

Catalytic Reactions of Organic Compounds
by Titanium Oxides and Titanate Nanotubes

Emiko WADA

Contents

Chapter 1 General Introduction	3
1.1 Catalytic reactions for green chemistry	4
1.2 Acid catalyzed reactions and acid catalysis	4
1.3 Photocatalytic organic reactions	7
1.4 Outline of this thesis	10
References	12
Chapter 2 Protonated Titanate Nanotubes with Lewis and Brønsted Acidity: Relationship between Nanotube Structure and Catalytic Activity	15
2.1 Introduction	16
2.2. Experimental	18
2.3. Results and Discussion	20
4.4. Conclusions	43
References	44
Chapter 3 Effect of Preparation Conditions on the Structural and Acid Catalytic Properties of Protonated Titanate Nanotubes	47
3.1. Introduction	48
3.2. Experimental	50
3.3. Results and Discussion	52
3.4. Conclusions	64
References	65
Chapter 4 Effect of Nb doping into Protonated Titanate Nanotubes for Catalytic Activity and Acidity	67
4.1. Introduction	68
4.2. Experimental	69
4.3. Results and Discussion	72
6.4. Conclusions	90
References	90
Chapter 5 Direct Cyanomethylation of Aliphatic and Aromatic Hydrocarbons with Acetonitrile over Metal Loaded Titanium Oxide Photocatalyst	93
5.1. Introduction	94
5.2. Experimental	96
5.3. Results and discussion	98

5.4. Conclusion.....	118
References	119
Chapter 6 Dehydrogenative Lactonization form Diols with Platinum Loaded Titanium Oxide Photocatalyst	121
6.1.Introduction	122
6.2 Experimental	123
6.3 Results and discussion.....	125
6.4 Conclusion.....	135
References	136
Chapter 7 Summary	137
Acknowledgements.....	143

Chapter 1

General Introduction

1.1 Catalytic reactions for green chemistry

Catalysis plays important roles for current industrial chemistry because most industrial chemical processes include catalytic reactions. In general, catalytic reaction system is divided into homogenous one using molecular catalyst and heterogeneous one using solid catalyst. The homogeneous reaction system with molecular catalyst can control a chemical reaction in detail, in other words, molecular catalyst can promote the desired reaction easily compared with solid catalyst.

Homogeneous catalysts such as H_2SO_4 , KOH , and metal complex catalysts are usually utilized for synthesis of polymers, medicine, and so on. The reaction system involving such heterogeneous catalyst has some problems. For example, the separation of product and molecular catalyst is difficult, and the catalyst is not reusable. In case of inorganic acid catalysts such as H_2SO_4 , they have highly toxic and corrosive properties.

On the other hand, heterogeneous catalysts such as metal oxides, zeolites, supported metal catalysts are desirable in the view of more green and sustainable chemistry. Thus heterogeneous catalysts have been studied for both fields of fine chemistry and bulk chemistry. For example, the C–C bond formation reaction is a fundamental reaction in organic synthesis and has been widely developed with supported Pd catalysts instead of Pd metal complex catalysts [1].

1.2 Acid catalyzed reactions and acid catalysis

1.2.1 Variation of acid catalysts

In the acid catalysis, two kinds of acids are known, *i.e.*, Brønsted acid and Lewis acid. The typical reactions with Brønsted acid such as H_2SO_4 and HNO_3 are esterification of alcohols with carboxylic acid, aldol reactions between carbonyl compounds, and acetyl synthesis from carbonyl compounds, etc., whereas the reactions with Lewis acid such as AlCl_3 and TiCl_4 are Diels-Alder reaction of diene with olefin, Mukaiyama aldol reaction, and so on. Friedel-Crafts alkylation and

acylation are most studied class of C–C bond formation reactions, and can be catalyzed by both Lewis acid and Brønsted acid [2]. These acid catalyzed reactions can be applied in practical for the production of pharmaceutical chemicals, flavors, and cleaning substrates, in other words, homogeneous acid catalysts are still used in the field of fine chemistry. But they are usually not reusable and generate waste products. Due to the disadvantage, many efforts have been devoted to develop heterogeneous catalysts instead of using these homogeneous catalysts.

Heterogeneous acid catalysts such as silica-alumina and zeolite have been industrially used for bulk chemistry. For example, zeolites having strong acidity and regular porosity have been preferably utilized for catalytic cracking in petroleum refining because they exhibit high reaction selectivity, shape selectivity, high durability and reusability. The acidity of many heterogeneous catalysts including zeolites is comparable to the homogeneous catalyst. Thus, not only for the bulk chemistry but also for fine chemistry, researchers have reported many heterogeneous catalysts such as sulfured ZrO_2 [3], zeolites [4], mix oxides [5], and layered materials [6].

Recently, many new inorganic materials have been developed as acid catalysts. Kawai *et al.* reported that montmorillonite, which is a kind of layered clay having ion exchange capacity, can enhance aldol reactions of silyl enol ethers with aldehydes and acetals [7]. When proton is inserted between the layers instead of Na^+ , the montmorillonite functioned as an Brønsted acid catalyst. They also reported that the montmorillonite ion exchanged with Sn^{4+} showed catalytic activity for the reaction of cyanosilylation of ketones. [8] The successive acid-base reactions were achieved by Motokura *et al.* using two kinds of montmorillonites, where the montmorillonite having Brønsted acid sites catalyzed the first acid reactions and then another montmorillonite having base sites catalyzed further reaction [9].

Layered materials have been applied as acid catalysts as well. Tagusagawa *et al.* found that layered $HNbMoO_6$ functioned as a strong acid catalyst for Friedel-Crafts alkylation of toluene or anisole [6a]. The layered $HNbMoO_6$ specifically can accept the substances during the reaction, which

indicates that accessibility of reactants to the acid sites on heterogeneous catalysts is one of the key factors for the catalytic efficiency. In contrast, the reaction over layered titanate and niobate hardly promoted Brønsted acid catalyzed reactions such as alkylation of anisole because the distance of the interlayer is too narrow to provide reactive sites in interlayer acid sites. Takagaki *et al.* reported that that exfoliated layered materials such as HTiNbO₅ nanosheets efficiency catalyzed organic reactions of dehydration of propanol, cracking of cumene, and esterification of acetic acid [10].

Sulfated zirconia (SO₄²⁻/ZrO₂) and tungstic zirconia (WO₃/ZrO₂) are known as super acid catalysts ($H_0 = -16.1$ for SO₄²⁻/ZrO₂, and $H_0 = -13.3$ for WO₃/ZrO₂) [11]. It was reported that SO₄²⁻/ZrO₂ showed comparable catalytic activity for Friedel-Crafts benzoylation of alkylbenzenes with benzoic anhydride [12]. The acetylation of toluene is a difficult reaction because the formation of the intermediate, acetyl cation (CH₃CO⁺), hardly proceed even under a reflux condition, however, these super acid catalysts, SO₄²⁻/ZrO₂ and WO₃/ZrO₂, promoted this reaction at the mild reaction temperature 298 K and 323 K, respectively [13].

1.2.2 Structure and acidity

The acidity on the heterogeneous catalysts surface is totally determined by the structure and chemical properties of the catalyst material. It is well accepted that isolated Si(OH)Al sites in silica alumina, where Si and Al cations are in tetrahedral framework atoms interconnected by oxygen atom, can be act as a Brønsted acid site. This is the reason why zeolite shows acid property and catalytic activity for organic reactions. Besides zeolite, acid sites would be generated on many kinds of mixed oxides such as ZnO-Al₂O₃, TiO₂-Al₂O₃, and SiO₂-ZrO₂, on which the acidity were higher than single oxides such as TiO₂ and Al₂O₃ [14]. Tanabe *et al.* proposed that the acid sites on mixed oxides are formed by an excess of negative or positive charge, which can be suspected by the coordination numbers and valences, in the material [15]. According to this, isolated Ti(OH)M (M=Nb⁵⁺, or Ta⁵⁺) site on exfoliated HTiNbO₅ and HTiTaO₇ nanosheets would be strong acid sites to enhance Brønsted

acid catalyzed reactions [16]. The Brønsted acidity of nanosheets are demonstrated in the literature by using MAS NMR measurements and NH₃ temperature-programed desorption of ammonia [16b], which are considered as powerful techniques determine acid strength.

Some studies showed that the acidity related to the pore size of mesoporous silica. Yamamoto *et al.* demonstrated that the catalytic reaction rate by FSM-16 was improved with decrease of the pore size of the catalyst [17]. Iwamoto *et al.* suggested that weak acid sites are formed on the surface of mesoporous silica with uniformed porous structure [23]. In fact, amorphous silica does not have acid sites in the article ($H_0 = +4.8$) [19]. The correlation of acidity and pore size of zeolite was also investigated by Hung *et al.* and it was found that zeolite (H-ZSM-5) with narrow pores showed higher catalytic acidity than that with large pores [20]. These studies indicated that the pore structure, the pore size and the structural distortion can change the acidity.

Some research groups found that heterogeneous catalysts having both Lewis acid sites accepting a pair of electrons and Brønsted acid sites donating proton well promote various organic reactions [21–23]. Telalović *et al.* developed mesoporous inorganic acid catalysts, Al-Zr-TDU, in which Al and Zr cations provide Brønsted acid sites and Lewis acid sites, respectively, and the catalysts exhibited high activity for the cyclization of citronellal [21]. Kitano *et al.* mentioned that both of Brønsted and Lewis acids on protonated titanate nanotube cooperatively functioned to promote the Lewis acid catalyzed reaction of Friedel-Crafts alkylation at room temperature [22].

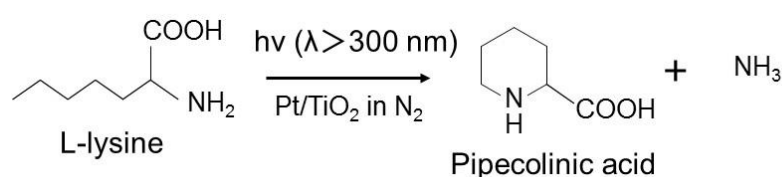
1.3 Photocatalytic organic reactions

Photocatalysts have been studied for hydrogen production from water [24], mineralization of toxic compounds [25] and so on. Under the light irradiation, photoexcited electrons and holes are generated and promote reduction and oxidation, respectively. These photocatalytic reduction and oxidation properties can be applied also for organic synthesis [26].

Although enormous number of semiconductors have been reported as new photocatalysts,

titanium dioxide (TiO₂) is most typical and popular photocatalyst due to its strong oxidative property, stability and nontoxic properties, as well as low cost. Since Fox *et al.* published their study for the oxidation of olefins over TiO₂ photocatalyst [27], many efforts have been made to achieve selective organic reactions (selective photocatalytic oxidation) with TiO₂ photocatalysis [26b] Principally, photocatalytic organic synthesis (*i.e.*, selective photocatalytic oxidation,) by TiO₂ photocatalysts is difficult in the presence of oxygen because the reduction of oxygen by photoexcited electron would form various kinds of reactive oxygen radical species, leading to the further and various oxidation of organic compounds. Thus, highly selective oxidation over TiO₂ photocatalysts have been developed in the absence of oxygen. In many cases, cocatalyst such as Pt nanoparticles have been employ to enhance the photocatalytic activity since Pt nanoparticles can promote the charge separation of photoexcited electron and hole pair to extend the life of them [28].

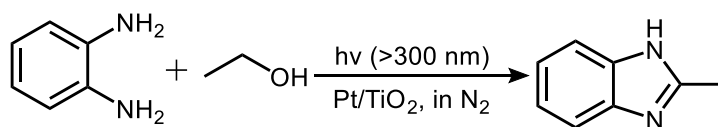
Pal *et al.* reported that L-pipecolic acid can be produced from L-lysine via cyclization by Pt/TiO₂ photocatalyst under the nitrogen atmosphere as shown in Scheme 1.1 [29]. In this reaction, Schiff base is formed by the oxidation of L-lysine, and the base functions as an electron acceptor, resulting the formation of pipecolic acid in high selectivity (85%).



Scheme 1.1. The formation of pipecolic acid with Pt/TiO₂ photocatalyst.

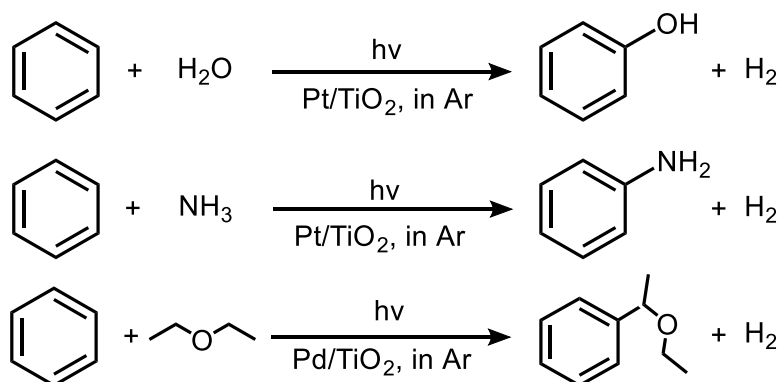
Shiraishi *et al.* reported that benzimidazole can be obtained from alcohol and diamine by a Pt loaded TiO₂ photocatalyst under the N₂ atmosphere as shown in Scheme 1.2 [30]. The reaction employs o-arylenediamines and alcohols as the reactants, and gives benzimidazoles with the selectivity of ca. 80–90%. The authors proposed that dehydrogenation reaction from the intermediate proceeded over

Pt nanoparticles on TiO₂.



Scheme 1.2. Synthesis of benzimidazole by Pt/TiO₂ photocatalyst.

Direct functionalizations of benzene have been developed with by Pt/TiO₂ photocatalyst [31] or Pd/TiO₂ bifunctional catalyst [32] under the argon atmosphere. In the hydroxylation and amination of benzene, the Pt/TiO₂ photocatalyst activates water and ammonia to form corresponding radical species, and these radical species can directly react with benzene.



Scheme 1.3. Direct functionalizations of benzene with simple molecules by Pt or Pd loaded TiO₂ photocatalysts.

On the other hand, the reaction between ethers and benzene are promoted by the Pd/TiO₂ catalyst. In this reaction the radical species formed from ethers cannot directly react with benzene. It is proposed that Pd nanoparticles on TiO₂ photocatalyst functions as metal catalyst to enhance the substitution reaction between the radical species and benzene ring to form intermediate. To develop photocatalytic organic synthesis further, the role of the cocatalyst also should be clarified.

1.4 Outline of this thesis

As mentioned above, many heterogeneous catalysts have been studied to promote catalytic reactions. There are two approaches to develop catalytic reaction systems: one is to find and develop new catalysts for the target catalytic reaction and another is to focus on the development of new catalytic reactions. Both types are efficient as a strategy for development of catalysis study. In the present thesis, the first part (Chapters 2–4) can be classified to the former type, where protonated titanate nanotube was studied and developed for a typical acid catalyzed reaction, *i.e.*, Friedel-Crafts alkylations [33–35]. On the other hand, the second part of this thesis (Chapters 5–6) shows the latter type, where new photocatalytic organic reactions such as direct cyanomethylation and direct lactonization were developed by using the typical metal loaded TiO₂ photocatalysts [36,37].

Through Chapters 2–4, protonated titanate nanotube was studied for Friedel-Crafts alkylations of aromatic compounds. Generally, heterogeneous acid catalyzed reactions including C–C bond formation are carried out over 363 K [38]. On the other hand, the titanate nanotube was recently reported as a new Lewis acid catalyst that functioned at room temperature for Friedel-Crafts alkylation of toluene with benzyl chloride [22]. Although it has already suggested that this material has both of Lewis acid sites and Brønsted acid sites, reaction mechanism of the Friedel-Crafts alkylation over the titanate nanotube was not investigated in detail. In Chapter 2, titanate nanosheet obtained by exfoliation of layered titanate was investigated to clarify the acid properties of protonated titanate nanotubes [33]. In the literature [39], the crystal structure of titanate nanotube was reported as the same crystal structure with the layered titanate such as H₂Ti₃O₇. The effect for acid properties of titanate nanotube was studied by comparing titanate material having same crystal structures. Chapter 3 shows a study of the relationship of the structure and catalytic performance. Aggregates of anatase nanoparticles, titanate nanotubes, and titanate nanorods were prepared by hydrothermal treatment at various temperatures, and their acid properties were investigated by using spectroscopic methods with a base compound as a probe. Through the study of chapter 2 and 3, it was proposed that the alkylation

of toluene takes place in the collaborative reaction mechanism by both Lewis acid sites and Brønsted acid sites on the titanate catalyst. From this hypothesis, it can be expected that the catalytic performance would be improved by increasing the Brønsted acid strength. According to this strategy, in Chapter 5, niobium doped titanate nanotube (Nb-TiNT) was prepared. The catalytic performance of Nb-TiNTs was much improved compared with non-doped titanate nanotube, and then the relation between the Brønsted acid strength and catalytic performance were investigated.

In Chapters 5 and 6, photocatalytic organic reactions are studied by using typical photocatalysts. Chapter 5 presents the direct cyanomethylation of hydrocarbons with acetonitrile by using metal loaded TiO_2 (M/TiO_2) photocatalysts. Since cyano group can be converted into not only carbonic acid or amide acid by hydrolysis but also converted into amine and aldehyde by reduction reaction, various reaction routes for introducing cyano group have been developed. Typically, potassium cyanide [40] and copper cyanide [41] are chosen as reactants to form compound having cyano group. In late years, cyanations over Pd catalyst with cyanation reagents such as ethyl cyanoacetate, [42] tert-butyl cyanide, [43] and acetone cyanohydrin [44] have been reported. In these reactions, reactants having leaving group and additives, which improve solubility and reactivity, are also necessary to produce desired product in high yield. [40a,40c,41] However, TiO_2 photocatalysts have a potential to activate stable molecules such as water [24b,47] and CH_3CN , [41] to be utilized for photocatalytic organic synthesis without any acids or oxidants. Here, direct cyanomethylation of aliphatic hydrocarbons over M/TiO_2 photocatalyst were examined by using acetonitrile as a source of cyano group. It was reported that direct cyanomethylation of aromatic compounds can proceed in the presence of Pd/TiO_2 catalyst and it was proposed that Pd cocatalyst would also act as a metal catalyst during the photocatalytic reaction [45]. Thus, the effect of the metal catalyst was investigated and found that the Pd metal catalyst is available only for the photocatalytic cyanomethylation of benzene.

Chapter 6 exhibits dehydrogenative lactonization from diols with M/TiO_2 photocatalyst. Acid catalysts give lactones from the compound having both of hydroxyl group and carboxyl group.

However, acid catalyst cannot promote lactonization from diol involving dehydrogenation because dehydration reaction of diols proceeds more efficiently in the presence of acid catalyst. Although many studies with metal complex catalysts have been reported for successive lactonizations [46], heterogeneous catalysts have been also developed [47]. Here, as a new route, photocatalytic lactonization was examined and established by using conventional M/TiO₂ photocatalysts.

At the end, Chapter 7 summarizes all catalytic reactions that were achieved in this thesis with protonate titanate nanotube as acid catalysts and metal loaded titanium dioxides as photocatalysts.

References

- [1] Yin, L.; Liebscher, J. *Chem. Rev.* **2007**, 107, 1, 133–173.
- [2] (a) Giovanni, S.; Maggi, R.; *Chem. Rev.* **2006**, 106, 3, 1077–1104. (b) Giovanni, S.; Maggi, R.; *Chem. Rev.* **2011**, 111, PR181–PR214.
- [3] Reddy, Benjaram M.; Meghshyam K. Patil. *Chem. Rev.* **2009**, 109, 6, 2185–2208.
- [4] Venuto, P.B. *Microporous Materials*, **1994**, 2, 297–411.
- [5] (a) Reddy, B.M.; Khan, A. *Catal. Rev.*, **2005**, 47, 257–296. (b) Sun, W. D.; Zhao, Z. B.; Guo, C.; Ye, X. K.; Wu, Y. *Ind. Eng. Chem. Res.*, **2000**, 39, 10, 3717–3725.
- [6] (a) Tagusagawa, C.; Takagaki, A.; Hayashi, S.; Domen, K. *J. Am. Chem. Soc.*, **2008**, 130, 7230–7231. (b) Motokura, K.; Baba, T. *Green Chem.*, **2012**, 14, 565–579.
- [7] Kawai, M.; Onaka, M.; Izumi, Y. *Bull. Chem. Soc. Jpn.*, **1988**, 61, 1237–1245.
- [8] (a) Onaka, M.; Higuchi, K.; Sugita, K.; Izumi, Y. *Chem. Lett.*, **1989**, 8, 1393–1396. (b) Onaka, M.; Higuchi, K.; Nanami, H.; Izumi, Y. *Bull. Chem. Soc. Jpn.*, **1993**, 66, 2638–2645.
- [9] (a) Motokura, K.; Fujita, N.; Mori, K.; Mizugaki, T.; Ebitani, K.; Kaneda, K. *J. Am. Chem. Soc.*, **2005**, 127, 9674–9675. (b) Motokura, K.; Tada, M.; Iwasawa, Y. *J. Am. Chem. Soc.*, **2009**, 131, 7944–7945.
- [10] Takagaki, A.; Sugisawa, M.; Lu, D.; Kondo, J. N.; Hara, M.; Domen, K.; Hayashi, S. *J. Am. Chem. Soc.*, **2003**, 125, 5479–5485.
- [11] Arata, K. *Green Chem.*, **2009**, 11, 1719–1728.
- [12] Nakamura, H.; Arata, K. *Bull. Chem. Soc. Jpn.*, **2004**, 77, 1893–1896.
- [13] Nakamura, H.; Kashiwara, Y.; Arata, K. *Bull. Chem. Soc. Jpn.*, **2003**, 76, 1071–1074.
- [14] Yamamoto, T.; Mori, S.; Shishido, T.; Kwai, J.; Tanaka, T. *Top Catal*, **2009**, 52, 657–663.
- [15] Iwamoto, M. *J. Synth. Org. Chem. Jpn*, **2004**, 62, 411–415.
- [16] Yamamoto, T.; Tanaka, T.; Funabiki, T.; Yoshida, S. *J. Phys. Chem. B*, **1998**, 102, 5830–5839.

- [17] Huang, J.; Jiang, Y.; Marthala, V. R.; Bressel, A.; Frey, J.; Hunger, M. *J. Catal.*, **2009**, 263, 277–283.
- [18] Telalović, S.; Ng, J. F.; Maheswari, R.; Ramanathan, A.; Chuah, G. K.; Hanefeld, U. *Chem. Commun.* **2008**, 4631–4633.
- [19] Kitano, M.; Nakajima, K.; Kondo, J. N.; Hayashi, S.; Hara, M. *J. Am. Chem. Soc.*, **2010**, 132, 6622–6623.
- [20] (a) Li, B.; Leng, K.; Zhang, Y.; Dynes, J. J.; Wang, J.; Hu, Y.; Ma, D.; Shi, Z.; Zhu, L.; Zhang, D.; Sun, Y.; Chrzanowski, M.; Ma, S. *J. Am. Chem. Soc.*, **2015**, 137, 4243–4248. (b) Li, S., Zheng, A., Su, Y., Zhang, H., Chen, L., Yang, J., Yang, J., Ye. C., Deng, F. *J. Am. Chem. Soc.*, **2007**, 129, 11161–11171. (c) Rane, N.; Kersbulck, M.; Van Santen, R. A.; Hensen, E. J. M. *Microporous Mesoporous Mat.*, **2008**, 110, 279–291.
- [21] Wada, E.; Kitano, M.; Nakajima, Hara, M. *J. Mater. Chem. A*, **2013**, 1, 12768–12774.
- [22] Shibata, K.; Kiyoura, T.; Kitagawa, J.; Sumiyoshi, T.; Tanabe, K. *J. Bull. Chem. Soc. Jp.*, **1973**, 46, 10, 2985–2988.
- [23] Tanabe, K.; Sumiyoshi, T.; Shibata, K.; Kiyoura, T.; Kitagawa, J. *Bull. Chem. Soc. Jp.*, **1974**, 47, 5, 1064–1066.
- [24] (a) Tagusagawa, C.; Takagaki, A.; Hayashi, S.; Domen, K. *J. Phys. Chem. C*, **2009**, 113, 7831–7837. (b) Takagaki, A.; Tagusagawa, C.; Hayashi, S.; Hara, M.; Domen, K. *Energy Environ. Sci.*, **2010**, 3, 82–93.
- [25] (a) Mohamed, O. S.; Gaber, A. E. M. A.; Abdel-Wahab, A. *J. Photochem. Photobiol. A*, **2002**, 148, 205–210. (b) Ni, M.; Leung, M. K.; Leung, D. Y.; Sumathy, K. *Renew. Sust. Energ. Rev.*, **2007**, 11, 401–425. (c) Kudo, A.; Miseki, Y. *Chem. Soc. Rev.*, **2009**, 38, 253–278.
- [26] (a) Gaya, U. I.; Abdullah, A. H. *J. Photochem. Photobiol- C, Rev.*, **2008**, 9, 1–12. (b) Anpo, M.; Kamat, P.V. *Springer*, **2010**, *Environmentally Benign Photocatalysts*, (Chapter 15)
- [27] (a) Anpo, M.; Kamat, P.V. *Springer*, **2010**, *Environmentally Benign Photocatalysts*, (Chapter 26). (b) Horst K. *Wiley*, **2007**, *Semiconductor photocatalysis for organic synthesis*. (c) Shiraishi, Y.; Hirai, T. *J. Photochem. Photobiol C*, **2008**, 9, 157–170.
- [28] Pillai, U. R.; Sahle-Demessie, E. *J. Catal.* **2002**, 211, 434 – 444.
- [29] Pal. B.; Ikeda, S.; Kominami, H.; Ohtani, B. *J. Catal.*, **2003**, 217, 152–159.
- [30] (a) Shibata, K.; Mimura, T.; Matsui, M.; Sugiura, T.; Minoura, H. *J. Chem. Soc., Chem. Commun.*, **1988**, 19, 1318–1320. (b) Park, K. H.; Joo, H. S.; Ahn, K. I.; Jun, K. *Tetrahedron Lett.*, **1995**, 36, 5943–5946. (c) Wang, H.; Partch, R. E.; Li, Y. *J. Org. Chem.*, **1997**, 62, 5222–5225.
- [31] Shiraishi, Y.; Sugano, Y.; Tanaka, S.; Hirai, T. *Angew. Chem. Int. Ed.*, **2010**, 49, 1656–1660.
- [32] (a) Yuzawa, H.; Yoshida, H. *Chem. Commun.*, **2010**, 46, 8854–8856. (b) Yoshida, H.; Yuzawa, H.; Aoki, M.; Otake, K.; Itoh, H.; Hattori, T. *Chem. Commun.*, **2008**, 38, 4634–4636.
- [33] Tyagi, A.; Matsumoto, T.; Kato, T.; Yoshida, H. *Catal. Sci. Technol.*, **2016**, 6, 4577–4583.

- [34] (a) Arata, K.; Hino, M. *Appl. Catal.*, **1990**, 59, 197–204. (b) Coq, B.; Gourves, V.; Figuéras, F. *Appl. Catal. A: Gen.*, **1993**, 100, 69–75. (c) Yadav, G. D.; Murkute, A. D. *Adv. Synth. Catal.*, **2004**, 346, 389–394.
- [35] (a) Bavykin, D.V.; Lapkin, A.A.; Plucinski, P.K.; Friedrich, J.M.; Walsh, F.C. *J. Phys. Chem. B* **2005**, 109, 19422–19427. (b) Bavykin, D.V.; Friedrich, J.M.; Walsh, F.C. *Adv. Mater.* **2006**, 18, 2807–2824. (c) Chen, Q.; Du, G.H.; Zhanga, S.; Penga, L.-M. *Acta Cryst.*, **2002**, B58, 587–593.
- [36] (a) Takagi, K.; Sasaki, K.; Sakakibara, Y. *Bull. Chem. Soc. Jpn.*, **1991**, 64, 1118–1121. (b) Anbarasan, P.; Schareina, T.; Beller, M. *Chemical Society Reviews*, **2011**, 40, 5049–5067. (c) Liu, Y.; Shirakawa, S.; Maruoka, K. *Org. Lett.*, **2013**, 15, 1230–1233.
- [37] (a) Sakamoto, T.; Ohsawa, K. *J. Chem. Soc., Perkin Trans.* **1999**, 1, 2323–2326. (b) Wen, Q.; Jin, J.; Zhang, L.; Luo, Y.; Lu, P.; Wang, Y. *Tetrahedron Lett.*, **2014**, 55, 1271–1280.
- [38] Zheng, S.; Yu, C.; Shen, Z. *Org. Lett.*, **2012**, 14, 3644–3647.
- [39] Peng, J.; Zhao, J.; Hu, Z.; Liang, D.; Huang, J.; Zhu, Q. *Org. Lett.*, **2012**, 14, 4968–4969.
- [40] Powell, K.J.; Han, L.-C.; Sharma, P.; Moses, J. E. *Org. Lett.*, **2014**, 16, 2158–2161.
- [41] Yoshida, H.; Fujimura, Y.; Yuzawa, H.; Kumagai, J.; Yoshida, T. *Chem. Commun.*, **2013**, 49, 3793–3975.
- [42] (a) Fujita, K.; Fujii, T.; Yamaguchi, R. *Org. Lett.*, **2004**, 6, 3525–3528. (b) Zhao, J.; Hartwig, J. F. *Organometallics*, **2005**, 24, 2441–2446. (c) Ito, M.; Osaku, A.; Shiibashi, A.; Ikariya, T. *Org. Lett.*, **2007**, 9, 1821–1824. (d) Tseng, K. N. T.; Kampf, J. W.; Szymczak, N. K. *Organometallics*, **2013**, 32, 2046–2049. (e) Fujita, K. I.; Ito, W.; Yamaguchi, R. *ChemCatChem*, **2014**, 6, 109–112.
- [43] (a) Kakiuchi, N.; Nishimura, T.; Inoue, M.; Uemura, S. *Bull. Chem. Soc. Jpn.*, **2001**, 74, 165–172. (b) Mitsudome, T.; Noujima, A.; Mizugaki, T.; Jitsukawa, K.; Kaneda, K. *Green Chemistry*, **2009**, 11, 79–797. (c) Touchy, A. S.; Shimizu, K. I. *RSC Advances*, **2015**, 5, 29072–29075.

Chapter 2

Protonated Titanate Nanotubes with Lewis and Brønsted Acidity: Relationship between Nanotube Structure and Catalytic Activity

Abstract

Nanostructured titanate materials with different morphologies, including layered materials, nanosheets, and nanotubes were examined as solid acid catalysts to elucidate the relationship between the structure and the catalytic properties. The titanate nanotube consists of a scroll-like layered structure derived from lamellar titanate nanosheets that exhibits excellent catalytic performance for the Friedel–Crafts alkylation of toluene with benzyl chloride near room temperature, exceeding the activities of layered titanates ($\text{H}_2\text{Ti}_3\text{O}_7$, $\text{H}_{0.7}\text{Ti}_{1.825}\square_{0.175}\text{O}_4\cdot\text{H}_2\text{O}$), and nanosheets that have similar crystal structures to that of the titanate nanotubes. Fourier transform infrared (FT-IR) spectroscopy and ^{31}P magic angle spinning nuclear magnetic resonance (^{31}P MAS NMR) spectroscopy using basic probe molecules has revealed that these titanate materials possess both Brønsted and Lewis acid sites, and the Brønsted acid strength of the titanate nanotubes is higher than that of the titanate nanosheets. The strong Brønsted acidity of the titanate nanotubes is attributed to lattice distortion originating from scrolling of the lamellar titanate nanosheet, which is evidenced by Raman spectroscopy and density functional theory (DFT) calculations. Furthermore, the mesopore structure of the titanate nanotubes is advantageous for acid catalysis, because the reactant molecules are confined within the nanotubes.

2.1 Introduction

Titanium is the second most abundant transition metal (ninth of all elements) in the Earth's crust and titanium oxides have been studied as versatile materials for many years due to their stability, nontoxicity and catalytic performance [1]. Nanostructured titanate materials, such as nanosheets, nanotubes, nanowires, nanospheres, and nanorods, with unique structures and properties have undergone extensive investigation in recent years [2–4]. Kasuga *et al.* reported on the synthesis of titanate nanotubes by the hydrothermal treatment of titania nanoparticles with aqueous NaOH solution [5,6]. The synthesis process is an inexpensive one-step reaction that requires neither expensive apparatus nor special chemicals. This material is a multiwalled scroll-type open-ended nanotube with

an inner diameter of *ca.* 6 nm and a layered spacing of *ca.* 0.7–0.8 nm [7], and is expected to have a layered titanate structure similar to those of $\text{H}_2\text{Ti}_3\text{O}_7$, $\text{H}_2\text{Ti}_4\text{O}_9 \cdot \text{H}_2\text{O}$, $\text{H}_2\text{Ti}_2\text{O}_5 \cdot \text{H}_2\text{O}$, $\text{H}_x\text{Ti}_{2-x/4} \square_{x/4} \text{O}_4 \cdot \text{H}_2\text{O}$, and $\text{H}_2\text{Ti}_5\text{O}_{11} \cdot \text{H}_2\text{O}$, rather than that of anatase TiO_2 [7]. The mechanism for the formation of titanate nanotubes is still controversial. It is now agreed that after dissolution of the starting TiO_2 in a high concentration of aqueous NaOH solution, layered nanosheets of sodium titanates are formed as intermediates, which are then folded into tubular structures and the nanotubes grow along their axis [7–10]. Over the past decade, titanate nanotubes with unique structures have been studied for various applications, such as catalyst supports, photocatalysis, electrocatalysis, H_2 storage and separation, H_2 sensing, lithium batteries, and photovoltaic cells [7]. Recently, it was found that protonated titanate nanotubes possess both Brønsted and Lewis acid sites and are applicable as acid catalysis for reactions such as Friedel–Crafts alkylation and the formation of 5-hydroxymethylfurfural (HMF) from glucose and fructose [11]. However, the correlation of the nanotube structure with the catalytic performance remains unclear.

In this chapter, protonated titanate nanotubes, layered titanates, and titanate nanosheets, which have similar crystal structures, were examined as solid acid catalysts. The titanate nanotubes consist of a scroll-like layered structure derived from lamellar titanate nanosheets and have mesopores with a pore diameter of *ca.* 6 nm, whereas the layered titanates and titanate nanosheets do not contain defined mesopores. The layered titanate catalysts are prepared by the proton exchange of $\text{Na}_2\text{Ti}_3\text{O}_7$ and $\text{Cs}_{0.7}\text{Ti}_{1.825} \square_{0.175} \text{O}_4 \cdot \text{H}_2\text{O}$, and subsequent exfoliation of the protonated layered titanates according to the previous literature [12–14]. The acid catalytic performance of these titanate materials is examined through the Friedel–Crafts alkylation of toluene with benzyl chloride. In addition, the relationship between the acidity and the structural distortion of the titanate nanotubes is discussed on the basis of Fourier transform infrared (FT-IR) spectroscopy, ^{31}P magic angle spinning nuclear magnetic resonance (^{31}P MAS NMR) spectroscopy, and density functional theory (DFT) calculations.

2.2. Experimental

2.2.1 Preparation of Titanate Materials

Protonated titanate nanotubes were synthesized by following the procedure developed by Kasuga *et al.* [5,6] with a slight modification. TiO₂ powder (ST-01, anatase, *ca.* 300 m²/g) and 70 mL of 10 M NaOH aqueous solution were placed into a Teflon-lined stainless autoclave and heated to 423 K for 20 h with stirring. After the reaction, the resulting white precipitate (sodium titanate nanotubes) was filtered and acid-washed until a pH value close to 7 was reached. To convert the sodium titanate nanotubes into the protonated form, the precipitate was dispersed into 0.1 M HNO₃ aqueous solution and stirred at room temperature for 24 h until the solution reached pH 1.5. The material was then washed repeatedly with distilled water and dried overnight in an oven at 343 K, yielding the protonated titanate nanotubes. The bulk layered titanates were prepared by conventional solid-state calcination [12–14]. Exfoliated H₂Ti₃O₇ and H_{0.7}Ti_{1.825}O₄·H₂O nanosheets were obtained by adding alkylamine solution to suspensions of the protonated layered titanate in distilled water [12–14].

4.2.2 Acid Catalyzed Reactions

The Friedel-Crafts alkylation of toluene with benzyl chloride in the liquid phase was performed in a 100 mL two-neck round-bottom flask with a reflux condenser at 373 and 300 K. The reactions were conducted using a mixture of 0.2 g of catalyst, toluene (0.1 mol) and benzyl chloride (0.01 or 0.02 mol) under an argon atmosphere. During the reactions, the liquid phase was monitored by gas chromatography (GC-17A, Shimadzu) with a DB-FFAP capillary column and a flame ionization detector.

4.2.3 Characterizations

The titanate materials were characterized by scanning electron microscopy (SEM; S-5200, Hitachi), transmission electron microscopy (TEM; EM002BF, TOPCON Tech. Co.), powder X-ray

diffraction (XRD; Ultima IV, Rigaku), and Raman spectroscopy (NRS-2100, Jasco). The Brunauer-Emmet-Teller (BET) specific surface area and Barrett-Joyner-Halenda (BJH) particle size distribution of the samples were determined from nitrogen adsorption–desorption isotherms measured at 77 K using an automatic gas adsorption instrument (NOVA 4200e, Quantachrome) after evacuation of the sample at 423 K. The acidity of each sample was examined by FT-IR spectroscopy (FT/IR-6100, Jasco) and ^{31}P magnetic angle spinning nuclear magnetic resonance spectroscopy (MAS NMR; ASX400, Bruker). FT-IR spectra were measured using a spectrometer equipped with an MCT detector at a resolution of 2 cm^{-1} to estimate the acidities of the samples. Samples were pressed into self-supported disks (20 mm diameter, *ca.* 20 mg), which were placed in a quartz cell equipped with NaCl windows and connected to a closed gas-circulation system, allowing for thermal adsorption-desorption experiments. The FT-IR spectrum of a clean disk was measured after pre-treatment at 423 K for 1 h to obtain a background spectrum. Adsorption of pyridine was conducted at room temperature (298 K) and the adsorption of CO was conducted at approximately 100 K with a stepwise decrease in pressure from 20 to 0.01 Torr. The FT-IR spectra presented here were obtained by subtracting the background spectra from those of the adsorbed species. The acid densities of the titanate materials were estimated from FT-IR measurements of pyridine-adsorbed samples at 298 K, according to the previous literatures [11,15]. ^{31}P MAS NMR spectra for samples with adsorbed trimethylphosphine oxide (TMPO) were measured at room temperature. A single-pulse sequence was employed with high-power proton decoupling. Bruker MAS probe heads were used with a 4 mm zirconia rotor. The spinning rate of the sample was set at 10 kHz. The ^{31}P chemical shift was referenced to 85% H_3PO_4 at 0.0 ppm. $(\text{NH}_4)_2\text{HPO}_4$ was employed as a second reference material with the signal set at 1.33 ppm. TMPO-adsorbed samples were prepared by evacuated dehydration at 423 K for 1 h, followed by immersion in a dichloromethane solution of TMPO at room temperature for 1 day under argon. After evacuation to remove the solvent, the samples were packed into the rotor under a N_2 atmosphere.

DFT calculations were conducted to investigate the geometrical structures and electronic

interactions of the acid sites. The plane wave based density functional calculations were performed using the CASTEP software package [16,17]. The structure of the titanate nanosheets was based on the Inorganic Crystal Structure Database [18] #245891 with a stoichiometry of $\text{H}_2\text{Ti}_3\text{O}_7$. There were two unique Brønsted acid sites on the nanosheets. For the modeling of the titanate nanotubes, the extended nanosheet structure was bent so that twelve unit cells compose a circle (tube). Four Brønsted acid sites were examined on the outer and inner surfaces of a nanotube using NH_3 as the probe molecule. For the calculation of the nanotube, the P6 point group symmetry was imposed and six molecules were adsorbed. Therefore, the unit cell compositions were $\text{H}_4\text{Ti}_6\text{O}_{14} + \text{NH}_3$ for the nanosheet and $\text{Ti}_{72}\text{O}_{168} \text{H}_{48} + 6\text{NH}_3$ for the nanotube. During the calculation, the lattice constants were fixed, and only the atom coordinates were optimized. The Perdew, Burke and Ernzerhof (PBE) functional [19] was used together with ultra-soft core potentials. [20]

2.3. Results and Discussion

2.3.1 Structures of Titanate Nanotubes and Nanosheets

Figure 2.1 shows SEM images of titanate nanotubes and nanosheets. Rod-like particles (10–50 nm diameter, 0.3–3.0 μm length) are evident in the SEM image of Fig. 2.1(a). High resolution TEM (HRTEM) observation revealed that the material was not composed of rods, but nanotubes with a diameter of *ca.* 6 nm. The walls of the protonated titanate nanotubes consisted of two types of lattice fringes, as shown in Fig. 2.2(b). The intervals among the fringes parallel and perpendicular to the tube axis were estimated to be *ca.* 0.7 and 0.3 nm, respectively. The former and latter correspond to the interlayer space in the layered titanates and the distance between two adjacent O atoms in the topmost corner positions of the TiO_6 edge-sharing octahedra that form a zigzag structure as shown Fig. 2.3 [21–23]. The SEM (Figs. 2.1(b) and (c)) and TEM (Figs. 2.2(c) and (d)) images of the titanate nanosheets indicate that both the $\text{H}_2\text{Ti}_3\text{O}_7$ and $\text{H}_{0.7}\text{Ti}_{1.825}\square_{0.175}\text{O}_4 \cdot \text{H}_2\text{O}$ nanosheets are aggregates composed of rather loosely and irregularly stacked titanate nanosheets that are free of tubular particles.

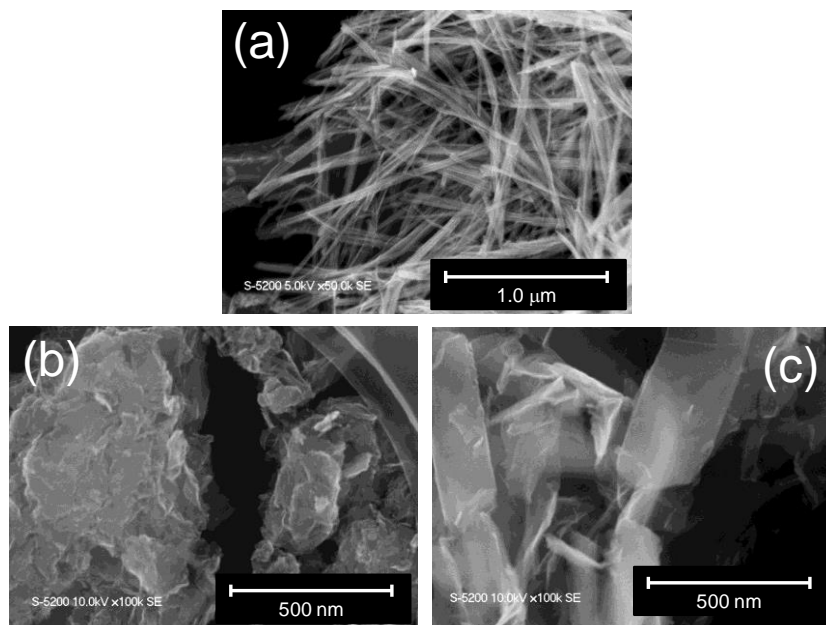


Figure 2.1. SEM images of (a) titanate nanotubes, (b) H_{0.7}Ti_{1.825}O₄·H₂O nanosheets, and (c) H₂Ti₃O₇ nanosheets.

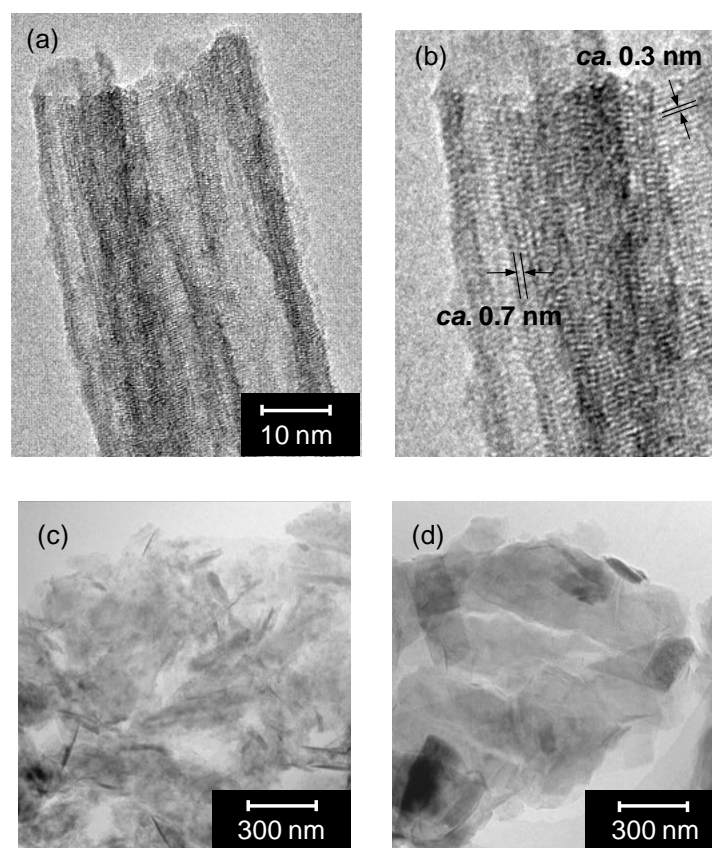


Figure 2.2. HRTEM images of (a) titanate nanotubes, (b) Enlarged HRTEM image of (a), (c) H_{0.7}Ti_{1.825}O₄·H₂O nanosheets, and (d) H₂Ti₃O₇ nanosheets.

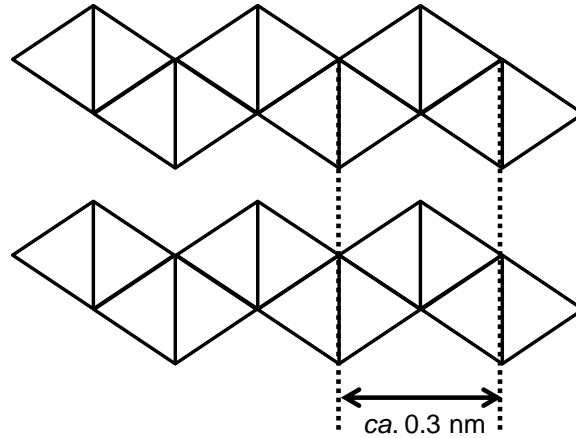


Figure 2.3. Specific surface areas and total pore volumes of titanate nanotubes and titanate nanosheets.

The nitrogen adsorption–desorption isotherms and BJH pore size distributions of these titanate materials are presented in Figs. 2.4(a) and (b), respectively. The corresponding specific surface areas and total pore volumes determined by N₂ adsorption are summarized in Table 2.1. The isotherm for the titanate nanotubes has a distinct hysteresis loop at $P/P_0 = 0.5–0.9$, which indicates a high density of mesopores in the material (type-IV according to IUPAC classification). Hysteresis loops are also observed for the titanate nanosheets at $P/P_0 \geq 0.4$, which suggests that the interspaces between sheet-like aggregates give rise to mesopores. Figure 2.4(b) shows that the titanate nanotubes have a narrow pore size distribution ranging from 2 to 10 nm with the peak located at *ca.* 6 nm, which corresponds to the inner diameter of the nanotubes observed by HRTEM. In contrast, the pore volumes of the titanate nanosheets are much smaller than that of the titanate nanotubes. Both the specific surface area and total pore volume of the titanate nanotubes are much higher than those of the titanate nanosheets (Table 2.1). The ideal surface area per unit weight of a tube (S_{tube}) and sheet (S_{sheet}) can be estimated geometrically from the following expressions: [24]

$$S_{tube} = [2\pi r_o l + 2\pi r_i l] / [(r_o^2 - r_i^2) \pi l d], \quad (2-1)$$

$$S_{sheet} = 2(xy + xt + yt) / xytd, \quad (2-2)$$

where r_o and r_i are the outer and inner radii of the tube, d is the density of the material, l is the length of the tube, t is the thickness of the sheet, and x and y are the lengths of longitudinal and lateral directions of the sheet, respectively. S_{tube} is calculated to be $423 \text{ m}^2 \text{ g}^{-1}$ for the nanotubes, using $r_o = 4.5 \text{ nm}$, $r_i = 3 \text{ nm}$, $d = 3.2 \text{ g cm}^{-3}$, and $l = 1500 \text{ nm}$ (Fig. 2.5(a)), which is consistent with the experimental result as summarized Table 1. Therefore, the average inner and outer diameters of the titanate nanotubes were determined to be 6 and 9 nm, respectively. S_{sheet} is calculated to be $915 \text{ m}^2 \text{ g}^{-1}$ for the nanosheets, using $x = 100 \text{ nm}$, $y = 200 \text{ nm}$, $d = 3.2 \text{ g cm}^{-3}$, and $t = 0.7 \text{ nm}$ (Fig. 2.5(b)), because the thickness of the titanate nanosheet is reported to be 0.7 nm. [25] The surface areas of the titanate nanosheets obtained are much smaller than an ideal surface area (Table 2.1), which indicates that certain parts of the aggregated nanosheets are not accessible by N_2 , probably due to intimate contact between the nanosheets. [26]

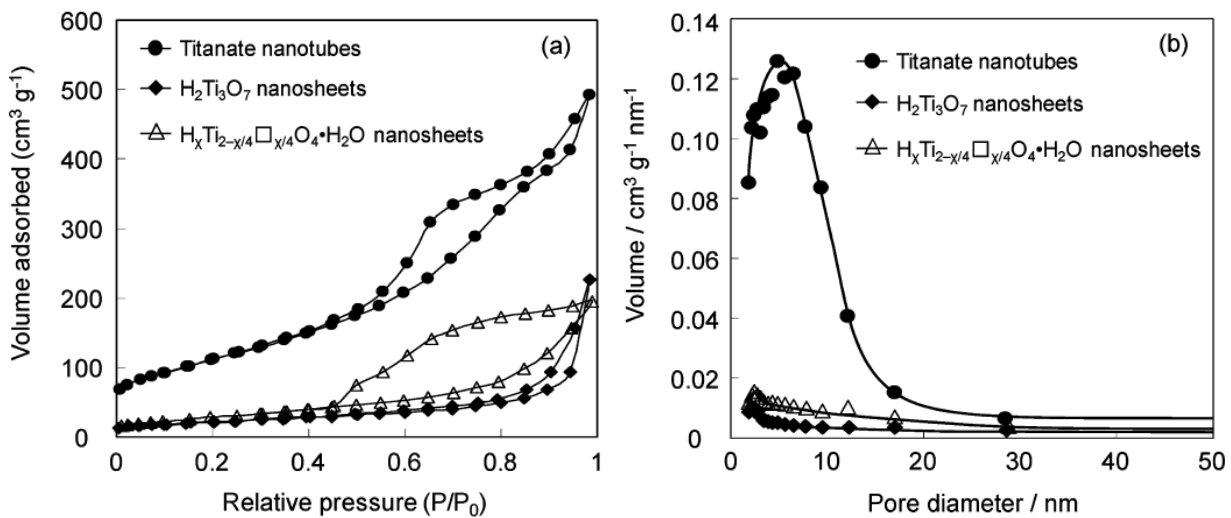


Figure 2.4. (a) Nitrogen adsorption–desorption isotherms and (b) BJH pore size distribution curves for titanate nanotubes, $\text{H}_{0.7}\text{Ti}_{1.825}\square_{0.175}\text{O}_4\cdot\text{H}_2\text{O}$ nanosheets, and $\text{H}_2\text{Ti}_3\text{O}_7$ nanosheets.

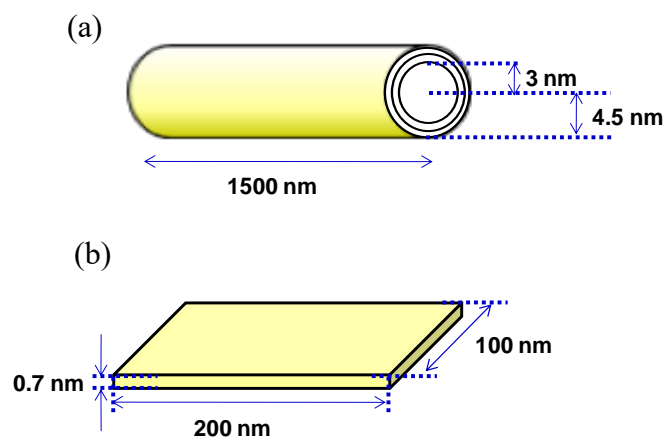


Figure 2.5. Schematic models for an ideal titanate (a) nanotube, and (b) nanosheet.

Table 2.1. Specific surface areas and total pore volumes of titanate nanotubes and titanate nanosheets.

Catalyst	Surface area ($\text{m}^2 \text{g}^{-1}$)	Pore volume ($\text{cm}^3 \text{g}^{-1}$)
Titanate nanotube	400	0.74
$\text{H}_2\text{Ti}_3\text{O}_7$ nanosheet	106	0.31
$\text{H}_x\text{Ti}_{2-x/4}\square_{x/4}\text{O}_4 \cdot \text{H}_2\text{O}$ nanosheet	75	0.31

Fig. 2.6 shows titanate nanotubes and nanosheets. The titanate nanotubes exhibited diffraction lines positioned at $2\theta = 10.7, 24.7, 28,$ and 48° , due to layered titanates such as $\text{H}_2\text{Ti}_3\text{O}_7, \text{H}_2\text{Ti}_2\text{O}_5 \cdot \text{H}_2\text{O}$, and lepidocrocite titanates [27–29]. The d-spacing was calculated to be 0.83 nm from the 2θ value of 10.7° using the Bragg equation, which is consistent with the interlayer spacing observed in the HRTEM image (Fig. 2.2(b)). These results suggest that the nanotubes are formed from layered titanates. The XRD patterns of the titanate nanosheets have weaker diffraction peaks than the layered titanates (Fig. 2.6) and are in good agreement with previously reported results [27–29]. The weak (200) diffraction peaks for the nanosheets indicate a much poorer periodic layer structure than the layered titanates. The

XRD patterns of the titanate nanosheets are almost identical to that of the titanate nanotubes, which indicates that these titanate materials have similar crystal structures.

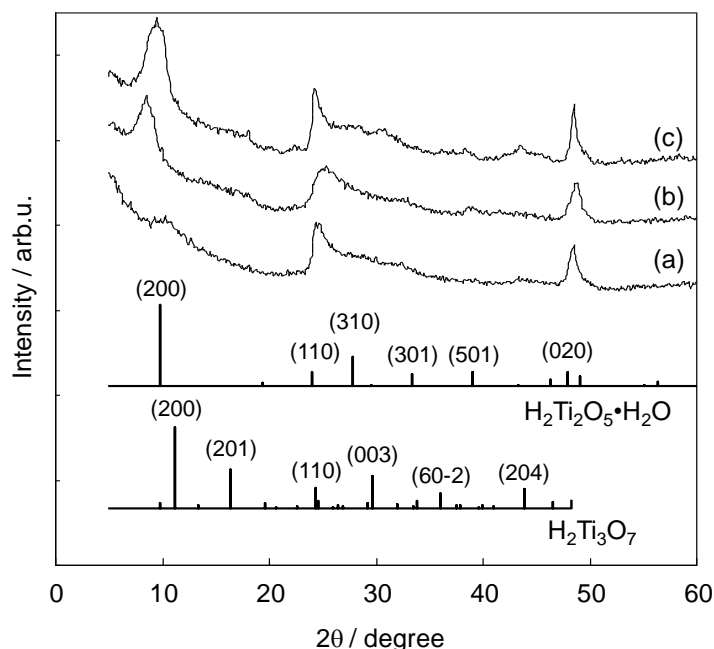


Figure 2.6. XRD patterns of (a) titanate nanotubes, (b) $\text{H}_{0.7}\text{Ti}_{1.825}\square_{0.175}\text{O}_4 \cdot \text{H}_2\text{O}$ nanosheets, and (c) $\text{H}_2\text{Ti}_3\text{O}_7$ nanosheets. Standard JCPDS diffraction patterns for $\text{H}_2\text{Ti}_2\text{O}_5 \cdot \text{H}_2\text{O}$ and $\text{H}_2\text{Ti}_3\text{O}_7$ are provided for reference.

Raman spectra of the titanate materials are shown in Fig. 2.7. Some bands were not observable because the notch filter cut off below 220 cm^{-1} . Anatase active modes at 144 , 397 , 516 , and 640 cm^{-1} were not observed for the titanate nanotubes, [30] which indicates complete transformation of the anatase into the titanate nanotubes. The titanate nanotubes showed well defined Raman bands at 275 , 395 , 458 , 665 , 833 , and 930 cm^{-1} and the spectrum is very similar to those for the $\text{H}_2\text{Ti}_3\text{O}_7$ and $\text{H}_{0.7}\text{Ti}_{1.825}\square_{0.175}\text{O}_4 \cdot \text{H}_2\text{O}$ nanosheets. According to the previous studies, the bands at around 270 , 450 , and 700 cm^{-1} are assignable to three A_g symmetric modes corresponding to pure framework Ti–O–Ti vibrations for layered titanates [31–35]. The bands around 830 and 930 cm^{-1} are assigned to a Ti–O–H symmetrical stretching mode with a very short Ti–O distance, and four coordinate Ti–O vibration in the titanate structure, respectively [33,35,36]. It is noteworthy that $\text{H}_2\text{Ti}_3\text{O}_7$ nanosheets exhibited a low

vibration wavenumber of 680 cm^{-1} for the Ti–O–Ti stretching mode compared with that for the $\text{H}_{0.7}\text{Ti}_{1.825}\square_{0.175}\text{O}_4\cdot\text{H}_2\text{O}$ nanosheets (700 cm^{-1}), which suggests that the former has a weaker Ti–O bond strength than the latter. This is because the $\text{H}_{0.7}\text{Ti}_{1.825}\square_{0.175}\text{O}_4\cdot\text{H}_2\text{O}$ nanosheets are composed of infinitely edge-shared TiO_6 octahedra, whereas the $\text{H}_2\text{Ti}_3\text{O}_7$ nanosheets are composed of three edge-shared TiO_6 octahedra that are linked by corner-sharing (Fig. 2.8) [32]. On the other hand, the band at 665 cm^{-1} for the titanate nanotubes shows a larger shift than that of the titanate nanosheets, which indicates that bending of the TiO_6 octahedral layers during the scrolling process give rise to a red-shift of the Ti–O–Ti stretching phonon line [37,38]. These results suggest that the structure of the titanate nanotubes is very similar to that of the $\text{H}_2\text{Ti}_3\text{O}_7$ and $\text{H}_{0.7}\text{Ti}_{1.825}\square_{0.175}\text{O}_4\cdot\text{H}_2\text{O}$ nanosheets, whereas the titanate nanotubes have lattice distortion, because they are formed by the scrolling of lamellar titanate nanosheets. This result does not conflict with the literature which suggests that titanate nanotube composes of highly distorted TiO_6 octahedra considering from Ti K-edge XAFS spectra [39].

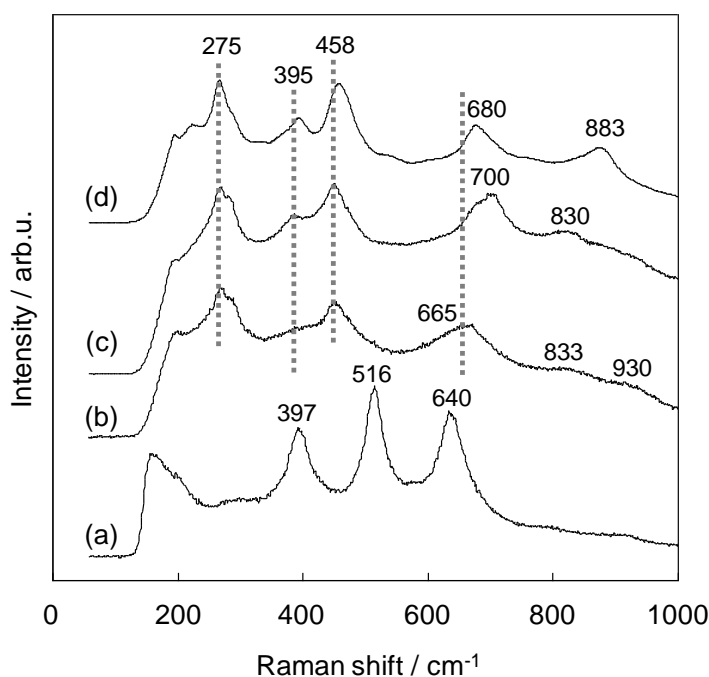


Figure 2.7. Raman spectra for (a) TiO_2 , (b) titanate nanotubes, (c) $\text{H}_{0.7}\text{Ti}_{1.825}\square_{0.175}\text{O}_4\cdot\text{H}_2\text{O}$ nanosheets, and (d) $\text{H}_2\text{Ti}_3\text{O}_7$ nanosheets.

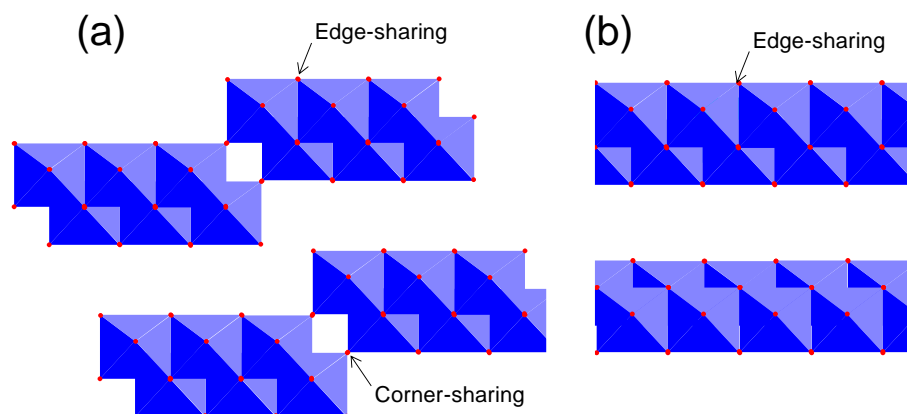


Figure 2.8. Schematic representations of (a) layered $\text{H}_2\text{Ti}_3\text{O}_7$ and (b) layered $\text{H}_{0.7}\text{Ti}_{1.825}\square_{0.175}\text{O}_4\cdot\text{H}_2\text{O}$ crystal structures.

4.3.2 Catalytic Performance.

The catalytic performance of the protonated titanate nanotubes was demonstrated using the Friedel-Crafts alkylation of toluene with benzyl chloride in the liquid phase. The results for the Friedel-Crafts alkylation, including acid concentration, surface area, and turnover frequency (TOF) at effective Lewis acid sites are summarized in Table 2.2. Under the reaction temperature of 373 K, this reaction was efficiently catalyzed by titanate materials, except for layered titanates, and both *o*-benzyltoluene and *p*-benzyltoluene were formed. It is difficult for the reactant molecules to penetrate into the interlayer space of layered titanates; therefore, the interlayer Lewis acid sites are not available for the reaction [26]. Layered $\text{H}_2\text{Ti}_3\text{O}_7$ exhibited no catalytic activity, whereas layered $\text{H}_{0.7}\text{Ti}_{1.825}\square_{0.175}\text{O}_4\cdot\text{H}_2\text{O}$ catalyzed the reaction to some extent. This is because the vacancy sites of layered $\text{H}_{0.7}\text{Ti}_{1.825}\square_{0.175}\text{O}_4\cdot\text{H}_2\text{O}$ may function as Lewis acid sites. The amount of Lewis acid sites exposed on the surface of the layered titanates was much lower than that of the other titanate materials, which resulted in the lower catalytic activity. At 300 K, TiO_2 and the layered titanates with only Lewis acid sites had negligible catalytic activity. In contrast, the alkylation reaction proceeded over the titanate nanosheets and nanotubes, where both Lewis and Brønsted acid sites were exposed to the reactants. It

is therefore proposed that Brønsted acid sites promote alkylation on the Lewis acid sites at room temperature.

Table 2.2. Friedel-Crafts alkylation of toluene with benzyl chloride over various titanate and titanium dioxide catalysts ^a

	BET surface area (m ² /g ⁻¹)	Acid amount (mmol/g)		Yield of benzyltoluene (%)		TOF ^d (/min)
		Lewis acid	Brønsted acid	373 K ^b	300 K ^c	
Titanate nanotube	400	0.10	0.25	97	92	7.3
H ₂ Ti ₃ O ₇ nanosheet	75	0.03	0.12	90	7.6	0.7
H _{0.7} Ti _{1.825} □ _{0.175} O ₄ ·H ₂ O nanosheets	106	0.05	0.16	96	7.6	0.5
Layered H ₂ Ti ₃ O ₇	5	n.d.	n.d.	0	0	0
Layered H _{0.7} Ti _{1.825} □ _{0.175} O ₄ ·H ₂ O	16	n.d.	0.02	37	0	0
TiO ₂ (anatase)	300	n.d.	0.13	95	0	0

^a Reaction conditions: catalyst (0.2 g), toluene (0.1 mol), benzyl chloride (0.02 mol); ^bProduct yield after the reaction at 373K for 1 h. ^c Product yield after the reaction at 300 K for 4 h. ^d TOF was calculated from the yield of benzyl toluene in 15 min and the concentration of Lewis acid sites. n.d. = not detected.

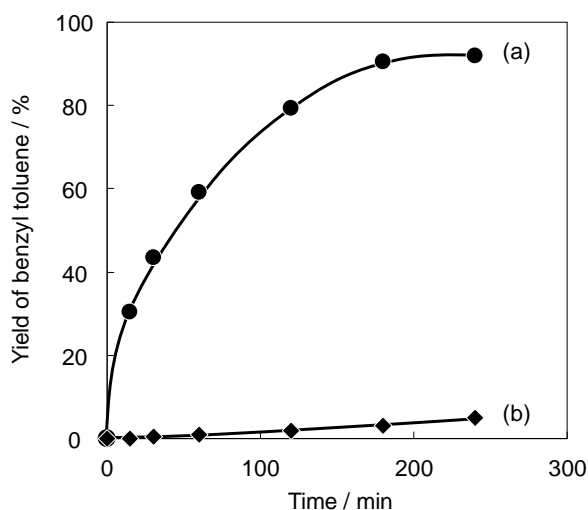


Figure 2.9. Time courses for benzyltoluene formation over titanate nanotubes in the (a) absence and (b) presence of 2,6-lutidine. Reaction conditions: catalyst (0.2 g), toluene (0.1 mol), benzyl chloride (0.02 mol), reaction temperature 300 K, amount of 2,6-lutidine added: 0.1 mmol g⁻¹ (cat.).

To clarify this hypothesis, the alkylation reaction was conducted in the presence of 2,6-lutidine, which can selectively interact with Brønsted acid sites and not with Lewis acid sites, due to the steric hindrance [40]. Figure 2.9 shows the time courses of benzyltoluene production over the titanate nanotubes with and without 2,6-lutidine at 300 K. The catalytic activity of the titanate nanotubes was significantly inhibited by 2,6-lutidine, which indicates that alkylation at the Lewis acid sites at 300 K is promoted by the Brønsted acid sites on the titanate nanotubes. A possible mechanism for the reaction is presented in Fig. 2.10, where initiation of the reaction would proceed by attack of the chlorine of benzyl chloride to coordinatively unsaturated Ti^{4+} centers (Lewis acid sites) of the catalyst surface. Adjacent Brønsted acid site attack the chlorine of benzyl chloride, resulting in the formation of a benzylcation and HCl. Then the benzylcation reacts with toluene to form benzyltoluene, while the Brønsted acid site is subsequently recovered. In sum, the Brønsted acid sites promote carbocation formation on the Lewis acid sites with HCl formed as a by-product. Although the titanate nanosheets have a sufficient amount of acid sites, only the titanate nanotubes function as an effective catalyst for the reaction at 300 K.

pyridine and CO. The samples were outgassed at 423 K for 1 h for the almost complete removal of water molecules from the catalysts. Difference FT-IR spectra of the pyridine-adsorbed titanate materials (298 K) are shown in Fig. 2.11.

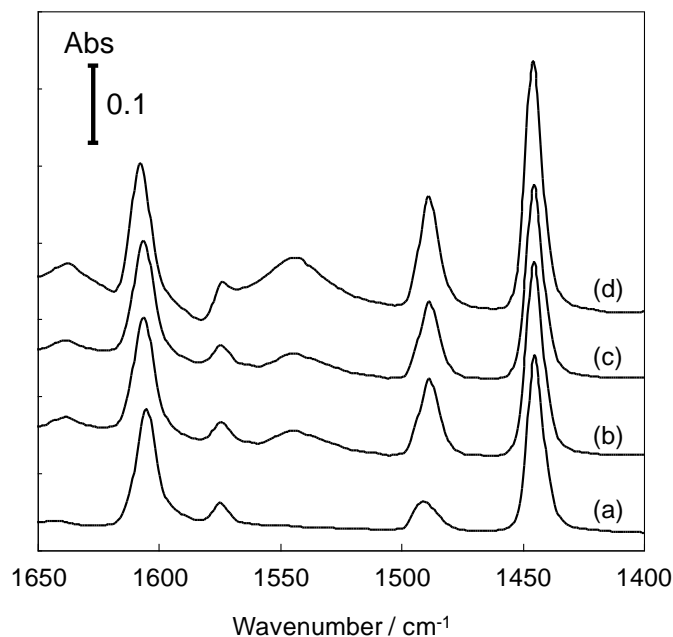


Figure 2.11. Difference FT-IR spectra for pyridine adsorbed on (a) TiO_2 , (b) $\text{H}_{0.7}\text{Ti}_{1.825}\square_{0.175}\text{O}_4\cdot\text{H}_2\text{O}$ nanosheets, (c) $\text{H}_2\text{Ti}_3\text{O}_7$ nanosheets, and (d) titanate nanotubes.

The bands observed at *ca.* 1445 and *ca.* 1605 cm^{-1} in all spectra are assigned to pyridine coordinatively bound to Lewis acid sites, which suggests that coordinatively unsaturated Ti^{4+} sites are present on the surfaces of these titanate materials [41–44]. The two broad bands around 1540 and 1640 cm^{-1} , due to pyridinium ions formed by Brønsted acid sites [41–44], were not observed for TiO_2 , but only for the titanate nanotubes and nanosheets, which indicates that protonated titanate nanotubes and nanosheets possess both Brønsted and Lewis acid sites.

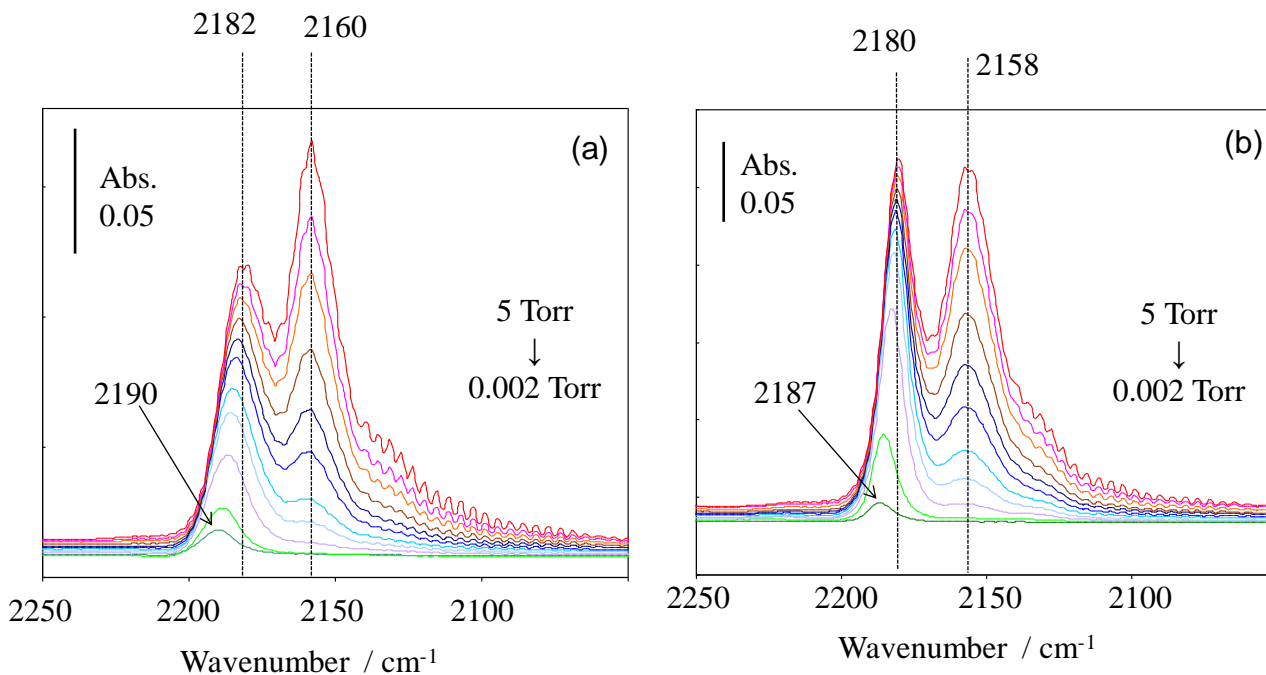


Figure 2.12. Difference FT-IR spectra for CO adsorbed on (a) titanate nanotubes and (b) $\text{H}_{0.7}\text{Ti}_{1.825}\square_{0.175}\text{O}_4 \cdot \text{H}_2\text{O}$ nanosheets at 100 K. The pressure of CO was decreased from 20 to 0.01 Torr by outgassing at 100 K.

The acid strength of these titanate materials were compared by FT-IR measurements of acid sites that adsorb CO as a basic probe molecule (Fig. 2.12.). The binding of CO to cationic surface sites stabilizes the 5σ level of CO (centered primarily on the carbon atom), which reduces the antibonding character and increases the overall bond order of the CO molecule [45–47]. Stronger interaction between CO molecules and acid sites on a solid acid shifts the CO stretching frequency to larger wavenumber with respect to that in the gas phase (*i.e.*, 2143 cm^{-1}). Figure 2.12(a) shows FT-IR spectra for CO adsorbed on the titanate nanotubes. Three intense peaks in the $2200\text{--}2100\text{ cm}^{-1}$ region were observed at high CO coverage. The peak around 2160 cm^{-1} is related to CO interacting with surface OH groups, while the weaker component at 2135 cm^{-1} is due to physisorbed CO in a liquid-like form, according to a previous FT-IR study of TiO_2 [47]. The CO band at 2160 cm^{-1} can be assigned to CO on acidic OH groups, due to the presence of Brønsted acid sites on the titanate nanotubes (and nanosheets). The peak centered at 2180 cm^{-1} is assigned to CO molecules adsorbed on coordinatively unsaturated Ti^{4+} sites (Lewis acid sites) [45–47]. The peak gradually shifted to 2190 cm^{-1} with

decreasing CO coverage, due to the progressive decrease of dynamic and static adsorbate-adsorbate interactions as the amount of adsorbed CO decreases. Figure 2.13(b) shows FT-IR spectra for CO adsorption on $\text{H}_{0.7}\text{Ti}_{1.825}\square_{0.175}\text{O}_4\cdot\text{H}_2\text{O}$ nanosheets. The three bands were also observed at the same positions for CO adsorption on $\text{H}_2\text{Ti}_3\text{O}_7$ nanosheets. The band attributed to CO on Lewis acid sites of the $\text{H}_{0.7}\text{Ti}_{1.825}\square_{0.175}\text{O}_4\cdot\text{H}_2\text{O}$ nanosheets was observed at 2180–2187 cm^{-1} , which indicates that the Lewis acidity of titanate nanosheets is comparable to that of titanate nanotubes. The stretching frequency of CO adsorbed on titanate nanotubes was smaller than that for adsorption on the protonated zeolites (*ca.* 2220 cm^{-1}) [44], which indicates that the Lewis acidity of the protonated titanate nanotubes is weaker than that of protonated zeolites. Although the peak due to CO adsorbed on acidic OH groups (Brønsted acid sites) also shifted to higher wavenumber regions with a decrease in the CO coverage, the peak was broad and not well defined at low CO coverage because the titanate materials have a number of OH groups with different acid strength. The Brønsted acidity of samples was evaluated using ^{31}P MAS NMR measurements with TMPO as a basic probe molecule. The adsorption of TMPO molecules on the acid sites causes a decrease in the density of the electron cloud surrounding the ^{31}P nucleus neighboring the oxygen atom on the phosphine oxides as the acid strength of the Brønsted acid sites increases, which causes the ^{31}P resonance peak position to shift downfield [48,49]. Figure 2.13 shows ^{31}P MAS NMR spectra for TMPO adsorbed on titanate nanotubes and nanosheets.

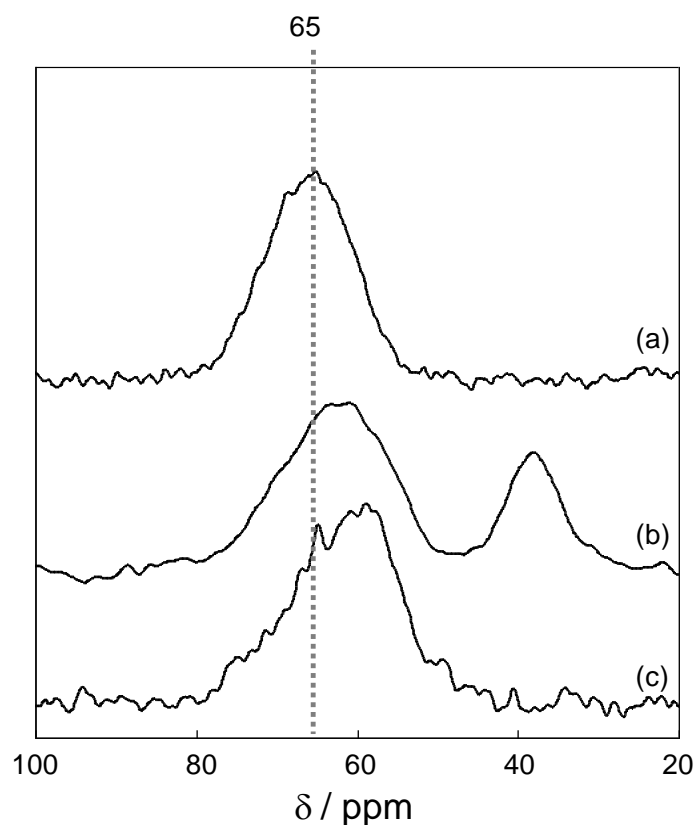


Figure 2.13. ^{31}P MAS NMR spectra for TMPO adsorbed on (a) titanate nanotubes, (b) $\text{H}_2\text{Ti}_3\text{O}_7$ nanosheets, and (c) $\text{H}_{0.7}\text{Ti}_{1.825}\square_{0.175}\text{O}_4 \cdot \text{H}_2\text{O}$ nanosheets.

The peak around 40 ppm observed for the $\text{H}_2\text{Ti}_3\text{O}_7$ nanosheets is ascribed to physisorbed TMPO. The protonated titanate nanotubes exhibited a distinct broad peak at *ca.* 65 ppm, whereas the main peaks for the $\text{H}_2\text{Ti}_3\text{O}_7$ and $\text{H}_{0.7}\text{Ti}_{1.825}\square_{0.175}\text{O}_4 \cdot \text{H}_2\text{O}$ nanosheets appeared at *ca.* 60 ppm. These peaks can be assigned to H^+ -complexed (Brønsted-bound) TMPO species, because the ^{31}P MAS NMR chemical shift range for the TMPO/Brønsted complex is determined to fall within the range of 50–90 ppm according to the previous literature [50,51]. There was no significant difference in Brønsted acidity between $\text{H}_2\text{Ti}_3\text{O}_7$ and $\text{H}_{0.7}\text{Ti}_{1.825}\square_{0.175}\text{O}_4 \cdot \text{H}_2\text{O}$ nanosheets although $\text{H}_{0.7}\text{Ti}_{1.825}\square_{0.175}\text{O}_4 \cdot \text{H}_2\text{O}$ nanosheets contain a large number of defect sites as compared to $\text{H}_2\text{Ti}_3\text{O}_7$ nanosheets, indicating that the Brønsted acidity does not depend on the number of defect sites. On the other hand, the titanate nanotubes possess stronger Brønsted acid sites than the titanate nanosheets. This suggests that the Brønsted acidity is due to the curvature of the nanotube wall. Furthermore, this results also indicate that the strong Brønsted

acidity of titanate nanotube is not due to the composition of the titanate materials because the composition of the titanate nanotubes is reported to be identical to that of $\text{H}_2\text{Ti}_3\text{O}_7$ or $\text{H}_{0.7}\text{Ti}_{1.825}\square_{0.175}\text{O}_4\cdot\text{H}_2\text{O}$ [27–29] and these titanate materials have similar crystal structures (Fig. 2.6). The peak positions in the ^{31}P MAS NMR spectra indicate that the strong acid sites of the titanate nanotubes (65 ppm) are comparable in strength to those of niobic acid [48], HY zeolite [52], and the HTiNbO_5 nanosheet catalyst (65 ppm) [53], but are weaker than those of H-ZSM-5 (86 ppm) [48] and H^+ resin (72 ppm) [49].

Ammonia (NH_3) adsorption energies were calculated using DFT calculations with periodic boundary conditions to evaluate the Brønsted acidity of the protonated titanate nanotubes [54–56]. The framework structure of the titanate nanosheets is represented in Figs. 2.14(a) and (b). An NH_3 molecule (basic probe) is adsorbed onto the OH group in each unit cell ($\text{H}_4\text{Ti}_6\text{O}_{14}$) of the titanate nanosheet to calculate the adsorption energy (Figs. 2.15(a) and (b)). There are two typical NH_3 adsorption structures, *i.e.*, linear Ti–OH (Fig. 2.15(a)) and bridged Ti–OH–Ti sites (Fig. 2.15(b)), of which the adsorption energies were estimated to be 87 and 89 kJ mol^{-1} , respectively.

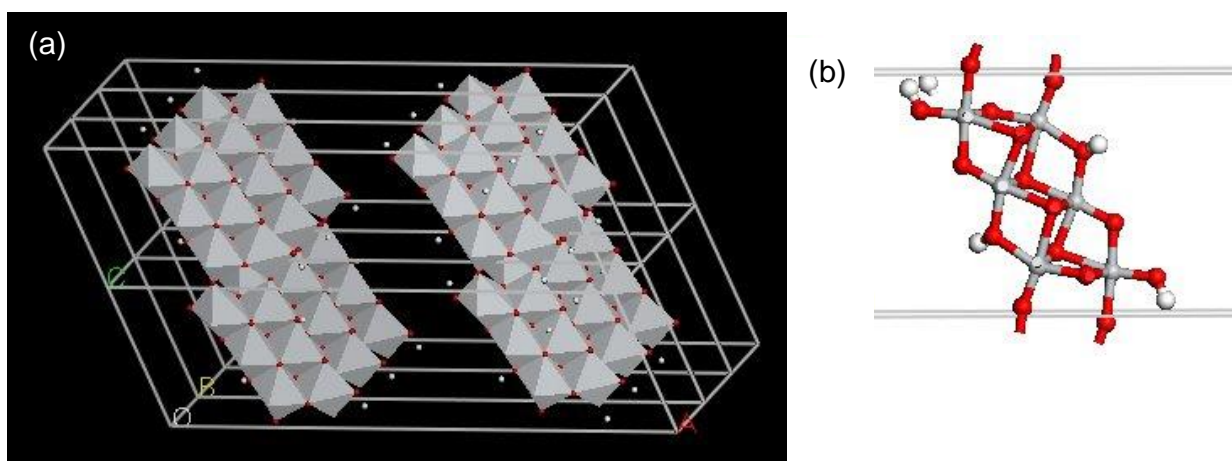


Figure 2.14. Nanosheet model with reference to the Inorganic Crystal Structure Database #245891 for a stoichiometry of $\text{H}_2\text{Ti}_3\text{O}_7$. The lattice constants are $a=35.466 \text{ \AA}$, $b=3.757 \text{ \AA}$, $c=9.759 \text{ \AA}$, $\alpha=\gamma=90^\circ$, and $\beta=101.46^\circ$. (a) The 3×2 extended unit cell with two layers by polyhedral representation, and (b) ball-and-stick representation of the unit cell used for DFT calculations of the single sheet and $\text{H}_4\text{Ti}_6\text{O}_{14}$ composition.

This indicates that the OH bridging groups exhibit slightly higher Brønsted acid strength than the OH terminal groups. Figure 2.16 shows the optimized nanotube model ($\text{Ti}_{72}\text{O}_{168}\text{H}_{48}$) composed of 12 unit cells of $\text{H}_4\text{Ti}_6\text{O}_{14}$. For comparison with the titanate nanosheets, the adsorption of NH_3 molecules on the nanotube model was calculated by DFT.

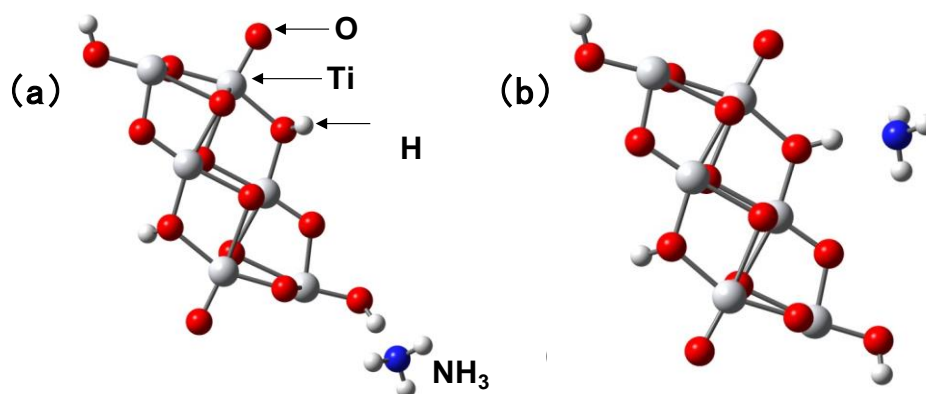


Figure 2.15. Optimized structures for NH_3 molecule adsorption on the (a) linear Ti-OH and (b) Ti-OH-Ti bridged sites of titanate nanosheets.

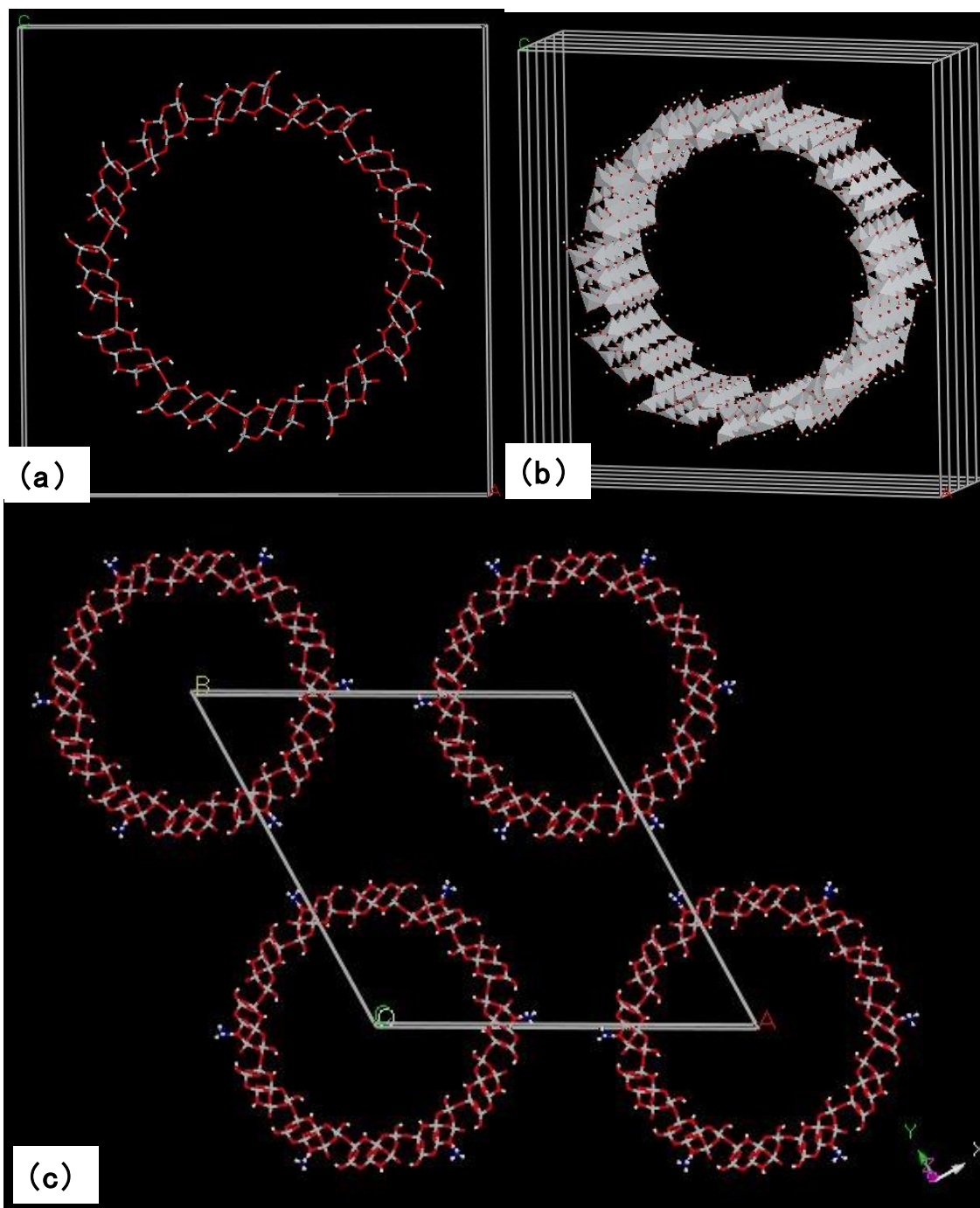


Figure 2.16. Framework structure of a titanate nanotube composed of twelve H₄Ti₆O₁₄ units shown as (a) ball-and-stick and (b) polyhedral representations. The lattice constants are $a=b=60 \text{ \AA}$, and $c=3.757 \text{ \AA}$. (c) The P6 point group symmetry is imposed for the adsorption of NH₃ and six NH₃ molecules are included.

Figure 2.17 shows four typical NH_3 adsorption structures to linear Ti-OH and bridged Ti-OH-Ti sites at the outer and inner tube surfaces. The adsorption energies were 62, 113, 89, and 114 kJ mol^{-1} for the linear-outside, bridged-outside, linear-inside, and bridged-inside structures, respectively. Therefore, the OH bridging groups on both the internal and external surfaces of the nanotube have higher Brønsted acid strength than the OH terminal groups. However, there was no noticeable difference in the Brønsted acid strength between the OH bridging groups on the internal and external surfaces of the nanotube. The DFT calculations revealed that NH_3 molecules adsorbed on the OH bridging groups of the titanate nanotubes are more stable than those adsorbed on the titanate nanosheets, which suggests that the Brønsted acidity of the titanate nanotubes is higher than that of the titanate nanosheets. This result is in good agreement with ^{31}P MAS NMR spectra (Fig. 2.13). It can be concluded that the strong Brønsted acidity of titanate nanotube is attributed to the curvature of the nanotube wall.

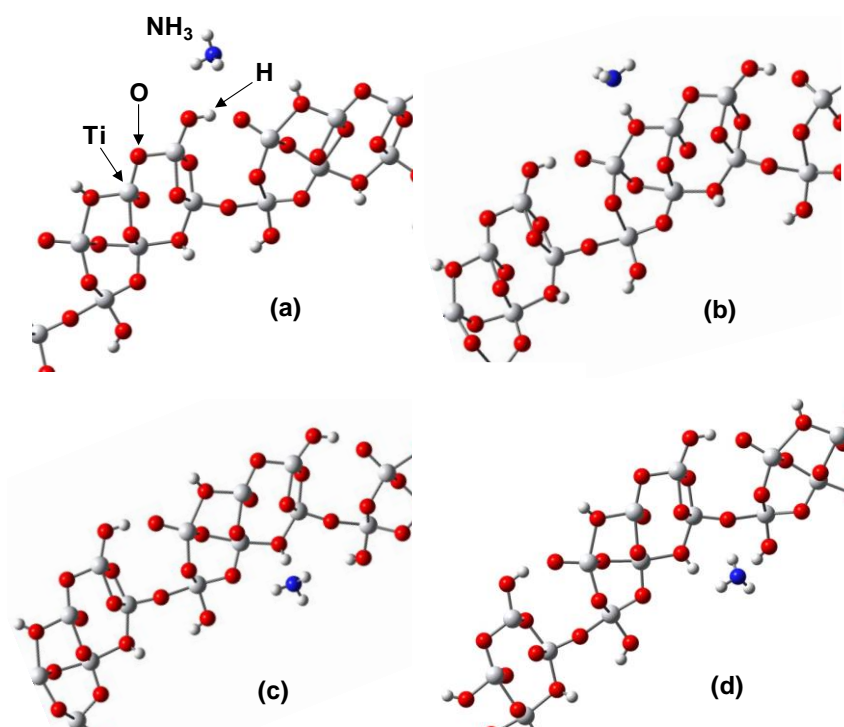
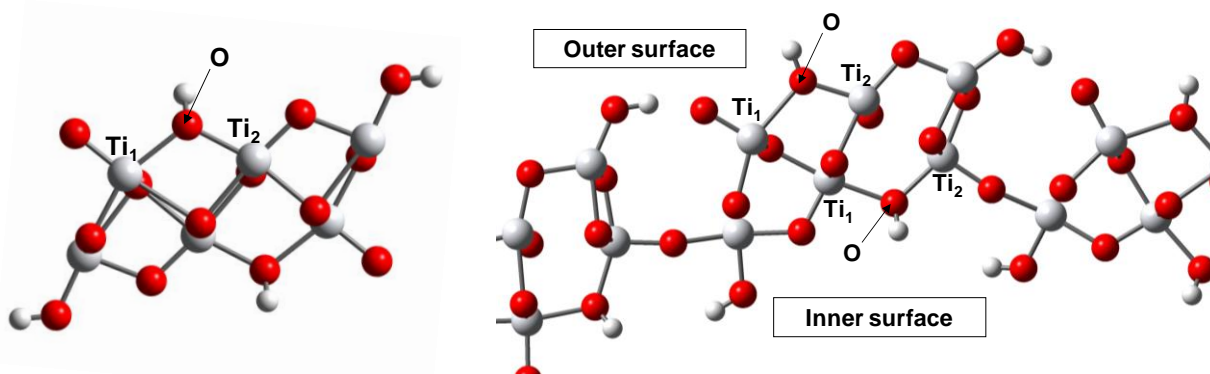


Figure 2.17. Optimized structures for NH_3 molecule adsorption on (a) linear Ti-OH , (b) outer surface bridged Ti-OH-Ti , (c) linear Ti-OH , and (d) inner surface bridged Ti-OH-Ti sites of titanate nanotubes.

Although we have not yet found relationship among the Ti–O–Ti bond angle, length, and the Brønsted acidity (Table 2.3), there is a clear difference in Ti–O–Ti bond strength between the titanate nanotubes and the titanate nanosheets. As shown in the Raman spectra (Fig. 2.8), the titanate nanotubes have a weaker Ti–O–Ti bond strength than the titanate nanosheets because of bending of the TiO₆ octahedral layers. In the literature on the relationship between bond strength and the localization of electron density [57], the electron density decreases as the Si–O bond length increases. Applying this assumption to titanate material, the electron density of the Ti–O–Ti bond in the titanate nanotubes is more delocalized than that of the titanate nanosheets. It has been reported that the electronic distribution near the acid center has a significant influence on the acid strength of zeolites [58].

Table 2.3. Bond lengths^a and bond angles in titanate nanotubes and titanate nanosheets before NH₃ adsorption



Catalyst	Acid sites	Ti–O–Ti angle (deg)	d(Ti ₁ –O)	d(Ti ₂ –O)	d(Ti ₃ –O)
Titanate nanosheet	Bridged OH group	114.7	2.129	2.019	4.148
Titanate nanotube	Bridged OH group (outer)	114.0	2.290	1.902	4.192
	Bridged OH group (inner)	116.6	2.062	1.997	4.059

^a d_{Ti-O} shows Ti–O bond length of Ti–OH–Ti bridged sites.

Therefore, in this study, the atomic charges of key atoms (O, H, N atoms) near Ti–OH–Ti sites were investigated to evaluate the local structure of Brønsted acid site. Table 2.4 shows that the Mulliken charges of O atoms belonging to the OH groups of the titanate nanotubes are even slightly less negative than those of the titanate nanosheets before NH₃ adsorption, and NH₃ adsorption enhances the tendency. (This is a consequence of electron donation from N to H atoms, and the increased electron density on H atom excludes the electron density on O atom.) In addition, the charges for H and N atoms in NH₃-adsorbed titanate nanotubes were less positive and less negative, respectively, compared to those of the NH₃-adsorbed titanate nanosheets (Table 2.5). This result indicates that the charge transfers between acid site and NH₃ molecules on titanate nanotubes is larger than that of titanate nanosheets.

As a result, the interatomic distances of the OH groups on the titanate nanotubes are significantly elongated after NH₃ adsorption compared with those of the titanate nanosheets, suggesting that protons are more easily released from the OH groups of the titanate nanotubes than from those of the titanate nanosheets. This results in large difference in NH₃ adsorption energy between titanate nanosheets and nanotubes.

Table 2.4. Selected parameters for NH₃ adsorption on Brønsted acid sites of the titanate nanotubes and nanosheets ^a

Catalyst	Acid sites	E_{ads} (kJ mol ⁻¹)	Before NH ₃ adsorption		After NH ₃ adsorption	
			q_0	d_{O-H}	q_0	d_{O-H}
Titanate nanosheet	Bridged	-89.2	-0.83	0.977	-0.79	1.004
	OH group					
Titanate nanotube	Bridged	-113.0	-0.81	0.972	-0.76	1.035
	OH group (outer)					
	Bridged					
	OH group (inner)	-113.9	-0.82	0.973	-0.77	1.042

^a NH₃ adsorption energy (E_{ads}), charges on the O atom (q_0) and the O-H bond length (d_{O-H}) of Ti–OH–Ti bridged sites.

Table 2.5. Mulliken charges^a of key atoms in titanate nanosheet and nanotube before and after NH₃ adsorption.

Catalyst	Acid sites	Before NH ₃ adsorption		After NH ₃ adsorption			Δq_O	Δq_H
		q_O	d_H	q_O'	d_H'	d_N'		
Titanate nanosheet	Bridged OH group	-0.83	0.41	-0.79	0.37	-1.15	0.04	-0.04
	Bridged OH group (outer)	-0.81	0.44	-0.76	0.35	-1.14	0.05	-0.09
Titanate nanotube	Bridged OH group (inner)	-0.82	0.41	-0.77	0.34	-1.10	0.05	-0.07

^a q_O and q_H show charges on the O and H atoms of Ti–OH–Ti bridged sites, respectively. ($\Delta q_O = q_O' - q_O$, $\Delta q_H = q_H' - q_H$)

The ³¹P MAS NMR analyses and DFT calculations revealed that the Brønsted acidity of titanate nanotubes is relatively superior to that of titanate nanosheets. Such effective Brønsted acid sites on the titanate nanotubes would promote the alkylation reaction on Lewis acid sites at 300 K (Fig. 2.7). In addition, the Friedel-Crafts alkylation reaction proceeds on both the internal and external surfaces of the nanotubes, because there is no difference in acid strength between both sites (Fig. 2.16). However, the reactant molecules may be effectively confined inside the titanate nanotubes due to their mesoporous structures. Recently, Tang *et al.* demonstrated the presence of a nanoconfinement effect on the molecular dynamics and phase transition of benzene and stearic acid confined inside titanate nanotubes by ¹³C NMR spectroscopy. [59,60] This result suggests that titanate nanotubes can contain aromatic molecules at near room temperature, and the inner space of the nanotubes can offer a special location for chemical reactions through the nanoconfinement effect. In this case, such a

nanoconfinement effect provides good access of reactants to the acid sites in the titanate nanotubes, which results in high catalytic performance. Thus, the remarkable catalytic activity of the titanate nanotubes compared with the titanate nanosheets can be attributed to a synergetic effect between Lewis and Brønsted acid sites and the nanoconfinement effect. The correlation between the nanotube structure and the acid catalytic performance established here will guide the design of new solid acid catalysts.

4.4. Conclusions

Protonated titanate nanotubes exhibited much higher catalytic activity for Friedel-Crafts alkylation than layered titanates such as $\text{H}_2\text{Ti}_3\text{O}_7$ and $\text{H}_{0.7}\text{Ti}_{1.825}\text{O}_{4.175}\cdot\text{H}_2\text{O}$, and titanate nanosheets, which have similar crystal structures. Raman spectroscopy revealed that the titanate nanotubes have a distorted structure, unlike the titanate nanosheets, which is due to bending of the TiO_6 octahedral layers of the nanotubes. On the basis of FT-IR, ^{31}P MAS NMR and DFT calculations, it was concluded that the titanate nanotubes exhibit stronger Brønsted acidity than the titanate nanosheets, and the acidity of the internal and external surfaces of the nanotubes is almost equal. This result indicates that lattice distortion originating from the scrolling of titanate nanosheets may form effective Brønsted acid sites, which promotes carbocation formation on the Lewis acid sites with the formation of HCl as a by-product. Such a synergetic effect between Lewis and Brønsted acid sites results in efficient alkylation on the titanate nanotubes. Furthermore, the titanate nanotubes have mesoporous structures, which would provide the reactants with good access to acid sites within the nanotubes. The nanoconfinement effect was also demonstrated to assist the catalytic activity of the titanate nanotubes.

References

- [1] Chen, X.; Mao, S. S. *Chem. Rev.* **2007**, *107*, 2891–2959.
- [2] Mao, Y.; Kanungo, M.; Benny, T. H.; Wong, S. S. *J. Phys. Chem. B*, **2006**, *110*, 702–710.
- [3] Tae, E. L.; Lee, K. E.; Jeong, J. S.; Yoon, K. B. *J. Am. Chem. Soc.* **2008**, *130*, 6534–6543.
- [4] Bavykin, D. V. Walsh, F. C., *Eur. J. Inorg. Chem.*, **2009**, *8*, 977–997.
- [5] Kasuga, T.; Hiramatsu, M.; Hoson, A.; Sekino, T.; Niihara, K. *Langmuir*, **1998**, *14*, 3160–3163.
- [6] Kasuga, T.; Hiramatsu, M.; Hoson, A.; Sekino, T.; Niihara, K. *Adv. Mater.*, **1999**, *11*, 1307–1311.
- [7] Bavykin, D. V.; Friedrich, J. M.; Walsh, F. C. *Adv. Mater.*, **2006**, *18*, 2807–2824.
- [8] Zhang, S.; Peng, L.M.; Chen, Q.; Du, G. H.; Dawson, G.; Zhou, W. Z. *Phys. Rev. Lett.*, **2003**, *91*, 256103–1–4.
- [9] Kukovecz, A.; Hodos, M.; Horváth, E.; Radnóczy, G.; Kónya, Z.; Kiricsi, I. *J. Phys. Chem. B*, **2005**, *109*, 17781–17783.
- [10] Wu, D.; Liu, J.; Zhao, X.; Li, A.; Chen, Y.; Ming, N. *Chem. Mater.*, **2006**, *18*, 547–553.
- [11] Kitano, M.; Nakajima, K.; Kondo, J. N.; Hayashi, S.; Hara, M. *J. Am. Chem. Soc.* **2010**, *132*, 6622–6623.
- [12] Sasaki, T.; Watanabe, M.; Michiue, Y.; Komatsu, Y.; Izumi, F.; Takenouchi, S. *Chem. Mater.* **1995**, *7*, 1001–1007.
- [13] Sasaki, T.; Watanabe, M. *J. Am. Chem. Soc.* **1998**, *120*, 4682–4689.
- [14] Dias, A. S.; Lima, S.; Carriazo, D.; Rives, V.; Pillinger, M.; Valente, A. A. *J. Catal.* **2006**, *244*, 230–237.
- [15] Nakajima, K.; Baba, Y.; Noma, R.; Kitano, M.; Kondo, J. N.; Hayashi, S.; Hara, M. *J. Am. Chem. Soc.* **2011**, *133*, 4224–4227.
- [16] Payne, M. C.; Teter, M. P.; Allan, D. C.; Arias, T. A.; Joan-nopoulos, J. D. *Rev. Mod. Phys.* **1992**, *64*, 1045–1097.
- [17] Milman, V.; Winkler, B.; White, J. A.; Pickard, C. J.; Payne, M. C.; Akhmatkaya, E. V.; Nobes, R. H. *Int. J. Quantum Chem.* **2000**, *77*, 895–910.
- [18](a) Bergerhoff, G.; Brown, I. D. in “Crystallographic Data-bases”, F.H. Allen et al. (Hrsg.) Chester, *International Union of Crystallography*, **1987**. (b) Belsky, A.; Hellenbrandt, M.; Karen, V. L.; Luksch, P. *Acta Cryst.* **2002**, B58, 364–369.
- [19](a) Perdew, J. P.; Burke, K.; Ernzerhof, M. *Phys. Rev. Lett.* **1996**, *77*, 3865–3868. (b) *ibid* 1997, *78*, 1396–1396.
- [20] Vanderbilt, D. *Phys. Rev. B* **1990**, *41*, 7892–7895.
- [21] Chen, Q.; Du, G. H.; Zhanga, S.; Peng, L. M. *Acta Cryst.* **2002** B58, 587–593.
- [22] Sun, X. M.; Li, Y. D. *Chem. Eur. J.* **2003**, *9*, 2229–2238.
- [23] Bavykin, D. V.; Lapkin, A. A.; Plucinski, P. K.; Friedrich, J. M.; Walsh, F. C. *J. Phys. Chem. B* **2005**, *109*, 19422–19427.
- [24] Kobayashi, Y.; Hata, H.; Salama, M.; Mallouk, T. E. *Nano Lett.* **2007**, *7*, 2142–2145.

- [25] Sakai, N.; Ebina, Y.; Takada, K.; Sasaki, T. *J. Am. Chem. Soc.* **2004**, 126, 5851–5858.
- [26] Takagaki, A.; Sugisawa, M.; Lu, D.; Kondo, J. N.; Hara, M.; Domen, K.; Hayashi, S. *J. Am. Chem. Soc.* **2003**, 125, 5479–5485.
- [27] Chen, Q.; Zhou, W.; Du, G. H.; Peng, L. M. *Adv. Mater.* **2002**, 14, 1208–1211.
- [28] Tsai, C. C.; Teng, H. S. *Chem. Mater.* **2006**, 18, 367–373.
- [29] Ma, R. Z.; Bando, Y.; Sasaki, T. *Chem. Phys. Lett.* **2003**, 380, 577–582.
- [30] Ohsaka, T.; Izumi, F.; Fujiki, Y. *J. Raman Spectrosc.* **1978**, 7, 321–324.
- [31] Horváth, E.; Kukovecz, Á.; Kónya, Z.; Kiricsi, I. *Chem. Mater.* **2007**, 19, 927–931.
- [32] Paek, M. J.; Ha, H. W.; Kim, T. W.; Moon, S. J.; Baeg, J. O.; Choy, J. H.; Hwang, S. J. *J. Phys. Chem. C* **2008**, 112, 15966–15972.
- [33] Nosheen, S.; Galasso, F. S.; Suib, S. L. *Langmuir* **2009**, 25, 7623–7630.
- [34] Beuvier, T.; Richard-Plouet, M.; Brohan, L. *J. Phys. Chem. C* **2010**, 114, 7660–7665.
- [35] Liu, H.; Yang, D.; Zheng, Z.; Ke, X.; Waclawik, E.; Zhu, H.; Frost, R. L. *J. Raman Spectrosc.* **2010**, 41, 1331–1337.
- [36] Torrente-Murciano, L.; Lapkin, A. A.; Chadwick, D. *J. Mater. Chem.* **2010**, 20, 6484–6489.
- [37] Menzel, R.; Peiró, A. M.; Durrant, J. R.; Shaffer, M. S. P. *Chem. Mater.* **2006**, 18, 6059–6068.
- [38] Gao, T.; Fjellvåg, H.; Norby, P. *Inorg. Chem.* **2009**, 48, 1423–1432.
- [39] Nakahira, A.; Kubo, T.; Numako, C. *Inorg. Chem.*, **2010**, 49, 5845–5852.
- [40] Ogasawara, Y.; Uchida, S.; Yamaguchi, K.; Mizuno, N. *Chem. Eur. J.* **2009**, 15, 4343–4349.
- [41] Busca, G. *Catal. Today* **1998**, 41, 191–206.
- [42] Zaki, M. I.; Hasan, M. A.; Al-Sagheer, F. A.; Pasupulety, L. *Colloids Surf., A* **2001**, 190, 261–274.
- [43] Ryczkowski, J. *Catal. Today*, **2001**, 68, 263–381.
- [44] Kondo, J. N.; Nishitani, R.; Yoda, E.; Yokoi, T.; Tatsumi, T.; Domen, K. *Phys. Chem. Chem. Phys.* **2010**, 12, 11576–11586.
- [45] Yang, Z.; Wu, R.; Zhang, Q.; Goodman, D. W. *Phys. Rev. B* **2001**, 63, 045419–1–6.
- [46] Panayotov, D. A.; Burrows, S.; Mihaylov, M.; Hadjiivanov, K.; Tissue, B. M.; Morris, J. R. *Langmuir* **2010**, 26, 8106–8112.
- [47] Minella, M.; Faga, M. G.; Maurino, V.; Minero, C.; Pelizzetti, E.; Coluccia, S.; Martra, G. *Langmuir* **2010**, 26, 2521–2527.
- [48] Rakiewicz, E. F.; Peters, A. W.; Wormsbecher, R. F.; Sutovich, K. J.; Mueller, K. T. *J. Phys. Chem. B* **1998**, 102, 2890–2896.
- [49] Zheng, A.; Huang, S. J.; Liu, S. B.; Deng, F. *Phys. Chem. Chem. Phys.* **2011**, 13, 14889–14901.
- [50] Kao, H. M.; Yu, C. Y.; Yeh, M. C. *Micropor. Mesopor. Mater.* **2002**, 53, 1–12.
- [51] Zhao, Q.; Chen, W. H.; Huang, S. J.; Wu, Y. C.; Lee, H. K.; Liu, S. B. *J. Phys. Chem. B* **2002**, 106, 4462–4469.
- [52] Tagusagawa, C.; Takagaki, A.; Hayashi, S.; Domen, K. *Catal. Today* **2009**, 142, 267–271.
- [53] Takagaki, A.; Tagusagawa, C.; Hayashi, S.; Hara, M.; Domen, K. *Energy Environ. Sci.* **2010**, 3,

82–93.

- [54] Yin, X.; Han, H.; Gunji, I.; Endou, A.; Ammal, S. S. C.; Kubo, M.; Miyamoto, A. *J. Phys. Chem. B* **1999**, 103, 4701–4706.
- [55] McGill, P. R.; Idriss, H. *Langmuir* **2008**, 24, 97–104.
- [56] Katada, N.; Suzuki, K.; Noda, T.; Sastre, G.; Niwa, M. *J. Phys. Chem. C* **2009**, 113, 19208–19217.
- [57] Gibbs, G. V.; Cox, D. F.; Rosso, K. M. *J. Phys. Chem. A* **2004**, 108, 7643–7645.
- [58] Sastrea, G.; Lewis, D. W. *J. Chem. Soc., Faraday Trans.* **1998**, 94, 3049–3058.
- [59] Tang, X. P.; Wang, J. C.; Cary, L. W.; Kleinhammes, A.; Wu, Y. *J. Am. Chem. Soc.* **2005**, 127, 9255–9259.
- [60] Tang, X. P.; Mogilevsky, G.; Kulkarni, H.; Wu, Y. *J. Phys. Chem. C* **2007**, 111, 18615–18623.

Chapter 3

Effect of Preparation Conditions on the Structural and Acid Catalytic Properties of Protonated Titanate Nanotubes

Abstract

The effect of hydrothermal treatment on the morphological and acid catalytic properties of titanate nanomaterials was examined. Anatase nanoparticles were converted into titanate nanotubes and layered titanate nanorods according to the heating temperature used during hydrothermal treatment. Fourier transform infrared (FT-IR) spectroscopy measurements and acid-base titrations revealed that all titanate nanomaterials possess Lewis acid sites, whereas Brønsted acid sites are formed after hydrothermal treatment at temperatures higher than 323 K. At 423 K, titanate nanotubes with an inner diameter of 6 nm were formed, which exhibited the highest catalytic activity for the liquid phase Friedel-Crafts alkylation of aromatics with benzyl chloride or benzyl alcohol. The titanate nanorods prepared at 473 K exhibited Lewis acidity, but had no effective Brønsted acid sites. The high catalytic performance of the titanate nanotubes can be attributed to the presence of a large number of both Lewis and Brønsted acid sites located on the surfaces of the nanotubes.

3.1. Introduction

Titanate nanotubes have been widely employed in the design of photocatalytic systems [1,2], catalyst supports [3,4], lithium batteries [5,6], and photoelectrochemical cells [7,8] since their discovery by Kasuga et al. in 1998 [9,10]. The nanotube is derived from the alkaline treatment of TiO₂ nanoparticles under highly basic conditions and the morphology can be strongly affected by the synthesis conditions, including temperature, duration of reaction time, and concentration of the alkaline solution [11–14]. For example, a mixture of titanate nanosheets and nanoparticles are obtained after alkaline treatment at low temperatures (< 363 K), whereas titanate nanotubes are formed in the temperature range 383–443 K. The formation of titanate nanorods usually occurs at temperatures higher than 443 K [12]. There is currently much discussion regarding the formation mechanism and phase of these titanate materials, although many studies have been devoted to investigation of the transformation process from TiO₂ to nanotubes. It is now generally agreed that titanate nanotubes are

formed through the dissolution and subsequent recrystallization of the particulate precursor into single- or multiwalled nanosheets, which then scroll or wrap into nanotubes [15–18]. In addition, the concentration of dissolved Ti(IV) moiety can determine the rate of crystallization of titanate nanosheets, which in turn controls the morphology of the final nanostructures [12]. High concentration of dissolved Ti(IV) moiety at high temperature is expected to lead to the titanate nanorods, while low concentration of dissolved Ti(IV) moiety at low temperature is expected to provide the titanate nanosheets as well as scrolled nanosheets, *i.e.*, titanate nanotubes.

Although these titanate nanomaterials have unique physicochemical and structural properties, they do not effectively function as catalysts without modification, such as calcination and deposition of metal catalyst [7,14]. For example, titanate nanotubes calcined at 573–673 K, which have a polycrystalline anatase structure, are effective photocatalysts for the oxidation of various organic compounds [1,2]. However, the photocatalytic activity of as-prepared titanate nanotubes is negligibly small because of its less crystallinity. As described previous chapter, protonated titanate nanotubes function as efficient Lewis acid catalysts for the Friedel-Crafts alkylation reaction of toluene with benzyl chloride near room temperature, and the catalytic activity is much higher than that of conventional solid acid catalysts such as ion-exchange resins, zeolite, and niobic acid [19]. The protonated titanate nanotubes possess both Lewis and Brønsted acid sites, whereas TiO₂ nanoparticles have only Lewis acid sites. The Brønsted acidity of these nanotubes is improved by lattice distortion due to scrolling of the nanosheets [19,20]. These results suggest that the effective Brønsted acid sites are formed during the hydrothermal treatment of TiO₂ nanoparticle with NaOH. Therefore, titanate materials prepared under various hydrothermal conditions are also expected to function as solid acid catalysts.

In this chapter, titanate materials prepared by the hydrothermal treatment of TiO₂ samples with NaOH at various temperatures were examined as solid acid catalysts. To gain insight into the origin of acidity, the effect of the treatment temperature on the catalytic activity of the titanate materials

for the Friedel-Crafts alkylation of toluene with aromatics such as benzyl alcohol and benzyl chloride was investigated. Furthermore, the acid properties of the materials were evaluated using Fourier transform infrared (FT-IR) spectroscopy and titration methods.

3.2. Experimental

3.2.1 Preparation of catalysts

All samples were synthesized by hydrothermal treatment of TiO₂ powders in NaOH aqueous solution. TiO₂ powder (ST-01, Ishihara Sangyo Co.) of 5.0 g and 10 M NaOH aqueous solution of 70 mL were mixed and introduced into a Teflon-lined stainless steel autoclave, and the autoclave was heated at 323, 423, and 473 K for 20 h. After the hydrothermal treatment, the obtained mixture was neutralized, and the resultant white precipitates were filtrated, and proton-exchange was carried out in HNO₃ aqueous solution (pH = 1.0) for 24 h. The materials were then washed several times with distilled water and dried overnight at 353 K. These samples are referred to as HT-Ti-X [X: hydrothermal treatment temperature (K)]. Bulk layered H₂Ti₃O₇ was prepared using conventional solid-state calcination according to the literature [21].

3.2.2 Characterization

The crystal structure of the samples was examined using X-ray diffractometry (XRD; Ultima IV, Rigaku) with Cu K α radiation (40 kV, 40 mA) at a wavelength of $\lambda = 1.54 \text{ \AA}$ and at a scan rate of $2.0^\circ \text{ min}^{-1}$ over the 2θ range of $10\text{--}60^\circ$. The surface morphologies of the samples were investigated by using the field emission scanning electron microscopy (FE-SEM; S-4700, Hitachi) and the high-resolution transmission electron microscopy (HRTEM; EM002BF, Topcon). Adsorption measurements were performed using N₂ adsorption at 77 K in an automatic gas adsorption instrument (NOVA 4200e, Quantachrome) after evacuation of the sample at 423 K for 1 h. The Brunauer-Emmett-Teller (BET) surface areas were calculated over a relative pressure (P/P_0) range of 0.05 to 0.30 from

N₂ adsorption-desorption isotherms. The pore size distribution was analyzed using the Barrett-Joyner-Halenda (BJH) method. The amounts of acid sites on all samples were estimated using FT-IR (FT/IR-6100, Jasco) spectroscopy for pyridine-adsorbed samples at room temperature, according to the previous literature methods [19,22]. FT-IR spectra were measured with a spectrometer equipped with a mercury cadmium telluride (MCT) detector at a resolution of 4 cm⁻¹. All samples were pressed into self-supporting pellets (*ca.* 20 mm diameter) and placed in a quartz cell equipped with NaCl windows and connected to a closed gas-circulation system allowing adsorption-desorption experiments. Each pellet was dehydrated by heating at 423 K for 1 h under vacuum, after which pyridine adsorption was conducted at room temperature. The ion exchange capacity of the samples was determined by the titration method, where the sample of 0.1 g was stirred in NaCl or NaOH aqueous solution of 30 mL for 1 h, and each supernatant solution was titrated with NaOH or HCl aqueous solution, respectively. The concentration of Na⁺ was determined by inductivity coupled plasma atomic emission spectroscopy (ICP-AES; ICPS-8100, Shimadzu).

3.2.3 Acid catalytic reaction

The catalytic performance of protonated titanate nanotubes was investigated using Friedel-Crafts alkylation reactions. The reactions were performed in the liquid phase using 0.20 g of catalyst, 0.1 mol of toluene or anisole, and 0.02 mol of benzyl chloride or 0.01 mol of benzyl alcohol. Prior to the reaction, all catalysts were evacuated at 423 K for 1 h, and the reaction was conducted under an argon atmosphere. The reaction vessel was placed in an oil bath maintained at 300 or 373 K for a duration of 0.5-5 h. After the reaction, products in solution were analyzed using gas chromatography (GC-17A, Shimadzu) with a DB-EFAP capillary column and a flame ionization detector.

3.3. Results and Discussion

3.3.1 Structures

Figure 3.1 shows XRD patterns of titanate materials prepared by the hydrothermal method at various temperatures. The anatase phase was observed for HT-Ti-323 (Fig. 3.1). For the diffraction patterns of the samples after hydrothermal treatment above 423 K, these peaks assignable to anatase disappeared completely and broad peaks attributed to titanate materials such as $\text{H}_2\text{Ti}_3\text{O}_7$ [23,24] were observed at $2\theta = 10.7, 24.7, 28, 34, 44.5$ and 48° . This result indicates that anatase TiO_2 is completely transformed into layered titanates. Figures 3.1(c) and (d) show that the intensity of the (200) peak due to the diffraction between titanate layers increases with the hydrothermal treatment temperature, which indicates that the number of stacked titanate layers increased. The XRD pattern of HT-Ti-473 is identical to that of titanate nanowires reported in the previous literature [25].

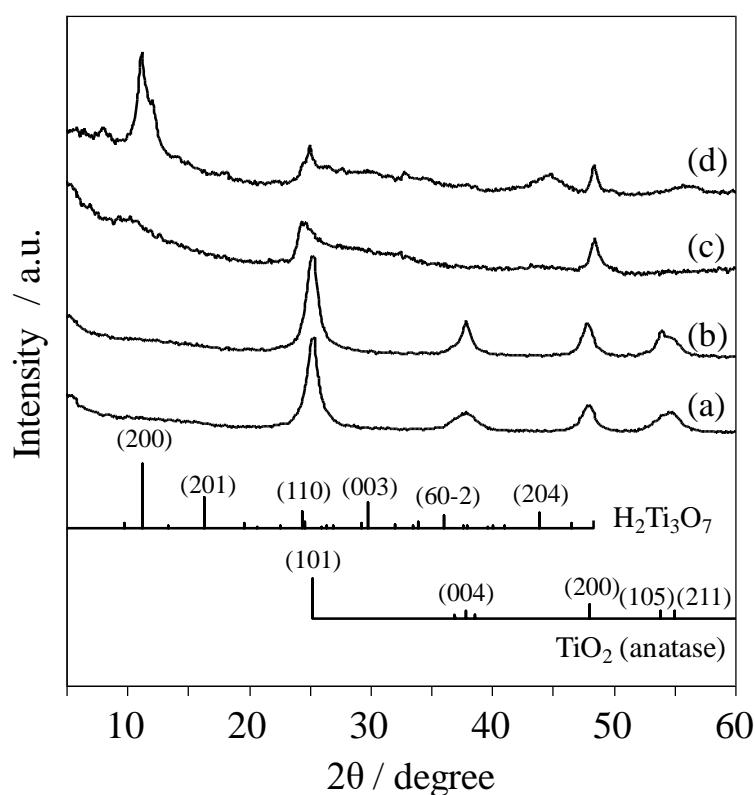


Figure 3.1. XRD patterns of (a) TiO_2 , (b) HT-Ti-323, (c) HT-Ti-423, and (d) HT-Ti-473. Standard diffraction patterns (JCPDS) for $\text{H}_2\text{Ti}_3\text{O}_7$ and anatase TiO_2 are provided at the bottom of the figure.

Figure 3.2 shows FE-SEM images of the titanate materials. Small nanoparticles with an average grain size of *ca.* 20–30 nm are somewhat agglomerated in the TiO₂ powders (Fig. 3.2(a)). HT-Ti-323 also consists of aggregated nanoparticles, although the grain boundaries are not distinct, which indicates that the surface of the TiO₂ particles is partially dissolved during the hydrothermal treatment. At heating temperatures higher than 423 K, one-dimensional nanofibers with high aspect ratios are produced, of which the lengths are several micrometers. In addition, the diameters of the fibers increase (*ca.* 30–200 nm) when the heating temperature is 473 K.

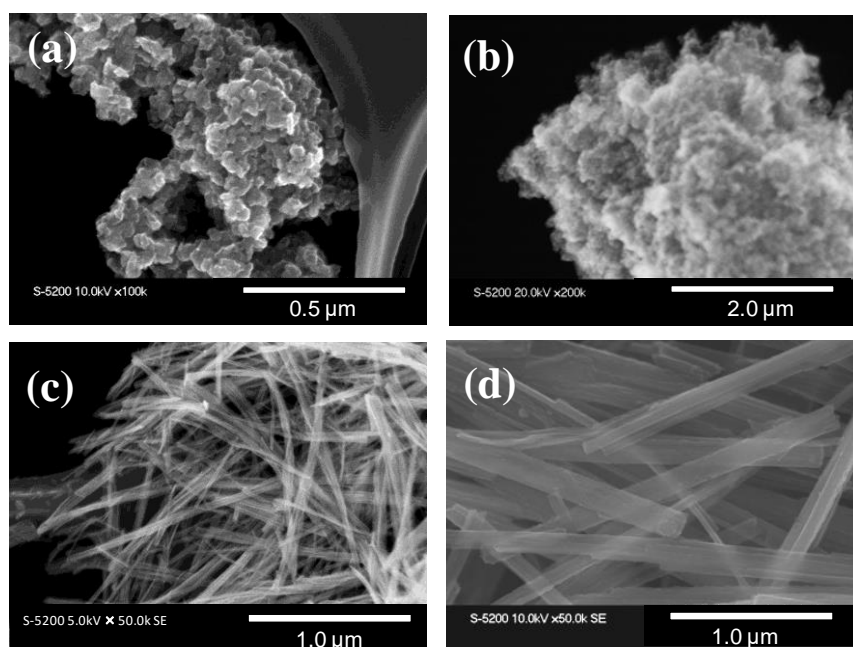


Figure 3.2. SEM images of (a) TiO₂, (b) HT-Ti-323, (c) HT-Ti-423, and (d) HT-Ti-473.

HRTEM images of HT-Ti-423 and HT-Ti-473 are shown in Fig. 3.3. HT-Ti-423 is composed of nanotubes with inner diameters of *ca.* 5 nm and outer diameters of *ca.* 9 nm. Na⁺ ions are not detected by XPS and ICP-AES analyses for HT-Ti-423, indicating that Na⁺ ions have no influence on the formation of the nanotubes. This result is consistent with the previous reports [13,26]. However, hydrothermal treatment at 473 K resulted in solid nanorods with large size distributions of both length and diameter. Selected area electron diffraction (SAED) patterns taken from areas consisting of many

nanotubes or nanorods are shown in the insets of Fig. 3.3. Diffraction rings are observed for both samples because these samples are polycrystalline and have random orientations. HT-Ti-473 exhibited more prominent diffraction rings than HT-Ti-423, which suggests that the structure of the titanate nanorods is more uniform and crystalline than the titanate nanotubes. From Fig. 3.3(b), the intervals among the fringes parallel and perpendicular to the tube axis were estimated to be *ca.* 0.8 and 0.3 nm, respectively, and the angle between the *a* and *c* axes is *ca.* 102°. These values are in good agreement with the lattice parameter of H₂Ti₃O₇ [27]. Furthermore, the number of stacked titanate layers in the titanate nanorods is much greater than that in the titanate nanotubes, which is consistent with the XRD results (Fig. 3.1).

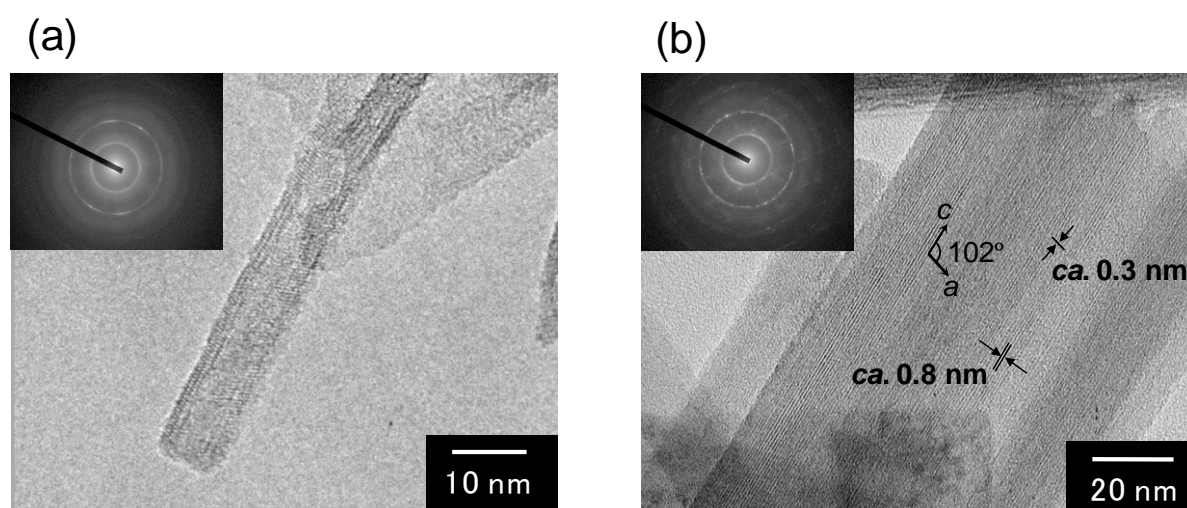


Figure 3.3. HRTEM images of (a) HT-Ti-423 and (b) HT-Ti-473. Insets show selected area electron diffraction patterns.

Nitrogen adsorption-desorption analysis was performed to investigate the surface area and pore size distribution of the obtained samples. Figure 3.4 shows BJH pore size distribution curves for various titanate materials, and the surface areas and total pore volumes are summarized in Table 3.1. TiO₂ has a broad pore size distribution from 2 to 50 nm and HT-Ti-323 had a narrower distribution in the range of 2–15 nm. These mesopores are attributed to the interspaces between aggregates of TiO₂

nanoparticles because hollow nanotube structures are formed after hydrothermal treatment above 423 K, as shown in Fig. 3.2 and 3.3. The surface area of HT-Ti-323 was lower than that of TiO₂, which may be due to partial dissolution of the TiO₂ particle surface and the aggregation of particles during hydrothermal treatment. However, HT-Ti-423 showed a narrow distribution ranging from 2 to 15 nm with the peak located at *ca.* 6 nm, which corresponds to the inner diameter of the nanotubes observed using HRTEM. Table 3.1 shows that HT-Ti-423 had the highest surface area and pore volume, which is attributed to the hollow structure. HT-Ti-473 had a low surface area and virtually no pores, which indicates the formation of nanorods rather than nanosheet scrolling, as confirmed in Fig. 3.3.

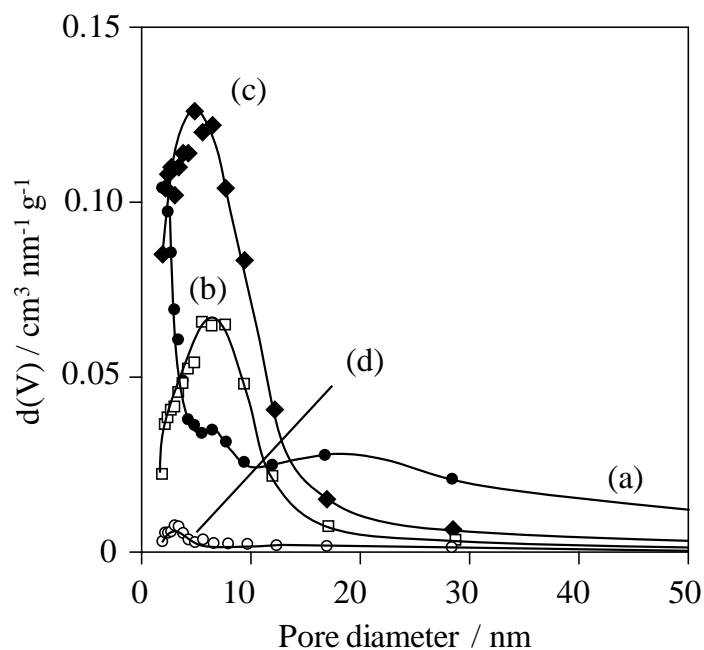


Figure 3.4. BJH pore size distributions of (a) TiO₂, (b) HT-Ti-323, (c) HT-Ti-423, and (d) HT-Ti-473.

Table 3.1. Physical properties of various titanium oxide materials and results for Friedel-Crafts alkylation of toluene with benzyl chloride. ^a

Catalyst	S_{BET} [m ² g ⁻¹]	V_{Total} [cm ³ g ⁻¹]	Acid concentration ^b (mmol g ⁻¹)		Ion exchange capacity ^e (mmol g ⁻¹)		Yield of benzyl toluene (%)	
			BAS ^c	LAS ^d	NaCl	NaOH	373 K ^f	300 K ^g
TiO ₂ (anatase)	300	300	n.d. ^h	0.13	0	1	94.5	0.0
HT-Ti-323	208	208	n.d.	0.05	0.03	1.3	95.0	28.0
HT-Ti-423	400	400	0.1	0.25	0.21	2.9	97.0	92.0
HT-Ti-473	30	30	n.d.	0.05	0	4.4	83.5	0.0
Layered H ₂ Ti ₃ O ₇	5	5	n.d.	n.d.	-	-	0.0	0.0

^a Reaction condition: catalyst (0.2 g), toluene (0.1 mol), benzylchloride (0.01 or 0.02 mol). ^b The acid concentrations of the titanate materials were estimated from FT-IR measurements of pyridine-adsorbed samples. ^c Brønsted acid sites, ^d Lewis acid sites ^e Ion exchange capacities of the samples estimated from the exchange of Na⁺ in aqueous 0.1 M NaCl (pH = 5.0) and 0.05 M NaOH solutions (pH = 12.7). ^f Yield of the product was measured after 1 h. ^g Yield of the product was measured after 4 h. ^h n.d. = not detected.

3.3.2 Acid properties

The acid properties of the titanate materials were evaluated by probing the vibrational spectra of adsorbed pyridine using FT-IR spectroscopy. Different FT-IR spectra of the pyridine-adsorbed titanate materials (298 K) are shown in Figure 3.5. The band at *ca.* 1450 cm⁻¹ was observed for all samples, which corresponds to pyridine that is coordinative bound to Lewis acid sites and confirms that coordinatively unsaturated Ti⁴⁺ sites are present on the surface of these titanate materials. The intense band around 1540 cm⁻¹ due to pyridinium ions formed by Brønsted acid sites was not observed for TiO₂, but was observed for HT-Ti-423, which indicates that the titanate nanotubes possess both Brønsted and Lewis acid sites. In the case of HT-Ti-323 and HT-Ti-473, the peak due to Brønsted acid sites was not detectable, which suggests that the number of Brønsted acid sites on the surface of HT-Ti-323 and HT-Ti-473 is much smaller than that of HT-Ti-423.

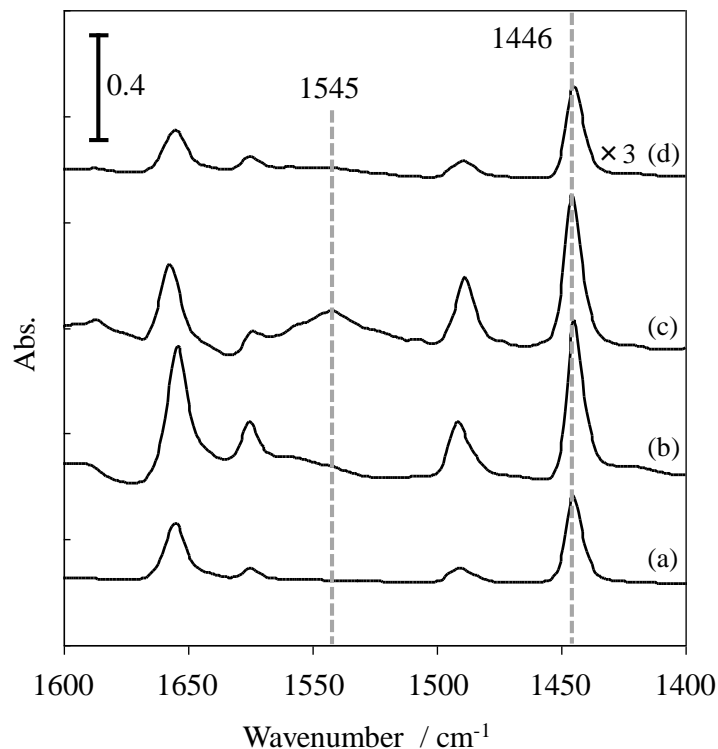


Figure 3.5. Different FT-IR spectra for pyridine-adsorbed (a) TiO_2 , (b) HT-Ti-323, (c) HT-Ti-423, and (d) HT-Ti-473.

The amounts of acid sites and ion-exchange capacities of these samples were determined by FT-IR measurements for pyridine-adsorbed samples and by titration with NaCl and NaOH aqueous solutions, respectively. Table 3.1 shows that the amounts of Lewis acid sites on HT-Ti-323 and HT-Ti-473 are much less than that on HT-Ti-423. The amounts of Brønsted acid sites on these samples were not estimated by FT-IR measurements. However, Na^+ ions were adsorbed on HT-Ti-323 in NaCl aqueous solution ($\text{pH} = 5.0$). This may be due to weak Brønsted acid sites present in HT-Ti-323, on which pyridinium ions are not formed (Figure 3.5). It has been reported that titanate nanosheets are produced by hydrothermal treatment of TiO_2 with NaOH at temperatures below 363 K, but the yield of nanosheets is poor [12]. Thus, it is considered that HT-Ti-323 also consists of TiO_2 nanoparticles and a small amount of titanate nanosheets that have weak Brønsted acid sites [19,21]. The ion-exchange capacity of HT-Ti-423 is much larger than that of HT-Ti-323 because TiO_2 is completely transformed into titanate nanotubes at 423 K during hydrothermal treatment. However, Na^+ ions are

not adsorbed onto TiO₂ and HT-Ti-473 under near neutral conditions (pH = 5.0), which indicates that these materials possess no Brønsted acid sites on their surfaces.

When the titanate materials are immersed into NaOH aqueous solution (pH = 12.7), a large number of Na⁺ ions are adsorbed on all samples because the metal oxide surface is negatively charged under alkaline conditions [28]. As a result, the concentration of Na⁺ ions adsorbed on the titanate materials in NaOH aqueous solution (pH = 12.7) is much higher than that of the case of NaCl aqueous solution (pH = 5.0). As listed in Table 3.2, the Na⁺ concentration was also determined by ICP analysis. These values are very similar to those of ion-exchange capacities estimated by the titration method. Therefore, it was found that the ion-exchange sites of these titanate materials can be estimated by the titration method. The adsorption capacities of the titanate materials increased with increase in the hydrothermal treatment temperature, especially above 423 K. This is attributed to the formation of layered titanate structure such as titanate nanotubes and nanorods, as shown in Fig. 3.3. These layered titanates have a large number of ion-exchange sites in the interlayer spaces and the adsorption capacity of the titanate nanorods is much greater than that of the titanate nanotubes [29,30]. These results indicate that ion-exchange sites in the interlayer spaces of the titanate nanotubes and nanorods do not function as Brønsted acid sites, but those on the surface of the titanate nanotubes do function as Brønsted acid sites.

3.3.3 Catalytic performance

The catalytic performance of the titanate materials was examined through the Friedel-Crafts alkylation of toluene with benzyl chloride. This reaction does not proceed effectively over Brønsted acid catalysts, whereas benzyl toluene is produced mainly on the Lewis acid sites [31]. The results for the Friedel-Crafts alkylation, including acid concentration, are summarized in Table 3.1. For comparison, the results for the layered H₂Ti₃O₇ phase with the same crystal structure as the titanate nanotubes and nanorods are also shown. Since the reactants cannot penetrate into the narrow interlayer

spaces of the layered $\text{H}_2\text{Ti}_3\text{O}_7$, it showed no catalytic activity. In contrast, over all the titanate catalysts, benzyl toluene was produced more than 85% in yield after 1 h of the reaction at 373 K, which indicates that these titanate materials have coordinatively unsaturated Ti^{4+} sites on their surface and function as Lewis acid catalysts for the alkylation reaction. Figure 3.6 shows the time courses of benzyl toluene production over the titanate materials at 300 K. HT-Ti-423 exhibited the highest catalytic performance for the reaction at 300 K among the HT-Ti samples. According to the studies [20,29], such high catalytic performance for titanate nanotubes is attributable to a synergistic effect between Lewis and Brønsted acid sites. On the other hand, TiO_2 showed negligible catalytic activity under the same conditions because TiO_2 has only Lewis acid sites. Furthermore, this reaction did not proceed over HT-Ti-473, which suggests that effective Brønsted acid sites are not exposed on the surface of the titanate nanorods. HT-Ti-323 catalyzed the reaction to some extent due to the presence of both Lewis and Brønsted acid sites (Table 3.1). However, the amount of these acid sites is much less than that of the titanate nanotubes, and thus, the catalytic activity was low.

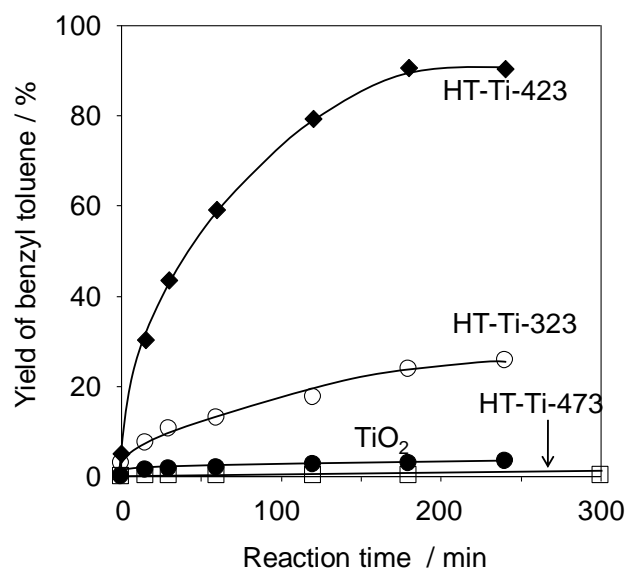


Figure 3.6. Time courses for benzyl toluene formation using various titanium oxide materials. Reaction condition: catalyst (0.2 g), toluene (0.1 mol), benzyl chloride (0.02 mol), reaction temperature (300 K).

To investigate the Brønsted acidity of these titanate materials, the Friedel-Crafts alkylation of anisole with benzyl alcohol was examined. It is generally accepted that Friedel-Crafts alkylation reactions require Brønsted acidity when the alkylating reagent is an alcohol [31]. Figure 3.7 shows that both TiO₂ and HT-Ti-473 exhibited no catalytic activity for this reaction because these materials possess no Brønsted acid sites. In contrast, this reaction is catalyzed over HT-Ti-373 and HT-Ti-423, and the yield of benzyl anisole formation over HT-Ti-423 reached 96% in yield after 5 h. In the initial period of the reaction, not only benzyl anisole but also dibenzylether was formed as an intermediate.

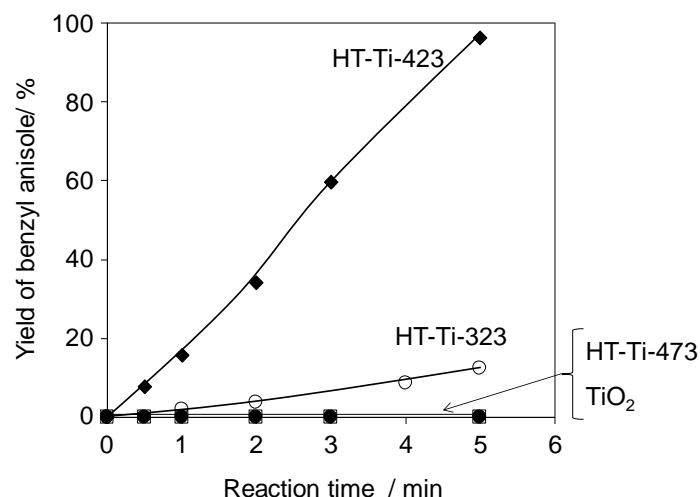


Figure 3.7. Time courses for benzyl anisole formation using various titanium oxide materials. Reaction condition: catalyst (0.2 g), anisole (0.1 mol), benzyl alcohol (0.01 mol), reaction temperature (373 K).

However, the dibenzylether reacted with anisole to form benzyl anisole as reaction time extends as shown in Fig. 3.8. The catalytic activity of HT-Ti-423 is more than 7 times higher than that of HT-Ti-373, corresponding to the difference in the acid concentration between two samples. In addition, the titanate nanotubes could be reused at least three times without a significant decrease in catalytic performance as shown in Fig. 3.9. Assuming that the reaction is catalyzed only on Brønsted acid sites, the turnover number (TON) at 15 h is determined to be 659, indicating that the titanate nanotubes function as stable catalysts for the reaction. These results indicate that the amounts of effective Brønsted acid sites on the titanate nanotubes is much more than those present on the other titanate materials. To further clarify the active sites of the titanate nanotubes, the catalytic performance of Na⁺-exchanged titanate nanotubes was investigated. Before the reaction, the titanate nanotube (HT-Ti-423) was stirred in NaOH aqueous these Friedel-Crafts reaction. These results indicate that the amounts of effective Brønsted acid sites on the titanate nanotubes is much more than those present on the other titanate materials. To further clarify the active sites of the titanate nanotubes, the catalytic performance of Na⁺-exchanged titanate nanotubes was investigated. Before the reaction, the titanate nanotube (HT-Ti-423) was stirred in NaOH aqueous solution at room temperature for 3 h and the amounts of NaOH

added are summarized in Table 3.2. The surface area of the samples was not changed after NaOH treatment (Table 3.3). On the other hand, the catalytic activity decreased with increasing Na⁺ ion adsorbed on the titanate nanotubes, falling to negligible value for 100% Na⁺-exchanged titanate nanotubes in which all Brønsted acid sites are completely exchanged by Na⁺ ions (Fig. 3.10). This result clearly indicates that all Brønsted acid sites of the titanate nanotubes determined by the titration method function as active sites for Friedel-Crafts alkylation of anisole with benzyl alcohol. From these results, it can be concluded that titanate nanotubes with a number of Brønsted acid sites are formed after the hydrothermal treatment of TiO₂ with NaOH at 423 K and subsequent proton exchange. And this material is available as an effective catalyst for these Friedel-Crafts reaction.

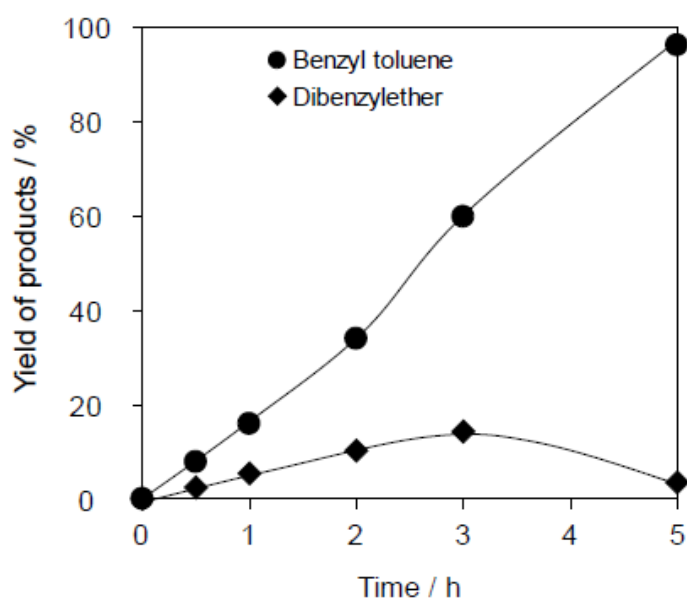


Figure 3.8. Time courses of Friedel–Crafts alkylation of anisole with benzyl alcohol over HT-Ti-423. Reaction condition: catalyst (0.2 g), anisole (0.1 mol), benzyl alcohol (0.01 mol), reaction temperature (373 K).

Table 3.2. Ion exchange capacity of various titanium oxide materials.

Entry	Catalyst	Ion exchange capacity (mmol g ⁻¹)	
		Titration method ^a	ICP-AES
1	TiO ₂ (anatase)	1.0	0.9
2	HT-Ti-323	1.3	1.1
3	HT-Ti-423	2.9	2.6
4	HT-Ti-473	4.4	4.2

^a Ion exchange capacities of these samples were estimated from the exchange of Na⁺ in aqueous 0.05 M NaOH solutions (pH=12.7) by titration method.

Table 3.3. Specific surface area of Na⁺-exchanged titanate nanotube.

Entry	Catalyst	Amount of NaOH	BET surface area
		(mmol g ⁻¹)	(m ² g ⁻¹)
1	Titanate nanotube	0	350
2	Na ⁺ -Titanate nanotube (30%)	0.06	352
3	Na ⁺ -Titanate nanotube (50%)	0.11	348
4	Na ⁺ -Titanate nanotube (70%)	0.15	337
5	^a Na ⁺ -Titanate nanotube (100%)	0.21	339

Numbers in parentheses present the Na⁺ ion exchange ratio of the titanate nanotubes.

^a100 % means that all Brønsted acid sites are replaced by Na⁺ ion.

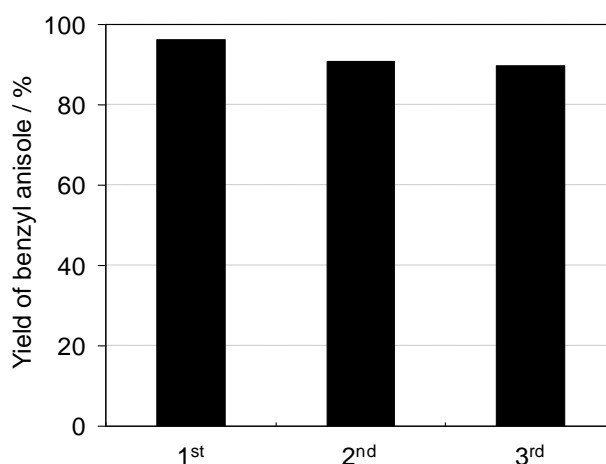


Figure 3.8. Catalytic activity of reused titanate nanotubes (HT-Ti-423) for Friedel-Crafts alkylation of anisole with benzyl alcohol at 373 K. Reaction time of each run is 5 h.

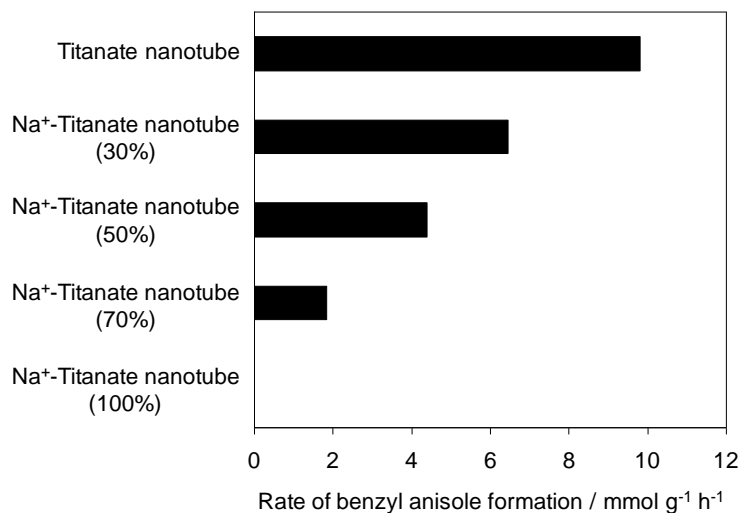


Figure. 3.9 Catalytic activity of Na⁺-exchanged titanate nanotubes (HT-Ti-423) for Friedel-Crafts alkylation of anisole with benzyl alcohol at 373 K.

3.4. Conclusions

TiO₂ nanoparticles were converted into titanate nanotubes (423 K) and nanorods (473 K) after hydrothermal treatment with NaOH aqueous solution. All titanate materials had coordinatively unsaturated Ti⁴⁺ sites on their surfaces and exhibited Lewis acidity. It was demonstrated that the titanate nanotubes possess a large number of Lewis and Brønsted acid sites, so that they can function as efficient acid catalysts for the Friedel-Crafts alkylation of aromatics with benzyl chloride or benzyl alcohol. In contrast, the ion-exchange sites in the interlayer spaces of the titanate nanorods did not function as Brønsted acid sites. Such effective acid sites are only formed on the surface of the titanate nanotubes.

References

- [1] J. Suetake, J.; Nosaka, A. Y.; Hodouchi, K.; Matsubara, H.; Nosaka, Y. *J. Phys. Chem. C*, **2008**, 112, 18474–18482.
- [2] An, H.; Zhu, B.; Li, J.; Zhou, J.; Wang, S.; Zhang, S.; Wu, S.; Huang, W. *J. Phys. Chem. C*, **2008**, 112, 18772–18775.
- [3] Bavykin, D.V.; Lapkin, A.A.; Plucinski, P.K.; Friedrich, J.M.; Walsh, F.C. *J. Catal.*, **2005**, 235, 10–17.
- [4] Nian, J.N.; Chen, S.A.; Tsai, C.C.; Teng, H.S. *J. Phys. Chem. B*, **2006**, 110, 25817–25824.
- [5] Gao, X.P.; Zhu, H.Y.; Pan, G.L.; Ye, S.H.; Lan, Y.; Wu, F.; Song, D.Y. *J. Phys. Chem. B*, **2004**, 108, 2868–2872.
- [6] Zhang, H.; Li, G.R.; An, L.P.; Yan, T.Y.; Gao, X.P.; Zhu, H.Y. *J. Phys. Chem. C*, **2007**, 111, 6143–6148.
- [7] Bavykin, D.V.; Friedrich, J.M.; Walsh, F.C. *Adv. Mater.* **2006**, 18, 2807–2824.
- [8] Wei, M.D.; Konishi, Y.; Zhou, H.S.; Sugihara, H.; Arakawa, H. *J. Electrochem. Soc.*, **2006**, 153, A1232–A1236.
- [9] Kasuga, T.; Hiramatsu, M.; Hoson, A.; Sekino, T.; Niihara, K. *Adv. Mater.* **1999**, 11, 1307–1311.
- [10] Kasuga, T.; Hiramatsu, M.; Hoson, A.; Sekino, T.; Niihara, K. *Langmuir*, **1998**, 14, 3160–3163.
- [11] Chen, Q.; Zhou, W. Z.; Du, G.H.; Peng, L.M. *Adv. Mater.*, **2002**, 14, 1208–1211.
- [12] Bavykin, D.V.; Kulak, A.N.; Walsh, F.C. *Cryst Growth Des.* **2010**, 10, 4421–4427.
- [13] Papa, A.-L.; Millot, N.; Saviot, L.; Chassagnon, R.M.; Heintz, O. *J. Phys. Chem. C*, **2009**, 113, 12682–12689.
- [14] Bavykin, D.V.; Walsh, F.C. *Eur. J. Inorg. Chem.*, **2009**, 977–997.
- [15] Saponjic, Z.V.; Dimitrijevic, N.M.; Tiede, D.M.; Goshe, A.J.; Zuo, X.B.; Chen, L.X.; Barnard, A.S.; Zapol, P.; Curtiss, L.; Rajh, T. *Adv. Mater.*, **2005**, 17, 965–971.
- [16] Wu, D.; Liu, J.; Zhao, X.; Li, A.; Chen, Y.; Ming, N. *Chem. Mater.*, **2006**, 18, 547–553.
- [17] Kukovecz, A.; Hodos, N.; Horvath, E.; Radnoczi, G.; Konya, Z.; Kiricsi, I. *J. Phys. Chem. B*, **2005**, 2005, 17781–17783.
- [18] Zhang, S.; Peng, L.M.; Chen, Q.; Du, G.H.; Dawson, G.; Zhou, W. Z. *Phys. Rev. Lett.*, **2003**, 91, 256103–256104.
- [19] Kitano, M.; Nakajima, K.; Kondo, J.N.; Hayashi, S.; Hara, M. *J. Am. Chem. Soc.*, **2010**, 132, 6622–6623.
- [20] Kitano, M.; Wada, E.; Nakajima, K.; Hayashi, S.; Miyazaki, S.; Kobayashi, H.; Hara, M. *Chem. Mater.*, **2013**, 25, 385–393.
- [21] Dias, A.S.; Lima, S.; Carriazo, D.; Rives, V.; Pillinger, M.; Valente, A. A. *J. Catal.*, **2006**, 244, 230–237.
- [22] Nakajima, K.; Baba, Y.; Noma, R.; Kitano, M.; Kondo, J. N.; Hayashi, S.; Hara, M. *J. Am. Chem. Soc.*, **2011**, 133, 4224–4227.
- [23] Tsai, C. C.; Teng, H. S. *Chem. Mater.*, **2006**, 18, 367–373.

- [24] Ma, R.Z.; Bando, Y.; Sasaki, T. *Chem. Phys. Lett.*, **2003**, 380, 577–582.
- [25] R. Yoshida, Y. Suzuki, S. Yoshikawa, *J. Solid State Chem.*, **2005**, 178, 2179–2185.
- [26] Gao, T.; Fjellvag H.; Norby, P. *Inorg. Chem.*, **2009**, 48, 1423–1432.
- [27] Feist, T.P.; Davies, P.K. *J. Solid State Chem.*, **1992**, 101, 275–295
- [28] Vallar, S.; Houivet, D.; Fallah, J. E.; Kervadec, D.; Haussonne, J.M. *J. Eur. Ceram. Soc.*, **1999**, 19, 1017–1021.
- [29] Sun, X.M.; Li, Y.D. *Chem. Eur. J.*, **2003**, 9, 2229–2238.
- [30] Li, N.; Zhang, L.D.; Chen, Y.Z.; Fang, M.; Zhang, J.X.; Wang, H. M. *Adv. Funct. Mater.*, **2012**, 22, 835–841.
- [31] Corma, A.; Garcia, H. *Chem. Rev.*, **2003**, 103, 4307–4365.

Chapter 4

Effect of Nb doping into Protonated Titanate Nanotubes for Catalytic Activity and Acidity

Abstract

Niobium doped titanate nanotubes (Nb-TiNT) with various Nb content were prepared by hydrothermal treatment of Nb-doped TiO₂ with NaOH aqueous solution and subsequent proton exchange. Nb-TiNT effectively catalyzed Friedel-Crafts alkylation of toluene with benzyl chloride or benzyl alcohol and the activity increased with increasing Nb content, reaching a maximum at 5%. Furthermore, Nb-TiNT showed much higher catalytic activity than other Nb-containing solid acid catalysts such as Nb₂O₅·*n*H₂O, Nb-Ti mixed oxides, and Nb-Ti nanosheet materials. FT-IR measurement revealed that Nb-TiNT possess both Lewis and Brønsted acid sites and these acid amounts are comparable to those of non-doped TiNT. On the other hand, the Brønsted acid strength of Nb-TiNT is slightly higher than that of TiNT. Kinetic experiments indicate that the formation of benzyl cations is promoted on the surface of Nb-TiNT.

4.1. Introduction

Solid acid catalysts have been widely investigated for the environmentally benign synthesis of bulk and fine chemicals because it is reusable and readily separable from the reaction solution [1,2]. Titanium dioxide (TiO₂), which is abundant, stable, and nontoxic material, has attracted attention as a support material for metal catalysts [3], photocatalysts [4], pigment, food additives, and dye-sensitized solar cell [5]. However, relatively few studies have been reported on solid acid catalysis of TiO₂ itself since it has moderate acid strength ($H_0 < -3$) and the acid amount is very small [6]. It has been demonstrated that protonated titanate nanotubes functions as efficient acid catalysts for Friedel-Crafts alkylation of toluene with benzyl chloride or benzyl alcohol, and found that the catalytic activity is much higher than that of other titanate materials, such as TiO₂, layered titanates, titanate nanosheets, and titanate nanorods [7]. Coordinatively unsaturated Ti⁴⁺ sites and bridged Ti–OH–Ti sites on the surface of the nanotubes act as Lewis and Brønsted acid sites, respectively [8,9]. And the Brønsted acidity of the nanotubes is improved by the lattice distortion due to the scrolling of the nanosheets. To

date, attempts have been made to clarify the relationship between catalytic activity and physicochemical properties of the titanate nanotubes [7,8]. In order to improve the catalytic activity of the nanotubes, effects of metal cation doping into titanate nanotube was investigated. Niobium oxide is well known as a stable and strong solid acid catalyst ($H_0 < -5.6$) for many reactions such as dehydration, hydration, esterification, hydrolysis, and alkylation [10]. Many researchers have widely investigated niobium-containing solid acid catalysts, such as $Nb_2O_5 \cdot nH_2O$ [11,12], HTiNbO₅ nanosheet [13], Nb_2O_5/Al_2O_3 calcined at high temperatures [14,15], and layered-structure-type niobium oxides [16]. Takagaki *et al.* reported that bridging hydroxyl groups, Nb(OH)M (M: Ti, Nb, Mo, W), function as strong Brønsted acid sites and the acidity increases with the cation valence [17]. From this viewpoint, it can be expected that Brønsted acidity of the titanate nanotubes is improved by Nb⁵⁺ cation doping.

In this chapter, Nb-doped titanate nanotubes were synthesized with various Nb content by hydrothermal treatment of Nb-doped TiO₂ with NaOH, and acid properties of the nanotubes were evaluated by Fourier transform infrared (FT-IR) spectroscopy and ³¹P magic angle spinning nuclear magnetic resonance (³¹P MAS NMR). Friedel-Crafts alkylations of toluene with benzyl chloride or benzyl alcohol were employed to evaluate the catalytic performance.

4.2. Experimental

4.2.1 Preparation of catalysts

Nb-doped TiO₂ (Nb-TiO₂) was prepared by a sol-gel method according to a similar procedure described in the literature [18]. First, titanium tetraisopropoxide (Ti(OC₄H₉)₄) and niobium pentaethoxide (Nb(OC₂H₅)₅) were dissolved into ethanol (92 ml). The Nb/Ti ratio adjusted to 0.01–0.10. Then, the mixed solution was added drop by drop to 250 ml of a solution of ethanol/water 1:1 under stirring at room temperature. The obtained white precipitate was washed with distilled water and dried at 353 K for 2 days. Then, the powder was heated at 773 K for 4 h. Nb-doped titanate nanotubes

(Nb-TiNT) were synthesized by hydrothermal treatment of Nb-TiO₂ powders in NaOH aqueous solution. 2.0 g of Nb-TiO₂ powder and 70 mL of 10 M NaOH aqueous solution were mixed into a Teflon-lined stainless autoclave, and the autoclave was heated at 393 K for 20 h. After the hydrothermal treatment, the mixed solution was neutralized and the white precipitates were filtrated and proton exchanged in 0.1 M HNO₃ aqueous solution (pH = 1.0) for 24 h. The obtained materials were washed with distilled water several times, and dried overnight at 353 K. These samples referred to as Nb(X%)-TiNT [X: Nb contents]. Nb-oxide deposited TiNT was prepared by the impregnation method (imp-Nb(5%)-TiNT): TiNT powder is immersed into Nb(OC₂H₅)₅/ethanol solution in which Nb content is 5 atomic percent. After the deposition, the resultant powder was washed with 0.1 M HNO₃ aqueous solution (pH = 1.0) several times and rinsed with distilled water. The HTiNbO₅ and HTi₂NbO₇ nanosheets were prepared according to the procedure described in the literature [13].

4.2.2 Characterization

The crystal structures of the obtained samples were studied by an X-ray diffractometer (XRD; Ultima IV, Rigaku) using Cu K α radiation (40 kV, 40 mA) with a wavelength of $\lambda = 1.54 \text{ \AA}$ at a scan rate of $2.0^\circ \text{ min}^{-1}$ over the 2θ range of $10\text{--}60^\circ$. The surface Nb/Ti ratio was determined by X-ray photoelectron spectroscopy (XPS, ESCA-3200, Shimadzu) and the bulk Nb/Ti ratio was estimated by inductively coupled plasma atomic emission spectrometry (ICP-AES, ICPS-8100, Shimadzu). Surface morphologies of the samples were investigated by high-resolution scanning electron microscope (FE-SEM; S-4700, HITACHI) and transmission electron microscope (FE-TEM; EM002BF, TOPCON) equipped with an energy dispersive X-ray spectroscopy (EDS). The Brunauer-Emmet-Teller (BET) specific surface area and Barrett-Joyner-Halenda (BJH) particle size distribution of the samples were determined from nitrogen adsorption-desorption isotherms measured at 77 K using an automatic gas adsorption instrument (NOVA 4200e, Quantachrome) after evacuation of the sample at 423 K. The amounts of acid sites on all samples were estimated by FT-IR (FT/IR-6100, JASCO) spectroscopy for

pyridine adsorbed samples at 298 K according to the previous literatures [7,12]. FT-IR spectra were measured with a spectrometer equipped with a mercury cadmium telluride (MCT) detector at a resolution of 4 cm⁻¹. ³¹P MAS NMR spectra for samples with adsorbed trimethylphosphine oxide (TMPO) were measured at room temperature. A single pulse sequence was employed with high-power proton decoupling. Bruker MAS probe heads were used with a 4 mm zirconia rotor. The spinning rate of the sample was set at 10 kHz. The ³¹P chemical shift was referenced to 85% H₃PO₄ at 0.0 ppm. (NH₄)₂HPO₄ was employed as a second reference material with the signal set at 1.33 ppm. TMPO-adsorbed samples were prepared by evacuated dehydration at 423 K for 1 h, followed by immersion in a dichloromethane solution of TMPO at room temperature for 1 day under argon. After evacuation to remove the solvent, the samples were packed into the rotor under a N₂ atmosphere.

4.2.3 Acid catalytic reaction

The catalytic performance of the samples was investigated through the Friedel-Crafts alkylation reactions. The reaction was performed in a liquid phase using 0.20 g of the catalyst, 0.1 mol of toluene, 0.05 mol of benzyl chloride or 0.01 mol of benzyl alcohol. Prior to the reaction, all catalysts were evacuated at 423 K for 1h to remove the adsorbed water on the catalyst surface and expose Lewis acid sites, and then the reaction was carried out under argon atmosphere. The reaction vessel was placed in an oil bath maintained at 300 or 373 K for the duration of 0.5–5 h reaction. The products were analyzed by gas chromatography (GC-17A, Shimadzu) with a DB-EFAP capillary column and a flame ionization detector.

4.3. Results and Discussion

4.3.1 Structures

Figure 4.1 shows XRD patterns of Nb(5%)-TiO₂ and Nb-TiNTs with various Nb content. Nb-TiO₂ shows a typical anatase structure without any other detectable phase. Nb(5%)-TiO₂ mainly consists of anatase structure. After the hydrothermal treatment at 393 K for 20 h, the anatase phase was completely disappeared and broad peaks attributed to the titanate-like phase were observed at $2\theta = 10.7, 24.7, 28,$ and 48° . These peaks are well consistent with those of TiNT without Nb. However, the intensity of (200) peaks of Nb-TiNTs is much weaker than that of TiNT, implying that the titanate layers are stacked in a random fashion. Furthermore, Nb-oxide phase was not observed for all XRD patterns, suggesting that Nb species would be well dispersed on the titanate nanotubes or would exist as an amorphous form.

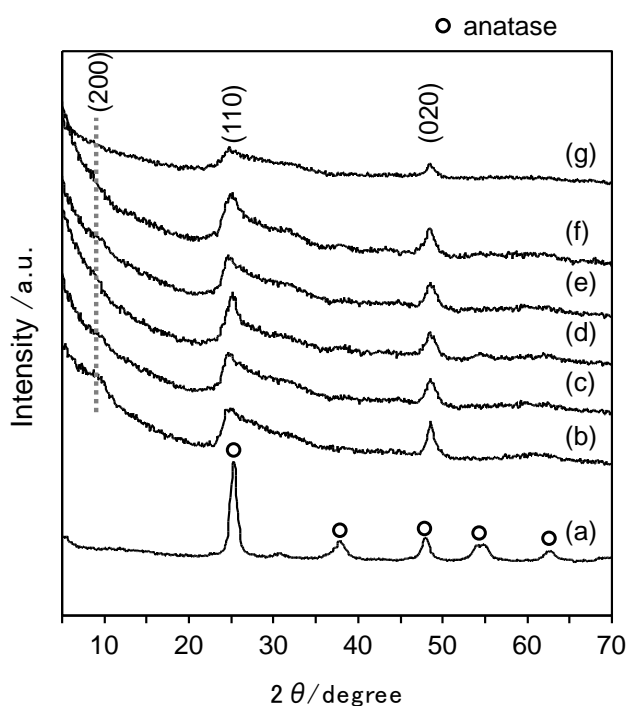


Figure 4.1. XRD patterns of (a) Nb(5%)-TiO₂, (b) TiNT, (c) Nb(1%)-TiNT, (d) Nb(3%)-TiNT, (e) Nb(5%)-TiNT, (f) Nb(7%)-TiNT, and (g) Nb(10%)-TiNT.

Table 4.1 summarizes the Nb/Ti ratio of Nb-TiNTs determined by ICP-AES and XPS analyses. The Nb/Ti ratios determined by ICP-AES analysis were comparable to the mixing ratios of Nb(OC₂H₅)₅ to Ti(OC₄H₉)₄. On the other hand, the Nb/Ti ratios estimated by XPS were higher than that of ICP-AES by a factor of 2. This result indicates that not all Nb atoms are doped into the titanate lattice and excess amount of Nb species were formed on the surface as amorphous Nb-oxides.

Table 4.1. Nb contents of Nb-TiO₂ and Nb-TiNTs measured by ICP-AES and XPS.

Catalyst	Nb/Ti ratio	
	ICP-AES	XPS
Nb(1%)-TiO ₂	0.8	1.6
Nb(1%)-TiNT	0.9	1.7
Nb(5%)-TiO ₂	4.7	9.2
Nb(5%)-TiNT	4.9	10
Nb(10%)-TiO ₂	11	20
Nb(10%)-TiNT	10	25

The morphologies of the synthesized samples were characterized by using SEM and TEM. Figure 4.2 shows the high-resolution SEM images of the Nb-doped titanate materials. In Nb-TiO₂ powders, small nanoparticles are somewhat agglomerated with the average grain size of about 10–20 nm as shown Fig. 4.3. In Nb-TiNT, nanotube structure with inner diameter of *ca.* 6 nm and outer diameter of *ca.* 10 nm was observed in the TEM image as shown Fig. 4.4 although it is difficult to identify each nanotube because of the considerable overlapping of the nanotubes. Non-doped TiNT is mainly composed of nanotubes with high aspect ratios, however, all Nb-TiNT samples have a distorted nanotube structure and nanosheets are also observed, which is consistent with previous results [18,19].

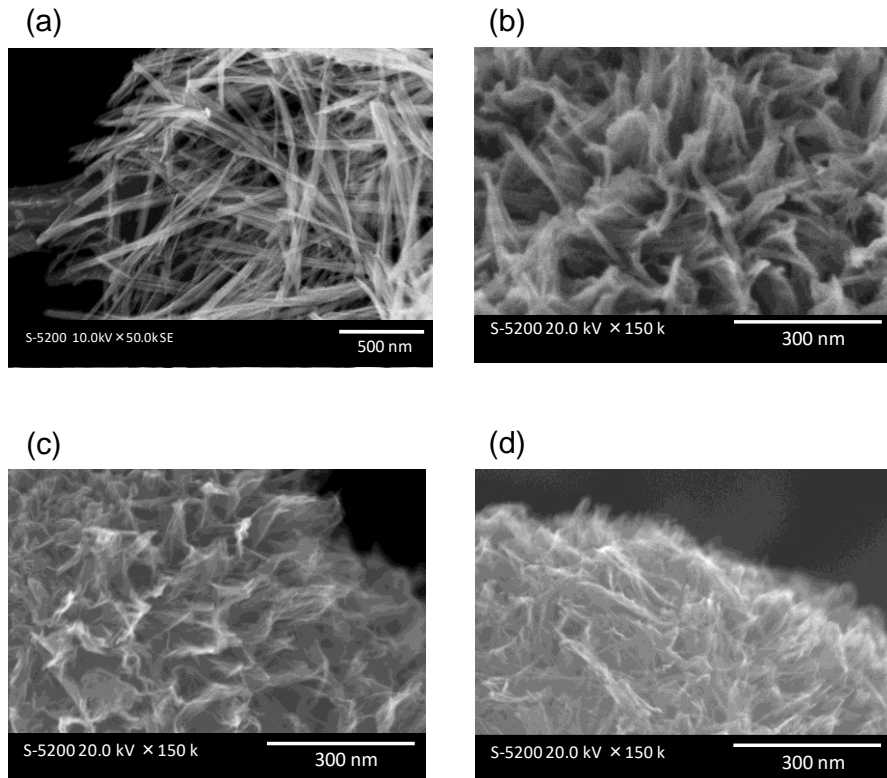


Figure 4.2. High- resolution SEM images of (a) TiNT, (b) Nb(1%)-TiNT, (c) Nb(5%)-TiNT, and (d) Nb(10%)-TiNT.

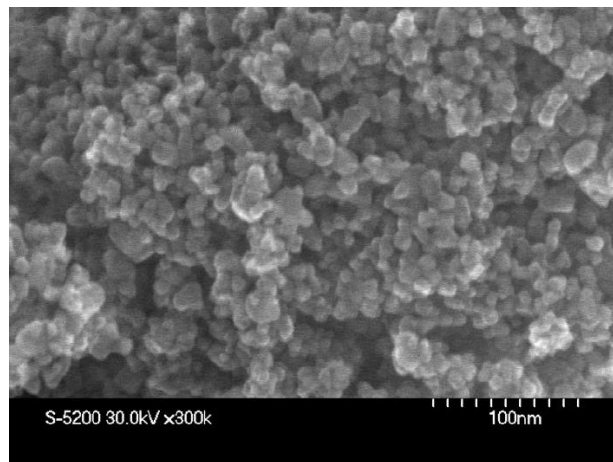


Figure 4.3. SEM images of Nb(5%)-TiO₂ sample

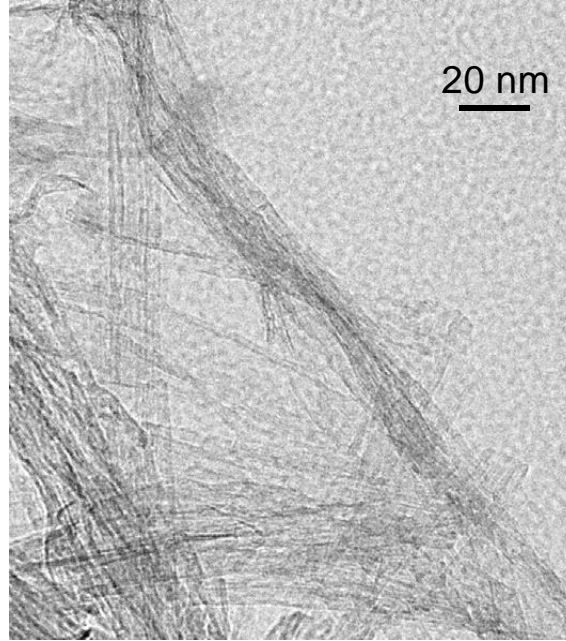


Figure 4.4. TEM image of Nb(5%)-TiNT sample.

Nikolić *et al.* reported that Nb-doped nanotubes were prepared by the similar hydrothermal method using Nb-doped TiO₂ with anatase crystal phase as a starting material [19]. In this literature, nanosheets with cuted edges are formed at the short treatment time (within 10 h), and finally nanotube structure is produced after 20 h. On the other hand, Liu *et al.* reported that Nb-doped nanorods are prepared from the mixture of TiO₂ and Nb₂O₅ powders by hydrothermal treatment at 393 K for 40 h. Here, ideal surface area per unit weight of a tube (S_{tube}) and rod (S_{rod}) is estimated to discuss the possibility of nanorod formation. The calculation of S_{tube} was according to the equation 2-1, in Chapter 2, while S_{rod} was estimated from the following expression:

$$S_{\text{rod}} = [2\pi r_o l + 2\pi r_o^2] / [r_o^2 \pi l d] \quad (4-1)$$

where r_o is the outer radius of the rod, l is the length of the rod, and d is the density of the material, respectively. S_{tube} is calculated to be 317.5 m² g⁻¹ for the nanotubes, using $r_o = 5$ nm, $r_i = 3$ nm, $d = 3.2$ g cm⁻³, and $l = 1000$ nm (Fig. 4.5a). In contrast, S_{rod} is calculated to be 127.4 m² g⁻¹ (Fig. 4.5b), which is much smaller than the experimental values (Table 4.2). Therefore, it can be concluded that Nb-doped TiNT mainly consists of the nanotube. However, the possibility of the nanosheet formation cannot be

ruled out. As for Nb-TiNTs, anatase nanoparticles completely transform into the layered titanates. Considering SEM and TEM images and results of surface area calculations, all Nb-TiNTs have a nanotube structures, though nanosheet structure would be partially formed.

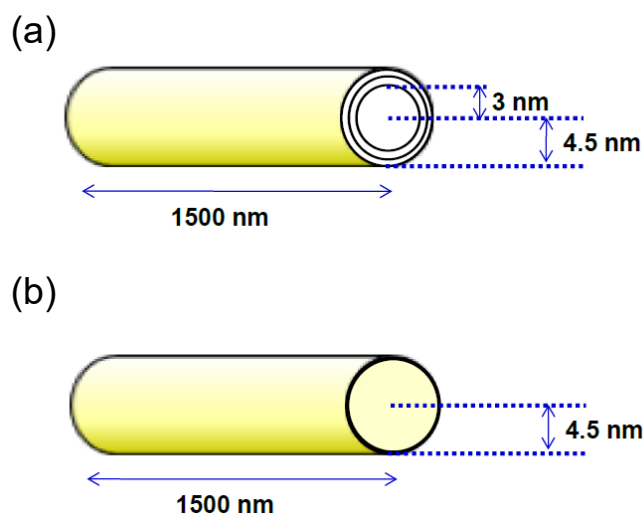


Figure 4.5. Schematic showing an ideal (a) nanotube and (b) nanorods model.

TEM images with EDS elemental mapping of Nb and Ti in Nb-TiNT are displayed in Fig. 4.6. When 1% of Nb was doped into TiNT, Nb species were dispersed uniformly on the nanotubes. In the case of Nb(10%)-TiNT, aggregated Nb compounds were formed and the yield of nanotube was much lower than that of Nb(1%)-TiNT, which is well consistent with the XPS results. These results clearly indicate that the formation of the nanotubes from the nanosheets during hydrothermal treatment is prevented by the presence of Nb species.

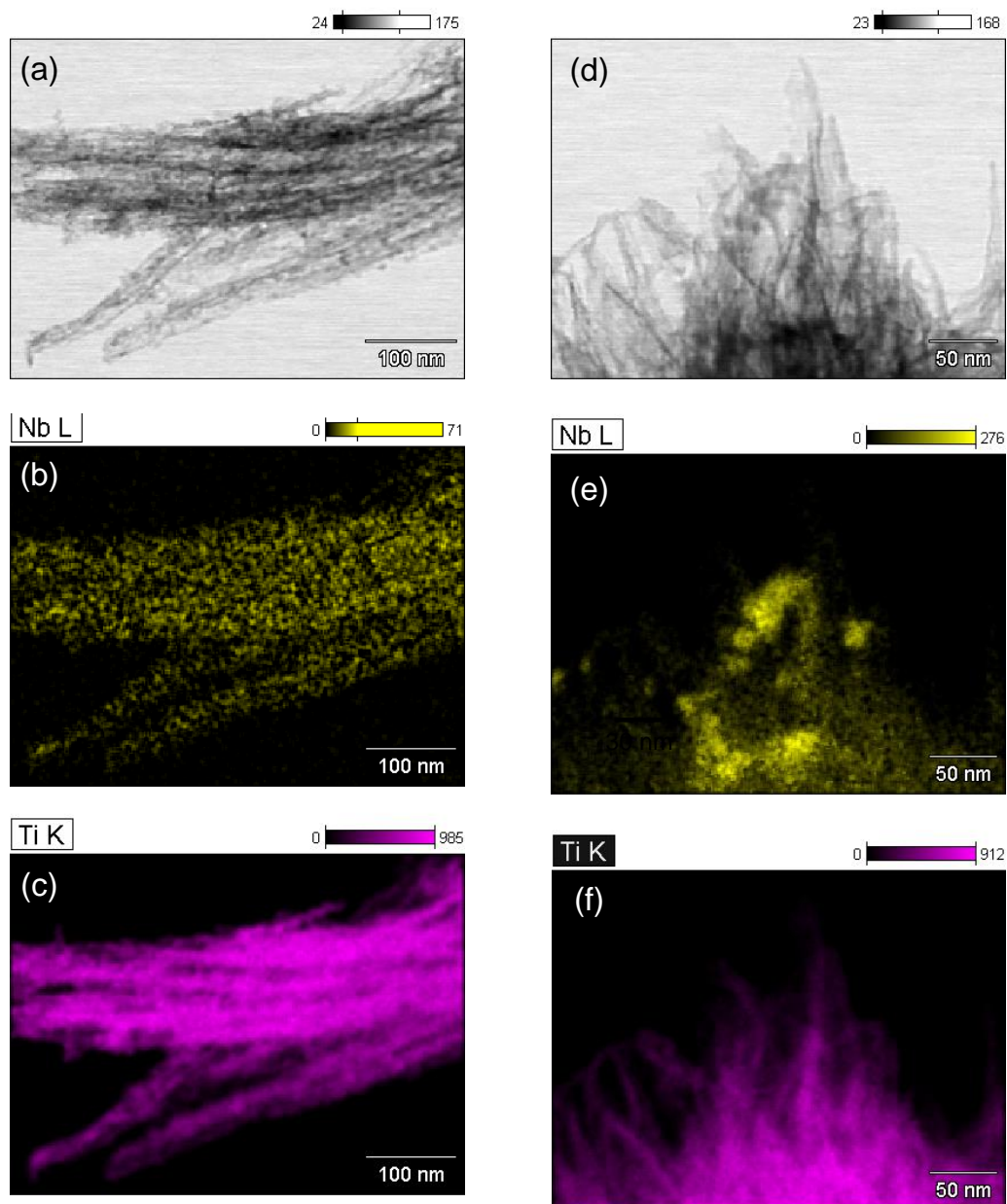


Figure 4.6. TEM image (a) Nb(1%)-TiNT and its elemental mapping of (b) Nb and (c) Ti. TEM image (d) Nb(10%)-TiNT and its elemental mapping of (e) Nb and (f) Ti.

Nitrogen adsorption-desorption analysis was performed to investigate the surface area and pore size distribution of the Nb-TiNTs. Figure 4.7 shows BJH pore size distribution curves for Nb-TiNTs, and the surface areas and total pore volumes are summarized in Table 4.2. Nb-TiNTs with Nb content higher than 3% exhibited narrower pore size distribution as compared with non-doped TiNT.

Furthermore, the surface area slightly increased and the pore volume slightly decreased with Nb content. These results may be associated with the generation of lots of nanosheets and the formation of Nb-oxide on the surface. However, all samples have single pore size distributions in the mesopore range, which corresponds to the size of pores inside the nanotubes.

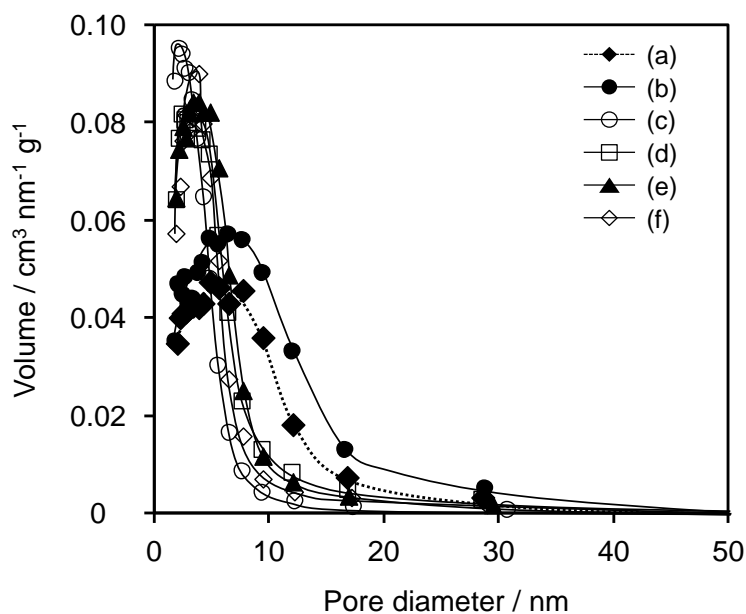


Figure 4.5. BJH pore size distributions of (a) TiNT, (b) Nb(1%)-TiNT, (c) Nb(3%)-TiNT, (d) Nb(5%)-TiNT, (e) Nb(7%)-TiNT, and (f) Nb(10%)-TiNT.

Table 4.2. Surface are and pore volume of various titanate materials.

Catalyst	Surface area (m ² g ⁻¹)	Total pore volume (cm ³ g ⁻¹)
TiNT	350	0.63
Nb(1%)-TiNT	388	0.87
Nb(3%)-TiNT	423	0.40
Nb(5%)-TiNT	431	0.60
Nb(7%)-TiNT	457	0.58
Nb(10%)-TiNT	438	0.50

4.3.2 Catalytic performance

Catalytic performance of Nb-TiNTs was examined through Friedel-Crafts alkylation of toluene with benzyl chloride at 300 K (Fig. 4.8). As reported previously, TiNT exhibits much higher catalytic activity for this reaction at 300 K than conventional solid acid catalysts such as ion-exchange resins, zeolite, and niobic acid [7,8]. After Nb-doping, the catalytic activity is greatly enhanced and the benzyl toluene formation rate strongly depends on the Nb concentration. The maximum catalytic activity was observed for Nb(5%)-TiNT, but further increase in Nb doping resulted in decline in activity. This is due to the low catalytic activity of Nb oxides species on TiNT, which was observed TEM-EDX measurement, for this reaction at 300 K. As shown in Fig. 4.6, aggregated Nb-oxide species are formed on the surface of Nb(10%)-TiNT. Therefore, the Nb-oxide species may prevent the alkylation reaction over Nb-TiNT surface. Regardless of Nb-doping, both of *p*- and *o*-benzyl toluene were produced and the selectivity was not influenced by Nb-doping. Although this reaction proceeds effectively over Lewis acid sites rather than Brønsted acid sites [21], recent study suggests that Brønsted acid sites of TiNT promote the carbocation formation on the Lewis acid sites [8]. Therefore, these results imply that Brønsted acidity of TiNT may be improved by Nb-doping.

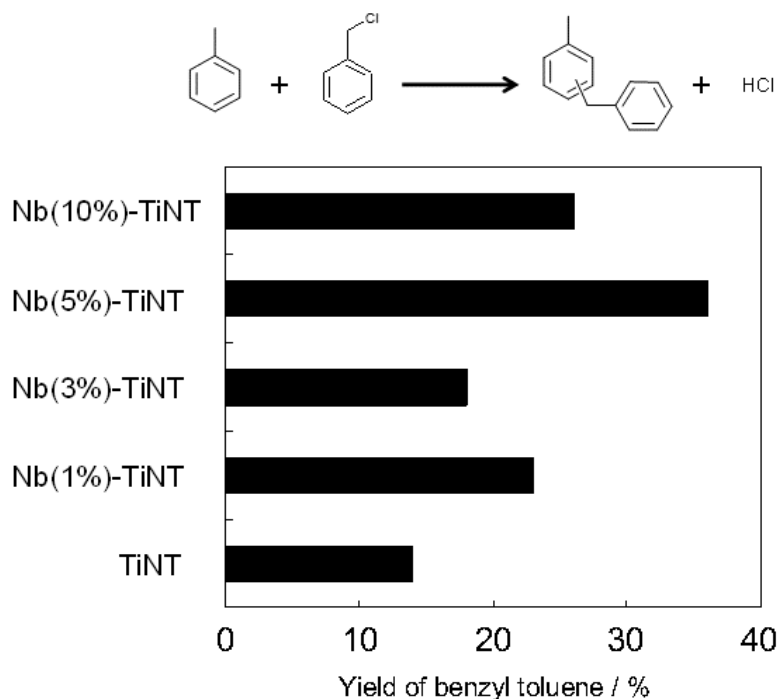


Figure 4.8. Benzyl toluene formation using titanate nanotube and Nb-doped titanate nanotubes. [Reaction conditions: catalyst (0.2 g), toluene (0.1 mol), benzyl chloride (0.05 mol), reaction temperature (300 K), reaction time (1h)]

The Friedel-Crafts alkylation of toluene with benzyl alcohol was also examined as a test reaction to investigate the Brønsted acidity of Nb-TiNT (Fig. 4.9). It is generally accepted that Friedel-Crafts alkylation reactions require Brønsted acidity when the alkylating reagent is an alcohol [22,23]. Ti-based oxide is not used as a solid acid catalyst for this type reaction because the acidity of Ti-based oxide is not high [6]. In fact, TiNT shows moderate catalytic activity. On the other hand, the catalytic activity of Nb-TiNT increased significantly with the Nb content, reaching a maximum at 5%, beyond which the catalytic activity began to decline. Nb(5%)-TiNT exhibits catalytic activity that is approximately 10 times higher than that for non-doped TiNT, which indicates that Nb-doping of TiNT accounts for the generation of effective Brønsted acid sites. Figure 4.10 shows the reaction time profiles of the Friedel-Crafts alkylation of toluene with benzyl alcohol over various Nb-containing solid acid catalysts. In the initial period of the reaction, dibenzyl ether is preferably formed as an intermediate (Fig. 4.10b).

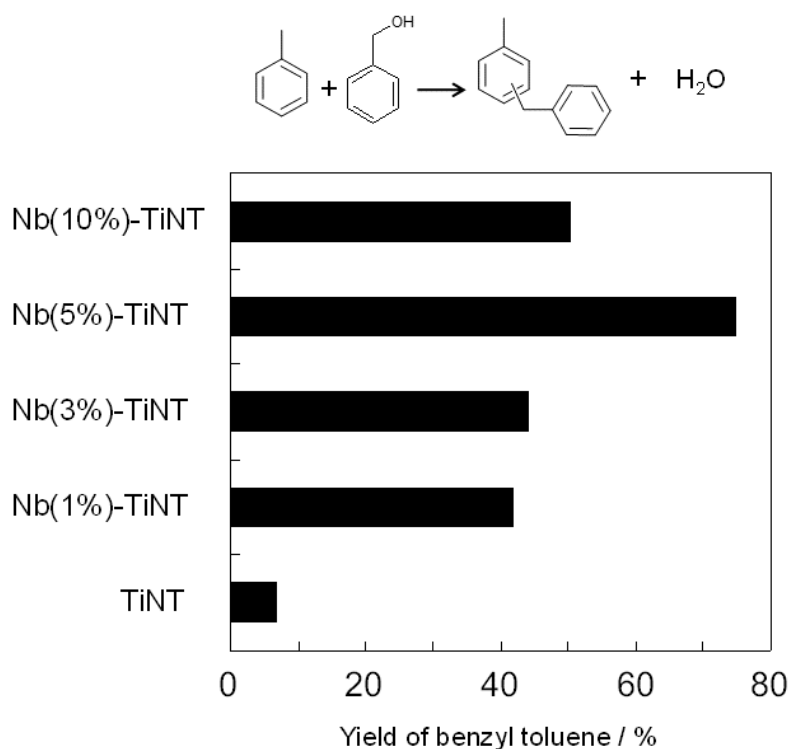


Figure 4.9. Benzyl toluene formation using TiNT and Nb-TiNTs.

Reaction conditions: catalyst (0.2 g), toluene (0.1 mol), benzyl alcohol (0.01 mol), reaction temperature (373 K), reaction time (5h)

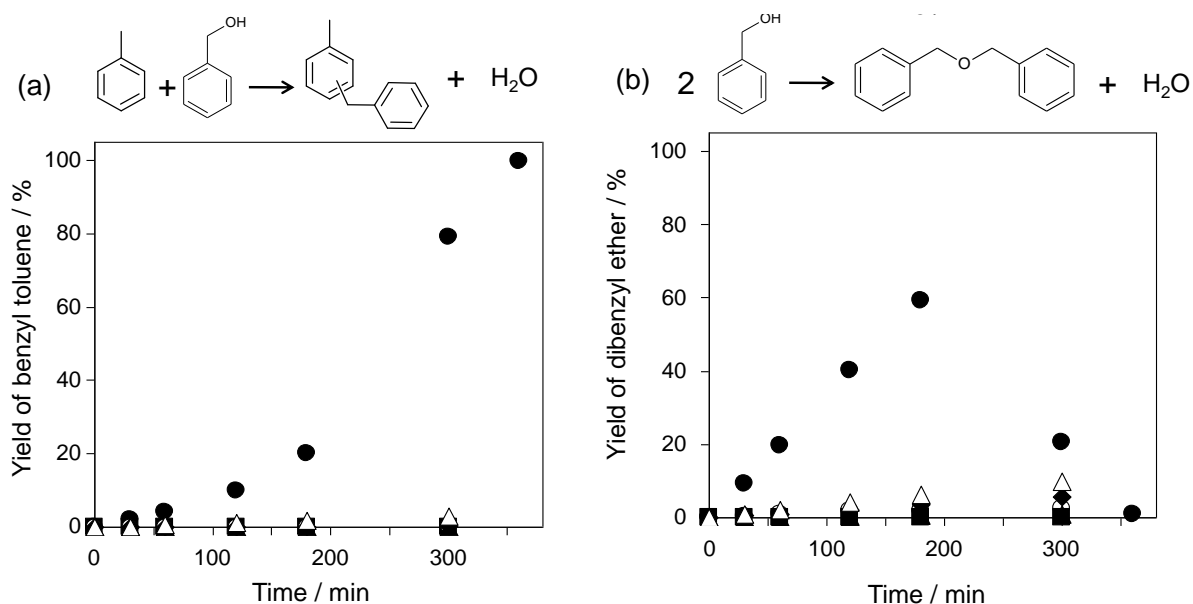


Figure 4.10. Time courses for benzyl toluene formation over Nb-TiNT and Nb-containing catalysts.

(●):Nb(5%)-TiNT, (◆): HTi₂NbO₇ nanosheet, (▲):HTiNbO₅ nanosheet, (○): Nb₂O₅·nH₂O, (■): imp-Nb(5%)-TiNT, (△):Nb(5%)-TiO₂. Reaction conditions: catalyst (0.2 g), toluene (0.1 mol), benzyl alcohol (0.01 mol), reaction temperature (373 K).

Dibenzyl ether, which is produced by the dehydration of two benzyl alcohol molecules in the presence of H^+ [23], then reacts with toluene to afford benzyl toluene as the reaction time extends. The possible reaction mechanism is described in Fig. 4.11.

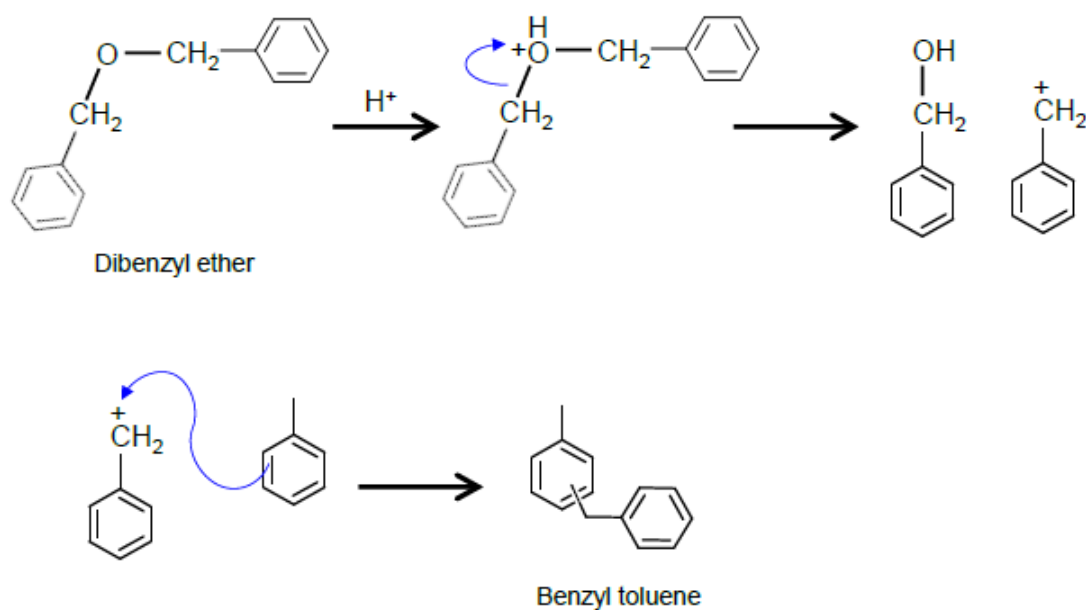


Figure 4.11. Possible reaction mechanism of the formation of benzyl toluene with dibenzyl ether in the presence of protonic acid catalyst.

It is reported that dibenzyl ether is converted into anthracene as a major product in addition to toluene, benzaldehyde, and water in the presence of alumina based solid acid under high temperature (573 K) [18,22]. However, in this case, such by-products cannot be observed and the yield of benzyl toluene reaches >99% after the reaction of 6 h (Fig. 4.10a). It is important to note that only Nb-TiNT exhibits outstanding catalytic activity, although all catalysts are composed of Nb oxide or Nb-Ti mixed oxides. On the other hand, the alkylation reaction did not proceed to a significant extent and only small amounts of dibenzyl ether were formed over HTi_2NbO_7 , $HTiNbO_5$ nanosheets, and niobic acid ($Nb_2O_5 \cdot nH_2O$), which are well-known solid acid catalysts. Generally, niobium oxide-based materials work as efficient catalysts for the alkylation of toluene or anisole with benzyl alcohol as shown in

Table 4.3. In most cases, the high catalytic performance can be obtained only for the alkylation of anisole with benzyl alcohol at high reaction temperatures (> 400 K).

Table 4.3. The catalytic performance of Nb-based catalysts for the alkylation of aromatics with benzyl alcohol.

Catalyst	Substrate	Reaction temperature (K)	Time (h)	Yield (%)	Ref.
Nb(5%)-TiNT	toluene	373	6	100	This work
Nb ₂ O ₅ ·nH ₂ O	anisole	Reflux temperature ^a	9	37.6	23
Nb ₂ O ₅ ·nH ₂ O	toluene	Reflux temperature ^b	9	3.3	23
H ₃ PO ₄ treated Nb ₂ O ₅ ·nH ₂ O	anisole	Reflux temperature ^a	9	85.2	23
H ₃ PO ₄ treated Nb ₂ O ₅ ·nH ₂ O	toluene	Reflux temperature ^b	9	31.8	23
Mesoporous Nb-oxide	anisole	Reflux temperature ^a	9	80	24
Sulfated Mesoporous Nb-oxide	anisole	Reflux temperature ^a	0.5	100	24
Nb ₂ O ₅ /Al ₂ O ₃	anisole	413	3	50	15
Layered niobium oxide	anisole	373	2	36.4	16
HTiNbO ₅ nanosheets	anisole	373	2	0	17
HNb ₃ O ₈ nanosheets	anisole	373	2	1.8	17

^a The temperature would be higher than 423 K because the boiling temperature of anisole and benzyl alcohol is 426.8 K and 478 K, respectively.

^b The temperature would be higher than 383 K because the boiling temperature of toluene is 383.6 K

It has been reported that these materials do not effectively catalyze the alkylation of anisole with benzyl alcohol under almost the same reaction conditions as in Fig. 4.8 [17,22,26]. In contrast, Nb-TiNT exhibited much higher catalytic activity at a lower temperature (373 K) for the alkylation reaction using a toluene instead of an anisole. Benzyl alcohol reacts more easily with anisole in the presence of a Brønsted acid than with toluene because of aromatic ring activation by electron donating effects

($-\text{OCH}_3 > -\text{CH}_3$) [27]. In fact, the catalytic activity of $\text{Nb}_2\text{O}_5 \cdot n\text{H}_2\text{O}$ is about 10 times higher for the alkylation of anisole with benzyl alcohol than the case of toluene (Table 4.3). These results clearly indicate that Nb species doped into TiNT play a significant role in the enhancement of Brønsted acidity (acid amount and/or acid strength). The enhancement of the Brønsted acidity is not due to the formation of niobic acid-like structure on the TiNT because both niobic acid and Nb-oxide deposited on TiNT exhibited negligible catalytic activity (Fig. 4.10). In addition, the amorphous Nb-Ti mixed oxide catalyst also shows low catalytic activity. These results clearly indicate that the high catalytic performance of Nb-TiNT is attributed to the Nb species substituted into the lattice of TiNT. However, it cannot be ruled out the possibility of the formation of monolayer-like Nb_2O_5 as demonstrated in $\text{Nb}_2\text{O}_5/\text{Al}_2\text{O}_3$ catalysts [14,15]. As shown in Table 4.1, XPS and ICP-AES analyses indicate that not all Nb atoms are doped into TiNT lattice and Nb-oxide is partially covered on the surface of TiNT. It can be considered that both Nb- and Ti-oxide are dissolved in conc. NaOH during the hydrothermal treatment and Nb substituted TiNT are formed by the scrolling of Nb-substituted titanate nanosheet via the formation of the nanosheet as an intermediate. At the same time, monolayer-like Nb_2O_5 may be produced on the surface of the nanotubes, leading to the nanotube structure (Fig. 4.2). At present, it cannot be determined which Nb species are active sites for the alkylation reaction. Table 4.4 summarizes the results for the Friedel-Crafts alkylation of toluene with benzyl alcohol over various solid acid catalysts. Nb-TiNT exhibits higher catalytic activity than most of solid acid catalysts tested, and the activity is comparable to that of Nafion NR 50 and Nafion SAC13, which are well known as heterogeneous Brønsted acids having sulfo group.

Table 4.4. Friedel-Crafts alkylation over various solid acid catalysts. ^a

Catalyst	Brønsted acid density (mmol g ⁻¹)	Surface area (m ² g ⁻¹)	Yield (%)	Selectivity (%)
TiNT	0.21	400	9.8	18.4
Nb(5%)-TiNT	0.22	431	74.7	75.0
TiO ₂	-	300	0	0
Niobic acid	0.4	128	0	0
H-mordenite ^b	1.5	360	14.5	29.6
H-ZMS-5	0.2	326	2.7	15.6
Amberlyst 15	4.9	50	22.9	22.9
Nafion NR50	0.9	1	73.7	73.7
Nafion SAC13	0.13	344	85.7	85.7

^aReaction conditions: Reaction conditions: catalyst (0.2 g), toluene (0.1 mol), benzyl alcohol (0.01 mol), reaction temperature 373 K, reaction time 5h. ^bJRC-Z-HM20, ^cJRC-Z5-90H

6.3.3 Acid properties

The acid properties of the Nb-TiNTs were evaluated by probing the vibrational spectra of adsorbed pyridine using FT-IR spectroscopy. The difference FT-IR spectra of pyridine-adsorbed Nb(5%)-TiNT (298 K) are shown in Fig. 4.12. The band at *ca.* 1450 cm⁻¹ was clearly observed at low pyridine coverage (1.7 Pa), but OH band around 3700 cm⁻¹ was not changed, which indicates that the band is attributed not to hydrogen-bonding pyridine to non-acidic OH groups but to pyridine coordinatively bound to Lewis acid sites [28]. As increasing in pyridine coverage, broad negative OH band and the band at 1545 cm⁻¹ due to pyridinium ions formed on Brønsted acid sites increased. Thus, Nb-TiNT catalyst has both Lewis and Brønsted acid sites on the surface, which is very similar to the result of non-doped TiNT [8]. The amounts of acid sites of Nb-TiNTs were determined by FT-IR measurements for pyridine adsorbed samples and titration method with NaCl aqueous solution according to the previous method [9]. As shown in Table 4.5, there is no noticeable difference in the concentration of both Lewis and Brønsted acid sites among Nb-TiNTs. The amount of Lewis and

Brønsted acid sites on Nb-TiNT catalyst is comparable to that of non-doped TiNT.

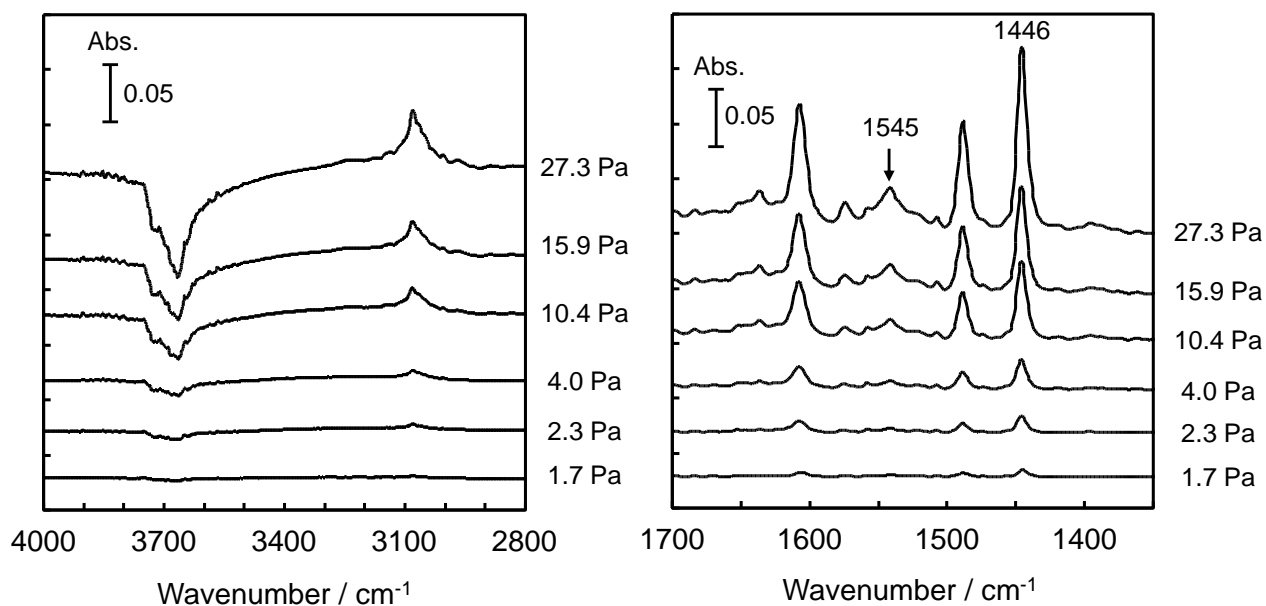


Figure 4.12. Difference FT-IR spectra for pyridine adsorbed Nb(5%)-TiNT at 298 K.

Table 4.5. Acid amount of Nb-TiNT estimated by FT-IR measurements with pyridine as a prove molecule.

Catalyst	Acid amount (mmol g ⁻¹)	
	Brønsted	Lewis
TiNT	0.21	0.27
Nb(1%)-TiNT	0.21	0.21
Nb(5%)-TiNT	0.22	0.23
Nb(10%)-TiNT	0.22	0.27

Next, the acid strength of samples was evaluated using ³¹P MAS NMR measurements with TMPO as a basic probe molecule. As the ³¹P chemical shifts of protonated TMPO tend to move downfield, higher chemical shifts mean higher protonic acid strength [29,30]. Figure 4.13 shows ³¹P MAS NMR spectra

for TMPO adsorbed on Nb-TiNT with various Nb content. All samples exhibit a broad ^{31}P peak in the range of 50–80 ppm. No excess solid TMPO was observed (*ca.* 40 ppm). The observed peaks can be assigned to H^+ -complexed (Brønsted-bound) TMPO species, because the ^{31}P MAS NMR chemical shift range for the TMPO/Brønsted complex is determined to fall within the range of 50–75 ppm according to the previous literatures [31,32]. These spectra reveal similar feature, and can be deconvoluted by 4 components. Table 4.6 summarizes the deconvolution results and relative area ratios for different sites. The intensity of the large downfield peaks at 65 and 70 ppm slightly increased with increasing Nb content, implying that the amount of strong Brønsted acid sites is increased by Nb doping. However, the amount of strong Brønsted acid sites on Nb(5%)-TiNT is only 1.2 times higher than that of non-doped TiNT because total amounts of Brønsted acid sites for are almost equivalent for both samples. The enhanced catalytic activity of Nb-TiNT therefore cannot be explained unambiguously by the Brønsted acidity.

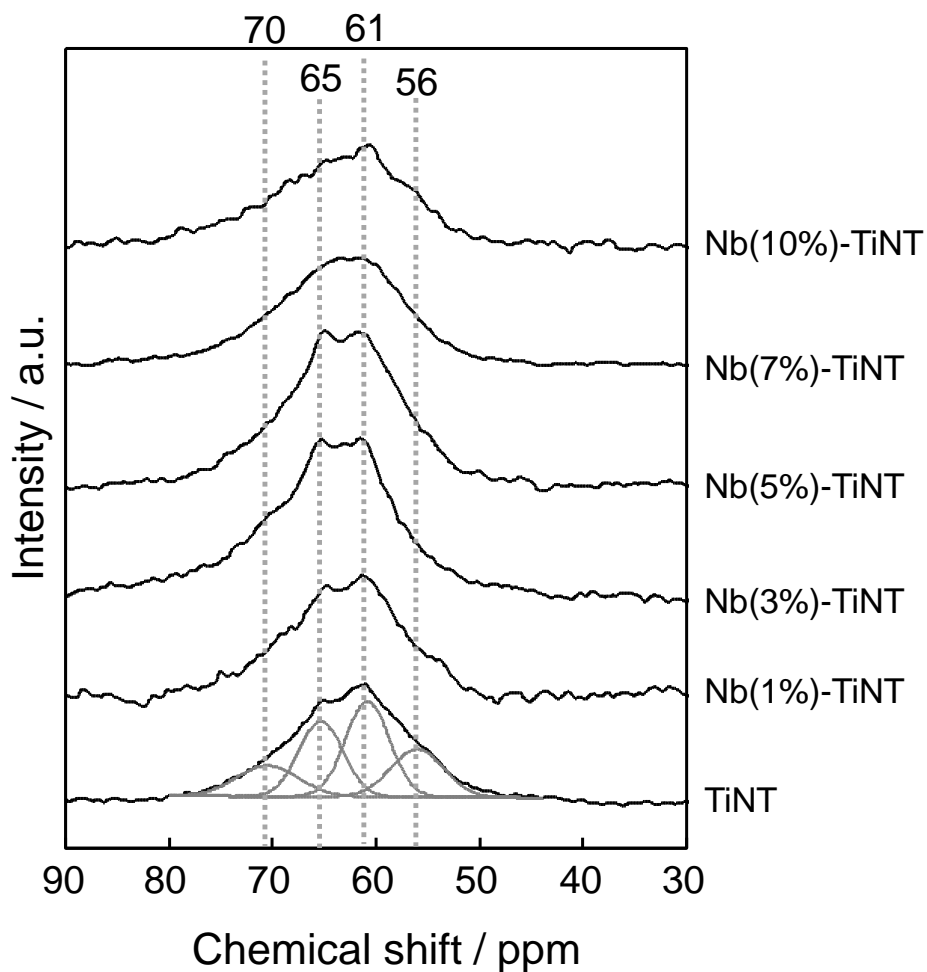


Figure 4.13. ^{31}P MAS NMR spectra for TMPO adsorbed on TiNT and Nb-TiNTs.

Table 4.6. Relative ratio for various Brønsted acid sites observed in Fig. 4.13.

Catalyst	Relative ratio (%)			
	70 ppm	65 ppm	61 ppm	56 ppm
Nb(10%)-TiNT	20.2	30.3	31.5	18.0
Nb(7%)-TiNT	21.6	29.5	32.8	16.1
Nb(5%)-TiNT	20.5	31.4	31.4	16.8
Nb(3%)-TiNT	19.4	31.1	38.1	11.4
Nb(1%)-TiNT	18.9	28.4	33.8	18.9
TiNT	15.8	27.7	35.2	21.2

The results of Friedel-Crafts alkylation of toluene with benzyl alcohol over TiNT and Nb(5%)-TiNT under various benzyl alcohol concentrations are shown in Figure 4.13. The catalytic activity of Nb(5%)-TiNT increased with the benzyl alcohol concentration, whereas that of TiNT was almost constant regardless of the benzyl alcohol concentration. The reaction orders for Nb(5%)-TiNT and TiNT with benzyl alcohol were determined to be 1.10 and -0.17, respectively, which strongly indicates that the surface coverage of benzyl alcohol on Nb(5%)-TiNT is much lower than that on TiNT.

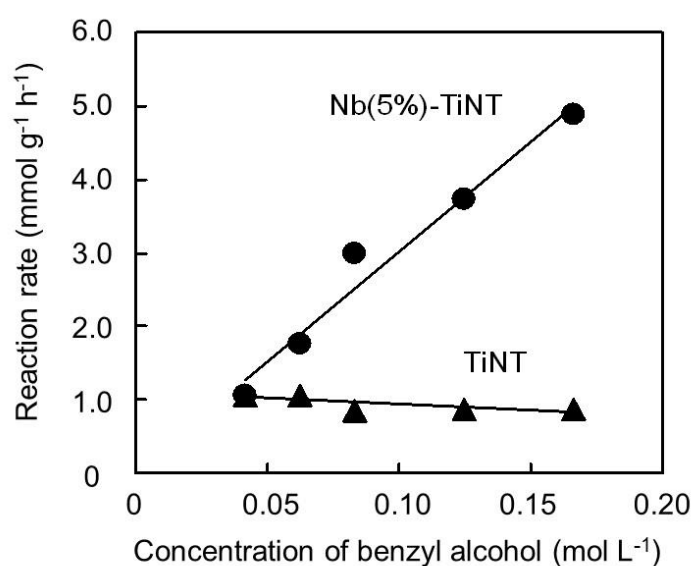


Figure 4.14. Reaction rates over TiNT and Nb(5%)-TiNT as a function of the concentration of benzyl alcohol. Reaction conditions: catalyst (0.2 g), reaction temperature 373 K

The first-order kinetics for alkylation with respect to the benzyl alcohol concentration suggest that benzyl alcohol adsorption would be the rate-determining step over Nb(5%)-TiNT. On the other hand, benzyl alcohol is strongly adsorbed on the TiNT surface, so that the rate-determining step is the formation of the benzyl cation. In the case of non-doped TiNT, the diffusion of the benzyl alcohol takes place not only the outer surface of the nanotubes but also inside the nanotubes due to the capillarity effect. The preferential adsorption of benzyl alcohol onto TiNT may retard the diffusion of toluene on

the catalyst surface, especially inside the nanotubes, resulting in low catalytic activity at high concentration of benzyl alcohol (Fig. 4.14). Both benzyl alcohol and toluene molecules can access easily to the surface acid sites on Nb-TiNT because it has distorted nanotube structure as shown Fig. 4.4. In addition, the amount of strong Brønsted acid sites on Nb(5%)-TiNT is higher than that of non-doped TiNT (Fig. 4.13), which promotes the formation of benzyl cations. These two factors enhance the alkylation reaction over Nb(5%)-TiNT.

6.4. Conclusions

Nb-doped titanate nanotubes with a distorted structure were prepared by the hydrothermal treatment of Nb-doped TiO₂. It was demonstrated that the acid catalytic properties of TiNT are substantially enhanced by Nb-doping. Nb-doped TiNTs shows much higher catalytic activity for Friedel-Crafts alkylation of toluene with benzyl chloride or benzyl alcohol than non-doped TiNT and other Nb-containing solid acid catalysts and comparable to sulfonated resin catalysts. The amounts of Lewis and Brønsted acid sites of the TiNT remained unchanged after Nb-doping, although the Brønsted acid strength was increased with the Nb content up to 5%. Based on the structural analyses and catalytic performance, it can be concluded that Nb-doping causes an increase of Brønsted acidity of TiNT and a distortion of nanotube structure, which enhanced the alkylation reactions.

References

- [1] Corma, A. *Chem. Rev.*, **1995**, 95, 559–614.
- [2] Okuhara, T. *Chem. Rev.*, **2002**, 102, 3641–3665.
- [3] Haruta, M.; Tsubota, S.; Kobayashi, T.; Kageyama, H.; Genet, M. J.; Delmon, B. *J. Catal.*, **1993**, 144, 175–192.
- [4] Fujishima, A.; Honda, K. *Nature*, **1972**, 238, 37.
- [5] Oregan, B.; Gratzel, M. *Nature*, **1991**, 353, 737–740.
- [6] Tanabe, K.; Hattori, H.; Sumiyoshi, T.; Tamaru, K.; Kondo, T. *J. Catal.*, **1978**, 53, 1–8.

- [7] Kitano, M.; Nakajima, K.; Kondo, J.N.; Hayashi, S.; Hara, M. *J. Am. Chem. Soc.*, **2010**, 132, 6622–6623.
- [8] Kitano, M.; Wada, E.; Nakajima, K.; Hayashi, S.; Miyazaki, S.; Kobayashi, H.; Hara, M. *Chem. Mat.*, **2013**, 25, 385–393.
- [9] Wada, E.; Kitano, M.; Nakajima, K.; Hara, M. *J. Mater. Chem. A*, **2013**, 1, 12768–12774.
- [10] Tanabe, K.; Okazaki, S. *Appl. Catal. A*, **1995**, 133, 191–218.
- [11] Iizuka, T.; Ogasawara, K.; Tanabe, K. *Chem. Soc. Jpn.*, **1983**, 56, 2927–2931.
- [12] Nakajima, K.; Baba, Y.; Noma, R.; Kitano, M.; Kondo, J.N.; Hayashi, S.; Hara, M. *J. Am. Chem. Soc.*, **2011**, 133, 4224–4227.
- [13] Takagaki, A.; Yoshida, T.; Lu, D.L.; Kondo, J.N.; Hara, M.; Domen, K.; Hayashi, S. *J. Phys. Chem. B*, **2004**, 108, 11549–11555.
- [14] Shishido, T.; Kitano, T.; Teramura, K.; Tanaka, T. *Catal. Lett.*, **2009**, 129, 383–386.
- [15] Kitano, T.; Shishido, T.; Teramura, K.; Tanaka, T. *J. Phys. Chem. C*, **2012**, 116, 11615–11625.
- [16] Murayama, T.; Chen, J.L.; Hirata, J.; Matsumoto, K.; Ueda, W. *Catal. Sci. Technol.*, **2014**, 4, 4250–4257.
- [17] Takagaki, A.; Tagusagawa, C.; Hayashi, S.; Hara, M.; Domen, K. *Energy Environ. Sci.*, **2010**, 3, 82–93.
- [18] Traversa, E.; Di Vona, M.L.; Licocchia, S.; Sacerdoti, M.; Carotta, M.C.; Crema, L.; Martinelli, G. *J. Sol–Gel Sci. Techn.*, **2001**, 22, 167–179.
- [19] Nikolic, L. M.; Milanovic, M.; Nedic, S.; Giannakopoulos, K.; Kontos, A. G. *Ceram. Int.*, **2011**, 37, 111–117.
- [20] Liu, C.; Miao, L.; Zhou, J. H.; Huang, R.; Tanemura, S. *J. Mater. Chem.*, **2012**, 22, 14180–14190.
- [21] Corma, A.; Garcia, H. *Chem. Rev.*, **2003**, 103, 4307–4365.
- [22] Fan, W. Q.; Zhang, Q.H.; Deng, W. P.; Wang, Y. *Chem. Mat.*, **2013**, 25, 3277–3287.
- [23] Ballantine, J. A.; Davies, M.; Purnell, H.; Payanakorn, M.; Thomas J. M.; Williams, K. J. *J. Chem. Soc., Chem. Commun.*, **1981**, 427–428.
- [24] Morais, M.; Torres, E. F.; Carmo, L. M. P. M.; Pastura, N. M. R.; Gonzalez, W.A.; dos Santos, A. C. B.; Lachter, E. R. *Catal. Today*, **1996**, 28, 17–21.
- [25] Rao, Y.; Trudeau, M.; Antonelli, D. *J. Am. Chem. Soc.*, **2006**, 128, 13996–13997.
- [26] Ganesan K.; Pillai, C. N. *J. Catal.*, **1989**, 119, 8–13.
- [27] Jin, H.; Ansari, M. B.; Jeong, E.Y.; Park, S. E. *J. Catal.*, **2012**, 291, 55–62.
- [28] Kondo, J. N.; Nishitani, R.; Yoda, E.; Yokoi, T.; Tatsumi, T.; Domen, K. *Phys. Chem. Chem. Phys.*, **2010**, 12, 11576–11586.
- [29] Rakiewicz, E.F.; Peters, A.W.; Wormsbecher, F.; Sutovich, K. J.; Mueller, K. T. *J. Phys. Chem. B*, **1998**, 102, 2890–2896.
- [30] Zheng, A.M.; Huang, S.J.; Liu, S.B.; Deng, F. *Phys. Chem. Chem. Phys.*, **2011**, 13, 14889–14901.
- [31] Kao, H.M.; Yu, C.Y.; Yeh, M.C. *Microporous Mesoporous Mat.*, **2002**, 53, 1–12.

[32] Zhao, Q.; Chen, W.H.; Huang, S.J.; Wu, Y.C.; Lee, H.K.; Liu, S.B. *J. Phys. Chem. B*, **2002**, 106, 4462–4469.

Chapter 5

Direct Cyanomethylation of Aliphatic and Aromatic Hydrocarbons with Acetonitrile over Metal Loaded Titanium Oxide Photocatalyst

Abstract

Platinum-loaded TiO₂ (Pt/TiO₂) photocatalysts promoted cyanomethylation of aliphatic hydrocarbons, namely cyclohexane and cyclohexene, with acetonitrile. In these reactions, it is suggested that the photogenerated holes oxidatively dissociate the C–H bond of both the acetonitrile and the aliphatic hydrocarbons to form each radical species before the radical cross-coupling of them. The Pt/TiO₂ photocatalyst was more active than the Pd/TiO₂ photocatalyst for these reactions in the current condition. In contrast, although the cyanomethylation of benzene is known to be promoted by the Pd/TiO₂ photocatalyst through the reaction between benzene and the generated cyanomethyl radical, it was found that a physical mixture of the Pt/TiO₂ photocatalyst and a Pd catalyst supported by Al₂O₃ also promoted this reaction and it was hardly promoted by the Pt/TiO₂ photocatalyst alone. The temperature dependence of the reaction rate proved that the Pd nanoparticles on the TiO₂ photocatalyst functioned as a metal catalyst for the dark process in this photocatalytic reaction. These results clearly suggested that the Pd metal catalyst is necessary for the cyanomethylation of benzene. However, in the cyanomethylation of aliphatic hydrocarbons, the improvement of the reaction rate by the metal particles was not observed, meaning that the radical cross-coupling would take place without the metal catalysis. Thus, it is concluded that in the case of the benzene cyanomethylation the Pd nanoparticles can play the dual roles, as the catalyst to activate benzene ring to enhance the substitution reaction with the cyanomethyl radical, and as the electron receiver to reduce the recombination of the photoexcited electron and hole in the TiO₂ photocatalyst, although the cyanomethylation of aliphatic hydrocarbons can proceed without the assist of the catalysis in the dark process by the Pd nanoparticles.

5.1. Introduction

Cyanomethylation is one of useful synthesis methods to provide intermediates of medicines, polymers, and so on. In order to obtain cyanomethylated compounds with high yield, functionalized nitriles such as trimethylsilyl acetonitrile [1], cyanoacetate salts [2] and chloroacetonitrile [3] are

typical reagents, and it is recognised that acetonitrile is not useful as a nitrile source as it is due to its very weak acidity [4]. Thus, the direct cyanomethylation with acetonitrile has been examined by using some kinds of base reagents such as NaH [5], cesium pivalate [6] and NaOH [7] to induce the dissociation of the C–H bond of acetonitrile. However, available strong base reactants are limited because they tend to promote side reactions also.

On the other hand, radical initiators [8] and metal complex catalysts [4,9] have been developed for the direct activation of the C–H bond of acetonitrile. For example, J. Li *et al.* reported that di-*tert*-butyl peroxide (DTBP) can activate acetonitrile to form cyanomethyl radical for cyanomethylation of aliphatic amides [8c]. Chakraborty *et al.* succeeded in the cyanomethylation of aldehydes at room temperature with a Ni complex catalyst promoting the C–H cleavage of acetonitrile [4]. In view of the sustainable chemistry, catalytic process is more desirable. However, in homogeneous catalytic reaction systems, it has always been pointed out that the products separation from the reaction mixture is not easy. Thus, heterogeneous catalysts have been desired for the direct cyanomethylation with acetonitrile, but it still has not been achieved except for the photocatalytic cyanomethylation [10].

Since TiO₂ photocatalyst oxidized organic compounds to radical species under the light irradiation, direct functionalizations of aromatics have been investigated by using metal loaded TiO₂ photocatalysts (M/TiO₂, M: Pt or Pd) [11]. For example, Pt/TiO₂ photocatalysts promoted functionalization of benzene with water [12] and ammonia [13] to yield phenol and aniline, respectively. The direct cyanomethylation of various aromatic compounds with acetonitrile was successfully achieved by employing Pd/TiO₂ photocatalysts to yield benzyl cyanides [10]. The Pd/TiO₂ photocatalysts also forwarded reactions between benzene and various ethers to form phenylated ethers [14]. Usually, Pt nanoparticles on a semiconductor photocatalyst much improve the photocatalytic activity compared to other metals such as Pd. It is explained that Pt nanoparticles function as a charge separator for the photoexcited electron and hole because of the large work function of Pt [15]. However,

it is noted that the direct cyanomethylation of benzene with acetonitrile hardly proceeded over the Pt/TiO₂ photocatalyst, while it was well promoted over the Pd/TiO₂ photocatalyst only under photoirradiation. This shows that the Pd nanoparticles on the TiO₂ photocatalyst themselves concertedly functioned in addition to the well-known photocatalysis by the TiO₂ photocatalyst, suggesting that the Pd nanoparticles would contribute as a metal catalyst to this reaction in the presence of photocatalyst [10]. In literature, some articles have described the function of the metal particles as a catalyst coupled with the photocatalysis [10,14,16].

In the present chapter, the photocatalytic cyanomethylation reactions of cyclohexane and cyclohexene were examined by using the M/TiO₂ photocatalysts and their reaction mechanisms were discussed. In addition, in order to clarify the function of the metal nanoparticles on TiO₂ photocatalyst, the physical mixture of the TiO₂ photocatalyst and a supported Pd or Pt metal catalyst was applied for the cyanomethylations of cyclohexane, cyclohexene, and benzene.

5.2. Experimental

5.2.1 Preparation of metal loaded TiO₂

Anatase TiO₂ (JPC-TIO-8, 338 m² g⁻¹) supplied by Catalysis Society of Japan was used as the photocatalyst. Metal nanoparticles were loaded by a photodeposition method as below. TiO₂ powder was suspended in an aqueous solution in a beaker and irradiated by the light from a 300 W xenon lamp (PE300BUV) without any optical filters (the intensity was 50 mW cm⁻² measured at 360±15 nm) to clean the catalyst surface for 60 min. After the pre-irradiation, a stock solution of a metal precursor (PdCl₂, Wako 99.0 %, dissolved in an aqueous solution of HCl, or H₂PtCl₆, Wako 99.8 %, dissolved in water) and 20 vol% of methanol as a hole scavenger were added into the suspension, and then it was stirred for 15 min in the dark, followed by photoirradiation from the xenon lamp without optical filters for 60 min. The obtained sample was separated from the suspension by suction filtration and washed with ion exchanged water. The prepared sample was dried at 323 K overnight in an oven to obtain the

metal loaded photocatalyst, *i.e.*, the M/TiO₂ samples. The metal loading amount of Pd or Pt was 0.1 wt%.

An impregnation method was employed for the preparation of the metal loaded Al₂O₃ samples. The Al₂O₃ spherical granule donated by Catalysis Society of Japan (JRC-ALO-07, 204 m² g⁻¹) was milled with a mortar before use. The Al₂O₃ powder, ion exchanged water, and an aqueous solution of the metal precursor mentioned above were put into a beaker, followed by stirring for 60 min at room temperature. The mixture was heated for evaporation to dryness around 373 K with stirring, and the obtained powder was calcined at 723 K for 60 min. The obtained power samples were referred to as the M(x)/Al₂O₃ samples, where the metal loading amount (x) on the Al₂O₃ support was 0.1, 1.0 or 2.0 wt%.

5.2.2 Photocatalytic reaction tests

The photocatalytic reaction tests were performed in a closed quartz reactor (46 cm³) under an argon atmosphere. The M/TiO₂ sample (0.2 g) was put into the quartz reactor and pre-irradiated from the beneath (20 cm²) with the xenon lamp for 15 min in air to clean the catalyst surface. After purging with argon, a mixture (4.0 mL) consisting of 0.1 mL of benzene, cyclohexane or cyclohexene, 3.8 mL of acetonitrile and 0.1 mL of ion exchanged water were introduced into the reactor. All reactants for the reaction tests were of analytical grade and used without further purification. The reaction test was carried out under the light of 365±20 nm in wavelength from the xenon lamp for 60 min with cooling by an electric fan. The light intensity was measured at 360±15 nm to be 27 mW cm⁻². After the reaction, the products in the gas phase were collected by a gas tight syringe and then analysed by a GC-TCD (Shimadzu, GC-8A). The reaction mixture was diluted with methanol and filtrated with a PTFE filter. The filtrate was mixed with a methanol solution of n-decane as an internal standard, and then analysed by a GC-MS (Shimadzu, GCMS-QP5050A).

5.2.3 Electron spin resonance (ESR) measurement

In order to investigate the radical species formed during the cyanomethylation of cyclohexane and cyclohexene, ESR spectra were recorded by an X-band spectrometer (JEOL-RE2X) in the presence of the Pd/TiO₂ photocatalyst under photoirradiation. Before the measurement, the Pd/TiO₂ sample was pre-irradiated for 60 min in order to clean the surface. The trace amount of the pre-irradiated Pd/TiO₂ sample (0.02 g) was suspended in cyclohexane (1 mL, 9.26 mmol) with PBN (N-tert-Butyl- α -phenylnitrone, Tokyo Chemical Industry, 98%, 0.67 mmol) as a spin trap reagent, then a part of the solution was taken into a quartz sample cell. In order to suppress the photodissociation of the cyclohexane and cyclohexene, the light from a xenon lamp was limited to 400 \pm 20 nm in wavelength with a band-pass filter. Especially, for measuring the ESR spectra of the cyclohexene solution, oxygen was carefully removed from the mixed solution of cyclohexene and PBN, and then a part of the solution was transferred into a quartz sample cell. After that, a trace amount of the Pd/TiO₂ sample was added into the solution, followed by argon purge. Other procedure and condition were the same as mentioned above.

5.3. Results and discussion

5.3.1 Cyanomethylation of cyclohexane

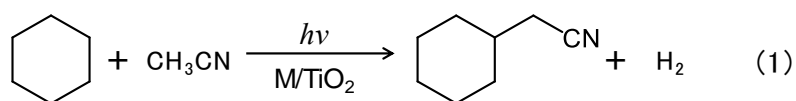
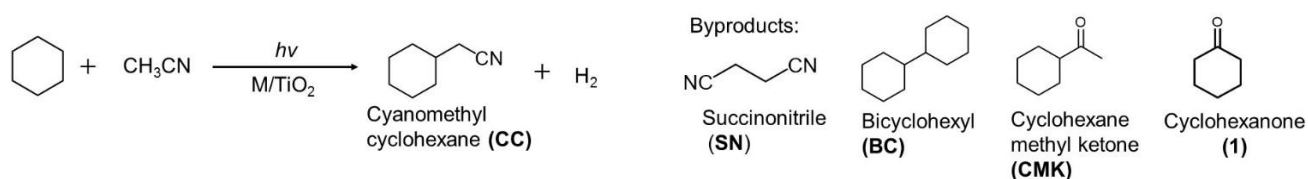


Table 5.1 shows the result of the reaction between cyclohexane and acetonitrile (eq. 1) over the photocatalyst samples. The Pt/TiO₂ sample gave cyanomethyl cyclohexane (CC) as the desired product, which was lower than that of succinonitrile (SN) as a major by-product (Table 5.1, entry 1). A small amount of bicyclohexyl (BC), cyclohexyl methyl ketone (CMK) and cyclohexanone were also detected. Hydrogen was detected as a gaseous product although the determination accuracy was not so high. The reaction over the Pd/TiO₂ sample gave the same products (Table 5.1, entry 2), but the

yields of these products were much less than those over the Pt/TiO₂ sample, implying that the Pt loaded on TiO₂ enhanced the charge separation of excited electrons and holes more efficiently and thus gave more products [14]. In both cases, the selectivity for CC was not high compared with the cyanomethylation of benzene [10]. The pristine TiO₂ photocatalyst exhibited much less activity than metal loaded ones (Table 5.1, entry 3), showing that these metal nanoparticles acted as a cocatalyst enhancing the electron-hole separation.

The effect of the addition of the M/Al₂O₃ sample to the Pt/TiO₂ photocatalyst was also examined in this reaction system for the discussion mentioned later to know the catalytic effect of the loaded metals. According to the literature [17], the presence of platinum black with TiO₂ photocatalyst much improved the photocatalytic activity because physical contact of Pt species with TiO₂ photocatalyst enhances the charge separation of the photogenerated electron-hole pairs in the TiO₂ photocatalyst. To investigate the other function of the metal nanoparticles such as catalysis, the physical contact of metal nanoparticles and TiO₂ photocatalyst should be avoided. Thus, the M/Al₂O₃ samples were employed here. Since in these samples the metal nanoparticles were dispersed and stabilised on the surface of the alumina with large specific surface area, the nanoparticles could not contact with the TiO₂ surface, allowing us to ignore the effect of the metal nanoparticle as the electron scavenger. As listed in Table 5.1 entries 4–6, the yield of CC decreased in the coexistence of the Pd/Al₂O₃ sample, the Pt/Al₂O₃ sample, and the bare Al₂O₃ sample. These results indicated that the contribution of the catalysis by the supported Pd and Pt metal particles was not so large or negligible in this reaction system.

Table 5.1. Results of the photocatalytic reaction tests for the cyanomethylation of cyclohexane with acetonitrile over the M/TiO₂ photocatalyst, a mixture of the M/TiO₂ sample and the M/Al₂O₃ sample, or a mixture of the Pt/TiO₂ sample and the Al₂O₃ sample. ^a



Entry	Catalyst ^b	Products / μ mol					H ₂
		CC	SN	BC	CMK	1	
1	Pt/TiO ₂	10	16	2.0	1.5	1.1	70
2	Pd/TiO ₂	2.6	2.5	0.13	0.36	0.4	15
3	TiO ₂	tr. ^d	tr.	tr.	0.27	tr.	tr.
4	Pt/TiO ₂ + Pd(1.0)/Al ₂ O ₃ ^d	4.2	4.0	0.58	0.87	tr.	28
5	Pt/TiO ₂ + Pt(1.0)/Al ₂ O ₃ ^d	4.3	4.8	0.72	0.25	tr.	28
6	Pt/TiO ₂ + Al ₂ O ₃ ^d	4.0	7.5	1.7	0.56	tr.	34

^a Reaction conditions: the M(0.1wt%)/TiO₂ photocatalyst 0.2 g, cyclohexane 0.93 mmol (0.1 mL), acetonitrile 72.8 mmol (3.8 mL), and water 5.56 mmol (0.1 mL). Reaction time was 1 h. The wavelength of the irradiation light was 365 \pm 20 nm and the light intensity was 27 mW cm⁻² measured at 360 \pm 15 nm. ^b The loading amount of metal on the TiO₂ sample was 0.1 wt%, and the loading amount of metals on the Al₂O₃ support was 1.0 wt%. ^c not detected. ^d trace. ^e A mixture of the M(0.1wt%)/TiO₂ photocatalyst of 0.2 g and the M(1.0 wt%)/Al₂O₃ sample or the bare Al₂O₃ sample of 0.2 g was used.

Since SN and BC were given by each photocatalyst, both acetonitrile and cyclohexane molecules should be oxidized by the TiO₂ photocatalysts to form each radical species, followed by the radical homo-coupling reaction between them. As shown in the literature [10], acetonitrile can be oxidized to a cyanomethyl radical species by a Pd/TiO₂ photocatalyst under the light. In this study, ESR measurement was carried out in order to confirm the formation of radical species from cyclohexane in the presence of the photocatalyst. Fig. 5.1 shows the ESR spectra of cyclohexane solution containing PBN as a spin trap reagent in some conditions. While no signals except for those of Mn²⁺ marker was observed without the photocatalyst (Fig. 5.1(a)) or light (Fig. 5.1(b)), new triplet signals were detected in the presence of the Pd/TiO₂ photocatalyst upon light irradiation (Fig. 5.1(c)).

Although the hyperfine structure was not clearly observed due to the weak signals, which would imply the high C–H bond activation energy of cyclohexane, these signals would be a radical species generated by the photocatalyst. Judging from the compounds in the cell under this condition, it can be considered that the triplet signals could originate from the nitrogen of the PBN adduct shown in Fig. 1 with the g value = 2.0065 and $A^N = 1.33$ mT [18], indicating that the cyclohexene-PBN adduct would be detected. Signals assignable to the hydrogen radical adduct could not be observed in this condition.

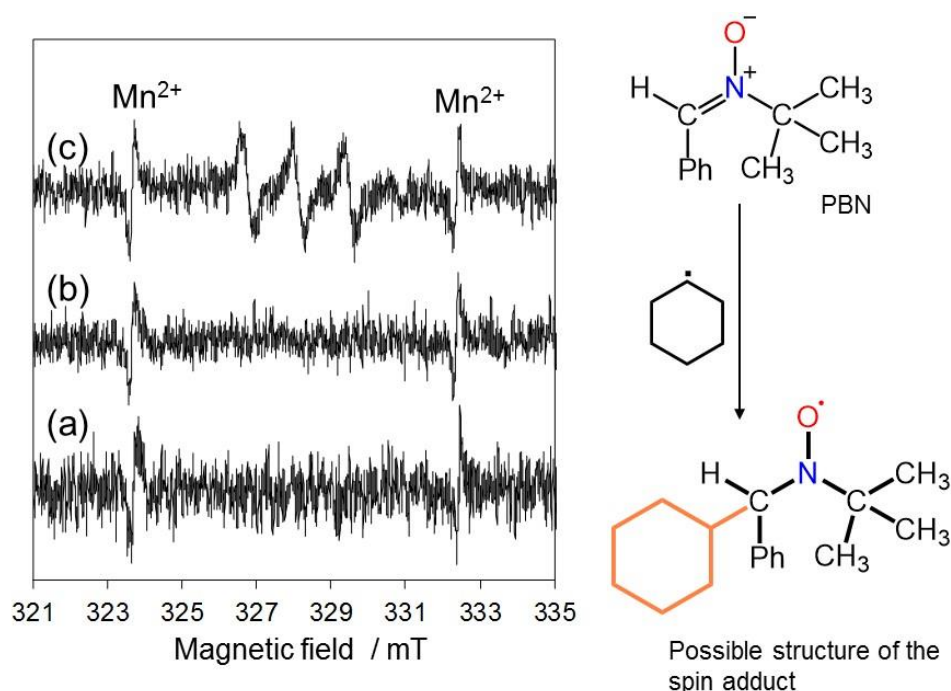


Figure 5.1. ESR spectra of cyclohexane using PBN as a spin trap reagent measured (a) after light irradiation for 120 min without the Pd/TiO₂ sample, (b) in the presence of the Pd/TiO₂ sample in the dark, and (c) after light irradiated for 120 min in the presence of the Pd/TiO₂ sample.

To know the rate-determining step in this reaction condition, some reaction tests were carried out with deuterated reagents over the M/TiO₂ samples. As listed in Table 5.2, when deuterated acetonitrile (CD₃CN) was reacted with cyclohexane (C₆H₁₂) over the Pt/TiO₂ sample, the yield of CC was almost similar to or slightly larger than the result using normal reagents, i.e. the k_H/k_D value for the CC formation was not larger than unity (Table 5.2, entry 2). On the other hand, when deuterated

cyclohexane (C_6D_{12}) was used for the reaction, the yield of CC clearly decreased, i.e., the k_H/k_D value for the CC formation was almost 2.0. This kinetic isotopic effect (KIE) clearly evidenced that the C–H bond activation of cyclohexane would be the rate-determining step (RDS) to give CC in this condition (Table 5.2, entry 3). The similar KIE was observed for the reaction over the Pd/TiO₂ sample (Table 5.2, entries 4–6), showing that the RDS would be the same step as the case of the Pt/TiO₂ sample. These results are consistent with the order of the C–H bond dissociation energy [19a] (Table 5.3): cyclohexane (416 KJ mol⁻¹) > acetonitrile (406 KJ mol⁻¹), where the RDS corresponded to the cleavage of the stronger bond.

Table 5.2. Results of the reaction tests with isotopic compounds for the direct cyanomethylation of cyclohexane by the M(0.1 wt%)/TiO₂ photocatalyst ^a


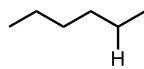
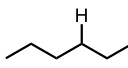
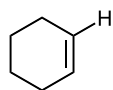
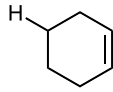
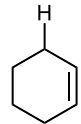
Entry	Loaded		Products ^b / μ mol			k_H/k_D ^c		
	metal on TiO ₂	Isotopic compound	CC	SN	BC	CC	SN	BC
1		none	10	16	2.0	-	-	-
2	Pt	CD ₃ CN	12	3.0	19	0.83	5.3	0.11
3		C ₆ D ₁₂	5.2	19	0.90	1.9	0.84	2.2
4		none	2.0	2.5	0.29	-	-	-
5	Pd	CD ₃ CN	2.6	n.d. ^d	2.1	0.77	-	0.14
6		C ₆ D ₁₂	1.7	2.6	0.11	1.2	0.96	2.6

^a The M/TiO₂ sample 0.2 g, cyclohexane 0.93 mmol (0.1 mL), acetonitrile 72.8 mmol (3.8 mL), and water 5.6 mmol (0.1 mL). Reaction time was 1 h. The wavelength of the irradiation light was 365±20 nm and the light intensity was 27 mW cm⁻² measured at 360±15 nm. ^b CC= cyanomethyl cyclohexane, SN= succinonitrile, BC= bicyclohexyl. ^c $k_H/k_D(\text{CC}) = (\text{yield of CC with the normal reagent}) / (\text{yield of CC with the deuterated reagent})$. The values of $k_H/k_D(\text{SN})$ and $k_H/k_D(\text{BC})$ were calculated in the similar ways. ^d Not detected.

On the other hand, it should be considered that the k_H/k_D values less than unity (inverse KIE) can provide more important information of the reaction mechanism. When the reaction between cyclohexane and CD₃CN was carried out, the k_H/k_D values for the yields of CC and BC were 0.83 and 0.11, respectively over the Pt/TiO₂ sample (Table 5.2, entry 2) and 0.77 and 0.14, respectively over

the Pd/TiO₂ sample (Table 5.2, entry 5), which can be recognised as the inverse KIE. In this reaction, both cyclohexane and acetonitrile would be oxidized by the photocatalytically-generated hole to become corresponding radical species, *i.e.*, the two reactions competitively take place to consume the photogenerated holes. The use of CD₃CN with C₆H₁₂ would decrease the oxidation rate of acetonitrile due to the high C–D bond dissociation energy, which enhanced the oxidation of competitor instead, *i.e.*, formation of the cyclohexyl radical. Since the RDS in these coupling reactions was the formation of cyclohexyl radical, both formation rates of CC and BC increased in the presence of CD₃CN as a result. In the reaction between CH₃CN and C₆D₁₂, since the C–D bond dissociation of C₆D₁₂ was more difficult, the competitive oxidation was enhanced, resulting that the concentration of cyanomethyl radical increased. In consequence, the yield of SN increased and the k_H/k_D values for SN production were lower than unity such as 0.84 and 0.96 (Table 5.2, entries 3 and 6). These results clarified that the competitive hole oxidation of both cyclohexane and acetonitrile took place to form their radical species.

Table 5.3. The C–H bond dissociation energies of organic compounds employed for the direct cyanomethylation. ^a

Compounds	C–H bonds	Bond dissociation energy /kJ mol ⁻¹
acetonitrile	H–CH ₂ CN	406
cyclohexane	H–C ₆ H ₁₁	416
n-hexane		414
		410
		415
cyclohexene ^b		457
		415
		350
benzene	H–C ₆ H ₅	440

^a These values were cited from the handbook of bond dissociation energy. [19a] ^b These values were cited from the literature. [19b]

Considering the results of the ESR measurements and the kinetic isotopic effect, the reaction mechanism for the cyanomethylation of cyclohexane should be radical cross-coupling, which would be a two photon process, as shown in Fig. 5.2. First, photoexcited electrons and holes generate on TiO₂ photocatalyst under photoirradiation. The holes on the TiO₂ surface oxidize both reactants, cyclohexane and acetonitrile, to form the corresponding radical species and protons, which proceeds competitively. Then, CC would be produced through the cross-coupling reaction between the cyclohexyl radical and the cyanomethyl radical, while BC and SN would be also formed via each homo-coupling reaction similarly. Produced protons were reduced by the photoexcited electrons to hydrogen radicals, followed by their radical coupling to form molecular hydrogen. These reactions can be promoted by the Pt or Pd loaded TiO₂, although the former exhibited higher activity. In the

cyanomethylation of cyclohexane proceeding via radical coupling, the loaded metal would function as the electron receiver to reduce the recombination of the photoexcited electron and hole in the TiO₂ photocatalyst.

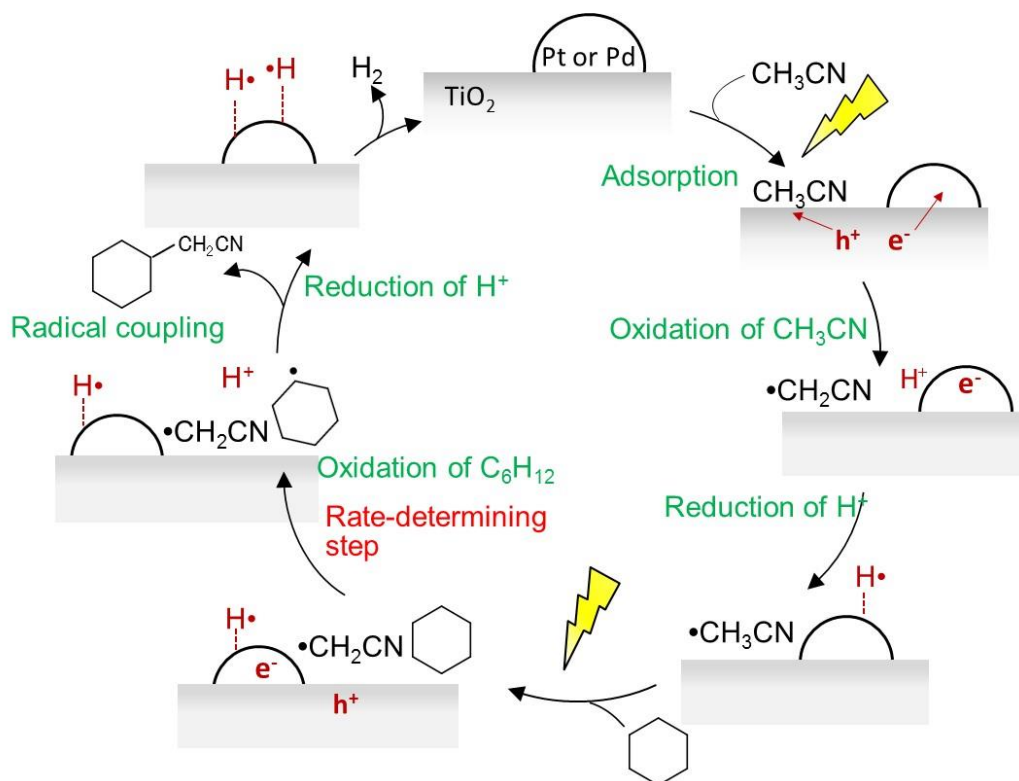
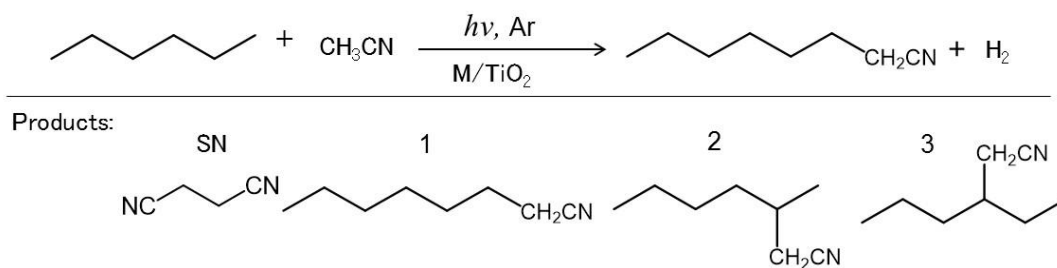


Figure 5.2. Proposed reaction mechanism of the direct cyanomethylation between cyclohexane and acetonitrile over the M/TiO₂ photocatalyst.

The cyanomethylation of n-hexane with acetonitrile was also examined with the Pd/TiO₂ and Pt/TiO₂ samples (Table 5.4). The cyanomethylated products were obtained in the presence of these photocatalysts, and the Pt/TiO₂ sample gave the products in higher yield than the Pd/TiO₂ sample. Among cyanomethylated products, the compound 2 and 3 were obtained more than the compound 1. The cyanomethylation at the primary carbon less proceeded because the primary carbon radical species would be rather unstable compared to the secondary and tertiary carbon radical species. However, the product selectivity was not so clear because of the small difference in the C–H bond dissociation

energy as shown in Table 5.3.

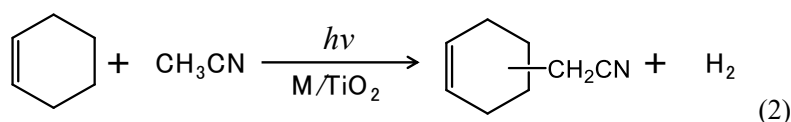
Table 5.4. Results of the photocatalytic reaction tests for the cyanomethylation of n-hexane with acetonitrile over a M/TiO₂ photocatalyst.^a



Entry	Catalyst	Products / μmol					C ₁₂ H ₂₆	H ₂
		SN	1	2	3			
1	Pt/TiO ₂	6.2	0.29	0.81	1.0	n.d. ^b	70	
2	Pd/TiO ₂	2.9	0.12	0.49	0.54	n.d.	35	

^a Reaction conditions: M/TiO₂ catalyst 0.2 g, n-hexane 0.76 mmol (0.1 mL), acetonitrile 74.7 mmol (3.9 mL). Reaction time was 1 h. The wavelength of irradiation was 365 \pm 20 nm and the intensity was 27mW cm⁻² measured at 360 \pm 15 nm. ^b not detected.

5.3.2 Cyanomethylation of cyclohexene



The direct cyanomethylation of cyclohexene with acetonitrile (eq. 2) was examined to know the property of the photocatalytic cyanomethylation system and to expand the application to unsaturated hydrocarbon. Although an authorized reagent could not be commercially obtained for the assignment of the main product, the main product was assigned to 2-cyclohexenyl acetonitrile (CA) according to the following results; (i) the retention time of the main product in the gas chromatograph was close to but clearly different from that of a purchased reagent of 1-cyclohexenyl acetonitrile, (ii) the mass fragments in the mass spectrum of the main product were almost the same but not identical to those of the purchased reagent of 1-cyclohexenyl acetonitrile (Fig. 5.3), and (iii) it is fact that the

C–H bond dissociation energy at allylic position is the lowest in a cyclohexene molecule (Table 5.3).

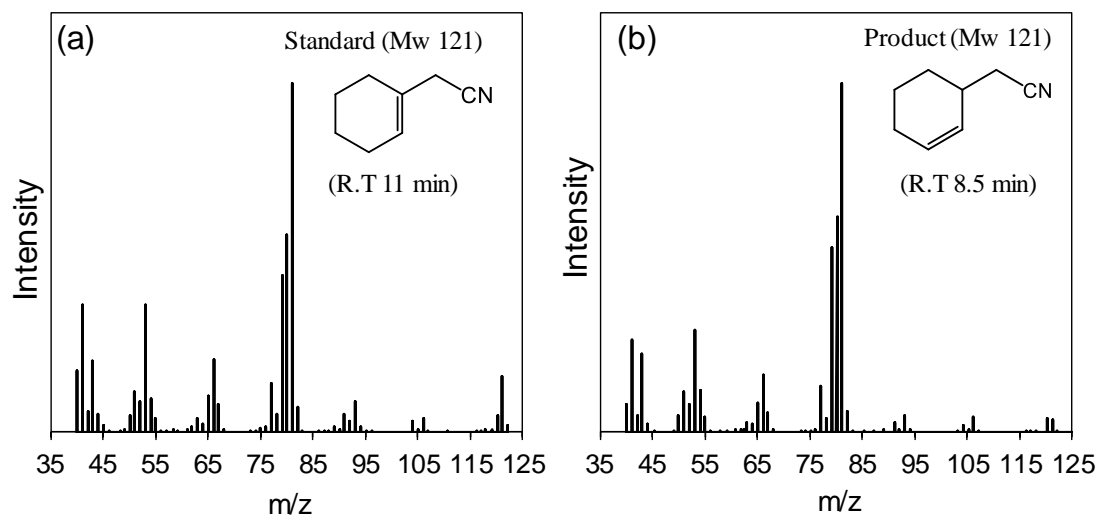
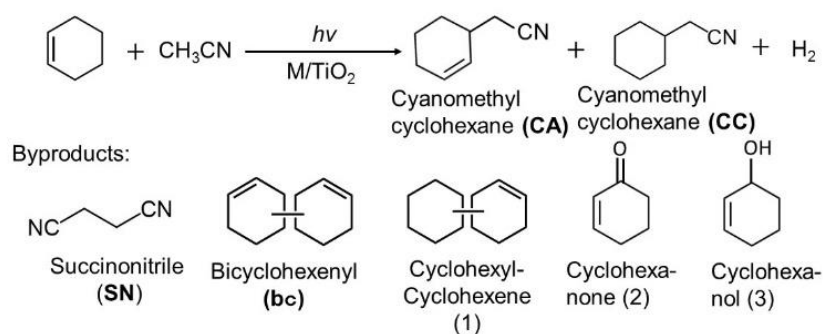


Figure 5.3. GC-Mass fragments of (a) the standard compound of 1-cyclohexenyl acetonitrile and (b) the product obtained from the direct cyanomethylation of cyclohexene with acetonitrile over the M/TiO₂ sample.

Table 5.5 shows the results of the reaction tests with the M/TiO₂ samples. Cyanomethylated cyclohexene, *i.e.*, 2-cyclohexenyl acetonitrile (CA), was produced as the major product over each photocatalyst. The Pt/TiO₂ sample produced higher amount of CA than the Pd/TiO₂ sample (Table 5.5, entries 1 and 2). Since the pristine TiO₂ sample exhibited very small activity, the metal nanoparticles were confirmed to function as the electron receiver enhancing the charge separation (Table 5.5, entry 3). The physical mixture of the Pt/TiO₂ sample and the Pd/Al₂O₃ sample did not exhibit higher yield of CA than the Pt/TiO₂ sample alone (Table 5.5, entry 4). As for the byproducts, cyanomethyl cyclohexane (CC), and some kinds of homo-coupling products from cyclohexene were produced, *e.g.*, bicyclohexenyls (bc) such as [1,1'-bi(cyclohexane)]-2,2'-diene and the hydrated compounds. The small amount of cyclohexenol and cyclohexenone were also detected because of water added in the reaction solution. Interestingly, SN was not detected and the large amount of CA and bc was produced even though large amount of acetonitrile existed in the reactor, which would originate from the much

lower C–H bond dissociation energy of the allylic position of cyclohexene (350 kJ mol⁻¹) than that of acetonitrile (406 kJ mol⁻¹) as shown in Table 5.3.

Table 5.5. Results of the photocatalytic reaction tests for the cyanomethylation of cyclohexene with acetonitrile over the M/TiO₂ photocatalyst samples or a mixture of Pt/TiO₂ and Pt/Al₂O₃.^a



Entry	Catalyst ^b	Products /μmol							
		CA	CC	SN	bc	1	H ₂	2	3
1	Pt/TiO ₂	42	5.4	tr.	24	n.d.	90	1.4	0.81
2	Pd/TiO ₂	16	7.8	n.d. ^d	8.4	6.6	10	2.0	1.9
3	TiO ₂	n.d.	n.d.	n.d.	2.4	n.d.	1.7	1.1	0.24
4	Pt/TiO ₂ + Pd(1.0)/Al ₂ O ₃ ^e	30	4.1	n.d.	22	n.d.	70	1.0	0.52

^a Catalyst 0.2 g, cyclohexene 0.987 mmol (0.1 mL), acetonitrile 74.6 mmol (3.8 mL), and water 5.56 mmol (0.1 mL). Reaction time was 1 h. The wavelength of the light irradiation was 360±20 nm and the light intensity was 27 mW cm⁻² measured at 360±15 nm. Not detected. ^b A mixture of the Pt(0.1wt%)/TiO₂ photocatalyst of 0.2 g and the Pd(1.0 wt%)/Al₂O₃ sample of 0.2 g was used.

To confirm the RDS in the present condition, the reaction tests with the isotopic compounds was carried out over the Pd/TiO₂ photocatalyst. As shown in Table 5.6, the *k_H*/*k_D* value for the CA formation was 3.9 when deuterated acetonitrile (CD₃CN) was used. This suggests that the C–H bond activation of acetonitrile would be the rate-determining step in this condition, which is clearly different from the case of the cyanomethylation of cyclohexane mentioned above. The RDS in these reactions seems related to the order of the C–H bond dissociation energy of the reactants (Table 5.3), cyclohexane (416 kJ mol⁻¹) > acetonitrile (406 kJ mol⁻¹) > cyclohexene (350 kJ mol⁻¹ at allylic

position as the lowest one), *i.e.*, the RDS would be determined by the difficulty of the radical formation through the C–H bond dissociation. Thus, in these conditions, the RDS in the cyanomethylation of cyclohexane was the formation of the cyclohexane radical, while that in the cyanomethylation of cyclohexene was the formation of cyanomethyl radical. The k_H/k_D value for the yield of bc was less than unity in the reaction between cyclohexene and CD_3CN , indicating that the oxidation of cyclohexene and acetonitrile to form these radical species would competitively proceed during this reaction in the similar way as discussed above.

Table 5.6. Results of the reaction tests with isotopic compounds for the cyanomethylation of cyclohexene over the Pd/TiO₂ sample ^a

Entry	Isotope	Products ^{b)} / μ mol			k_H/k_D ^{c)}	
		CA	bc	SN	CA	bc
1	None	12	9.1	n.d. ^{d)}	-	-
2	CD ₃ CN	3.1	18	n.d.	3.9	0.48
3	C ₆ D ₁₀	12	2.0	n.d.	1.0	5.4

^a Catalyst 0.2 g, cyclohexene 0.987 mmol (0.1 mL), acetonitrile 74.6 mmol (3.8 mL), and water 5.56 mmol (0.1 mL). A Pyrex test tube (ca.70 mL) was used as a reactor. Reaction time was 1 h. The wavelength of the light irradiation was 365 ± 20 nm, and the light intensity was 27 mW cm^{-2} measured at 360 ± 15 nm. ^b CA=2-cyclohexenyl acetonitrile, bc= the sum of bicyclohexenyl including isomers, SN=succinonitrile. ^c k_H/k_D = (yield with the normal compound) / (yield with the deuterated reagent). ^d Not detected.

The radical formation from cyclohexene over the Pd/TiO₂ sample was confirmed by ESR measurements. As shown in Fig. 5.4, the sharp signals were detected in the presence of the Pd/TiO₂ sample under photoirradiation, which means radical species were generated from cyclohexene by the photocatalyst. The signals showed a double triplet with the g value of 2.006 and the hyperfine coupling constant of $A^N=1.33$ mT (triplet) and $A^H=0.21$ mT (doublet), respectively. The possible spin adduct structure was suggested to be the cyclohexene-PBN adduct shown in Fig. 5.4, indicating that the cyclohexenyl radical was formed from cyclohexene. Signals originating from the hydrogen radical

adduct could not be observed in this condition. Since the radical formation of the cyanomethyl radical was confirmed with the Pd/TiO₂ photocatalyst in the literature [10], it is proposed that the reaction between cyclohexene and acetonitrile would involve a radical cross-coupling between cyclohexenyl radical and cyanomethyl radical.

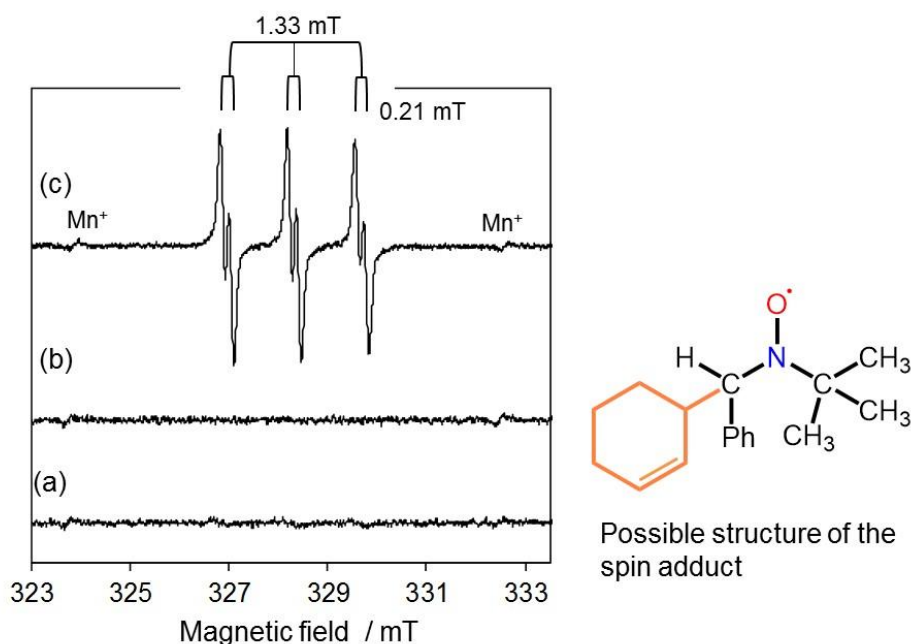


Figure 5.4. ESR spectra of the cyclohexene solution containing PBN in argon atmosphere, (a) measured after light irradiation for 20 min without the Pd/TiO₂ sample, (b) measured in the presence of the Pd/TiO₂ sample without light irradiation, (c) measured after light irradiated for 10 min in the presence of the Pd/TiO₂ sample.

Considering from the KIE effects and the ESR signals, the reaction between cyclohexene and acetonitrile would be explained by the radical coupling mechanism involving two photoexcitation steps as shown in Fig. 5.5. The photoformed hole oxidizes cyclohexene to cyclohexenyl radical, in which the radical centre is at the allylic position. The photoformed hole oxidizes also acetonitrile to cyanomethyl radical, which is the rate determining step (RDS) in this photocatalytic reaction. Then, the cross-coupling proceeds between these radicals, while homo-coupling reactions would also

undergo as the side reactions. In the current reaction condition, since the cyclohexenyl radical would be predominantly formed compared with the cyanomethyl radical, CA and bc were produced as the major products, but SN was rarely formed.

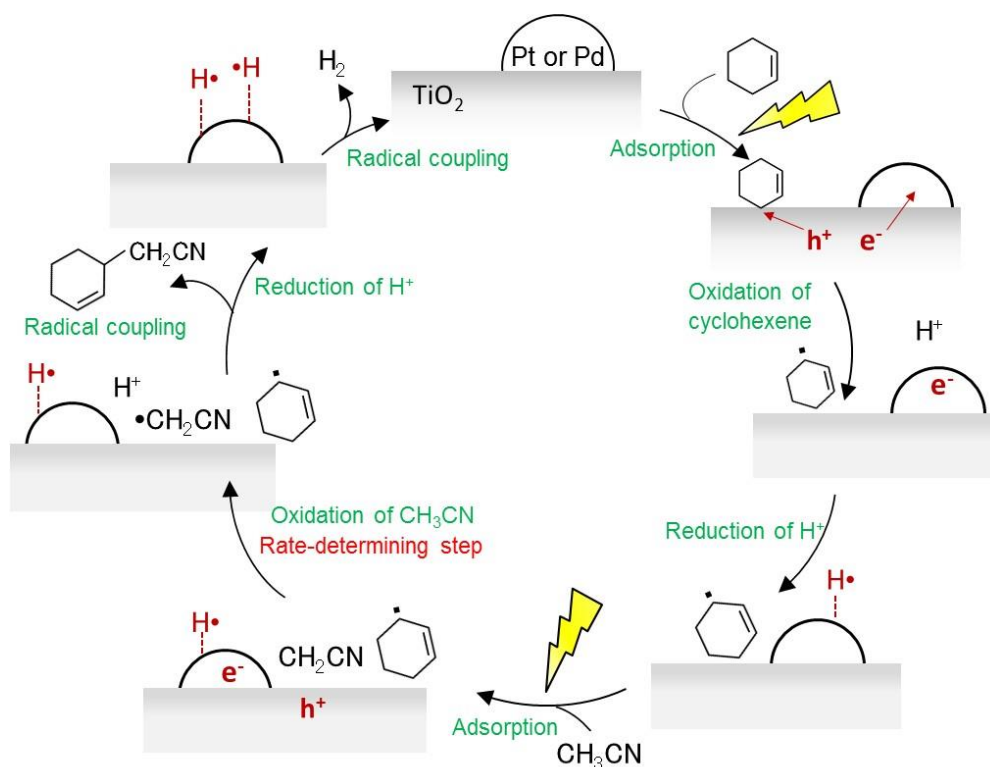
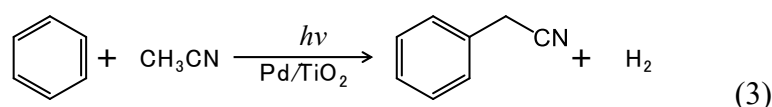


Figure 5.5 Proposed reaction mechanism of the direct cyanomethylation between cyclohexene and acetonitrile over the M/TiO₂ photocatalyst.

5.3.3 The cyanomethylation of benzene



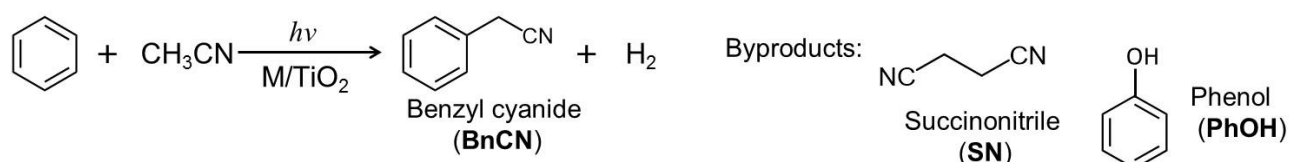
According to the study of the photocatalytic cyanomethylation of benzene [10], it was found that the cyanomethylation of benzene (eq. 3) was promoted by the hybrid Pd/TiO₂ catalyst consisting of Pd thermal catalyst and TiO₂ photocatalyst. Here, it was again confirmed that the reaction between

benzene and acetonitrile over the Pd/TiO₂ sample gave benzyl cyanide (BnCN) as the major product, and phenol (PhOH) and succinonitrile (SN) as the minor products (Table 5.7, entry 2). The formation of SN suggests that cyanomethyl radical generates through the photocatalytic oxidation of acetonitrile before the homo-coupling. In fact, the ESR spectra elucidated the formation of the cyanomethyl radical in the presence of the Pd/TiO₂ sample under photoirradiation. [10] Since the biphenyl was not detected as a homo-coupling product in this reaction condition, benzene would not be oxidized to phenyl radical species so much. This is supported by the fact that the C–H bond activation energy [19a] of benzene (440 kJ mol⁻¹ as shown in Table S1) is much higher than that of acetonitrile (406 kJ mol⁻¹).

On the other hand, it is notable that the reaction over the Pt/TiO₂ sample gave a very small amount of BnCN with a large amount of SN (Table 5.7, entry 1), which means this photocatalyst would be active at least for generation of the cyanomethyl radical. The pristine TiO₂ sample scarcely produced the coupling products (Table 5.7, entry 3), indicating that these metal nanoparticles enhanced the photocatalytic reactions. As mentioned above, it is generally accepted that these metal nanoparticles can function as the electron receiver to enhance the charge separation, and Pt is one of the most typical electron receiver, and actually the Pt/TiO₂ sample was more active than the Pd/TiO₂ sample for the cyanomethylation of aliphatic hydrocarbons. However, the Pt/TiO₂ sample promoted very slowly the cyanomethylation of benzene with acetonitrile, which is also well consistent with the previous study [10]. Although the cyanomethyl radical was produced by the both catalysts, BnCN as the cross-coupling product was obtained only with the Pd/TiO₂ sample, and hardly obtained with the Pt/TiO₂ sample. Thus, it was suggested the Pd nanoparticles would be necessary to catalyse the reaction between benzene and cyanomethyl radical as a dark process for the cyanomethylation of benzene. It is also indicated that this hybrid catalyst consisting the Pd metal catalyst and the TiO₂ photocatalyst can be applied to other aromatic compounds such as toluene and pyridine as reported in the literature [10], implying that the Pd/TiO₂ hybrid catalyst promotes the cyanomethylation of aromatic ring of these compounds.

In the present study, further experiments were carried out to confirm the assumption that the reaction between benzene and cyanomethyl radical would require the Pd nanoparticles as a catalyst. If the Pd nanoparticles catalysed the reaction of benzene with cyanomethyl radical, BnCN would be obtained even in the coexistence of the Pd/Al₂O₃ sample as a supported metal catalyst and the Pt/TiO₂ sample as a photocatalyst for radical formation.

Table 5.7. Results of the photocatalytic reaction tests for the cyanomethylation of benzene with acetonitrile over the M(0.1wt%)/TiO₂ photocatalyst, a mixture of the Pt/TiO₂ sample and the Pd/Al₂O₃ sample, or the Pd/Al₂O₃ sample. ^a



Entry	Catalyst	Products / μ mol			
		BnCN	PhOH	SN	H ₂
1	Pt/TiO ₂	0.08	0.91	12	20
2	Pd/TiO ₂	4.0	1.6	1.1	10
3	TiO ₂	n.d. ^d	n.d.	tr ^e	1.1
4	Pt/TiO ₂ + Pd(0.1)/Al ₂ O ₃ ^b	0.40	0.35	9.4	13
5	Pt/TiO ₂ + Pd(1.0)/Al ₂ O ₃ ^b	4.4	0.89	2.8	3.7
6	Pt/TiO ₂ + Pd(2.0)/Al ₂ O ₃ ^b	4.6	1.8	0.81	1.0
7	Pt/TiO ₂ + Al ₂ O ₃ ^b	0.08	0.43	5.8	15
8	Pd(1.0)/Al ₂ O ₃ ^c	n.d.	n.d.	n.d.	n.d.

^a Reaction conditions: the M(0.1wt%)/TiO₂ photocatalyst 0.2 g, benzene 1.1 mmol (0.1 mL), acetonitrile 72.8 mmol (3.8 mL), and water 5.56 mmol (0.1 mL). Reaction time was 1 h. The wavelength of the irradiation light was 365 \pm 20 nm and the light intensity was 27 mW cm⁻² measured at 360 \pm 15 nm. ^b The loading amount of Pd or Pt on the TiO₂ photocatalyst was 0.1 wt% and on the Al₂O₃ support was 0, 0.1, 1.0, or 2.0 wt%. A mixture of the Pt/TiO₂ sample of 0.2 g and the Pd/Al₂O₃ sample of 0.2 g was used. ^c The amount of the catalyst was 0.2 g. ^d Not detected. ^e trace.

The results are listed in Table 5.7, entries 4–6. The amount of BnCN was negligible small in the absence of the Pd/Al₂O₃ sample (Table 5.7, entry 1), whereas BnCN was obtained with the Pt/TiO₂

photocatalyst and the Pd/Al₂O₃ catalyst (Table 5.7, entries 4–6). In addition, the yield of BnCN was improved with the increase of the loading amount of Pd on the Al₂O₃ support, but it was not efficiently improved more than 1.0 wt% loading, although the formation of SN was suppressed with higher loading amount of Pd on the Al₂O₃ support. It is noted that the mixture of the Pt/TiO₂ sample and bare Al₂O₃ support (Table 5.7, entry 7) gave very small amount of the products. Hence, these results obviously support that the Pd nanoparticles should catalyse the reaction between benzene and the cyanomethyl radical, which should be not a photocatalytic process but a catalytic process. The Pd/Al₂O₃ sample itself did not give any product upon photoirradiation (Table 5.7, entry 8), confirming that the Al₂O₃ support could not function as a photocatalyst due to the large band gap and thus the Pt/TiO₂ photocatalyst was required to generate the cyanomethyl radical species.

In order to clarify the catalytic property of the Pd nanoparticles furthermore, temperature controlled reaction tests were performed over the Pd/TiO₂ sample. It is expected that the yield of BnCN will increase with the temperature if the Pd nanoparticles supported on the TiO₂ photocatalyst can function as a metal catalyst. As a result, the BnCN yield increased with increasing the reaction temperature, but the SN yield did not increase so much as shown in Fig. 5.5. The apparent activation energy calculated from the pseudo Arrhenius plot for the formation of BnCN was 43 kJ mol⁻¹, which seems high enough as that for a thermal catalytic process to produce BnCN. This step would be the rate determining step among the thermal processes, which should be the catalysis by the Pd metal nanoparticles loaded on the TiO₂ support. This step would correspond to the addition-elimination step between benzene and cyanomethyl radical. The KIE of this reaction over the Pd/TiO₂ sample suggests that the C–H bond dissociation of benzene is not involved for the production of BnCN [10]. Therefore, it can be concluded that the Pd thermal catalyst activate molecular benzene to react with the cyanomethyl radical for the formation of the transition state having a sp³ carbon in the benzene ring, where electron would be donated from the electron rich Pd metal nanoparticles [13] to π* orbital of benzene. In contrast, the apparent activation energy for the formation of SN was 5.5 kJ mol⁻¹ that is

acceptable as the activation energy for the photocatalytic reaction [20], suggesting that SN was formed by a photocatalysis through the homo-coupling of the cyanomethyl radicals.

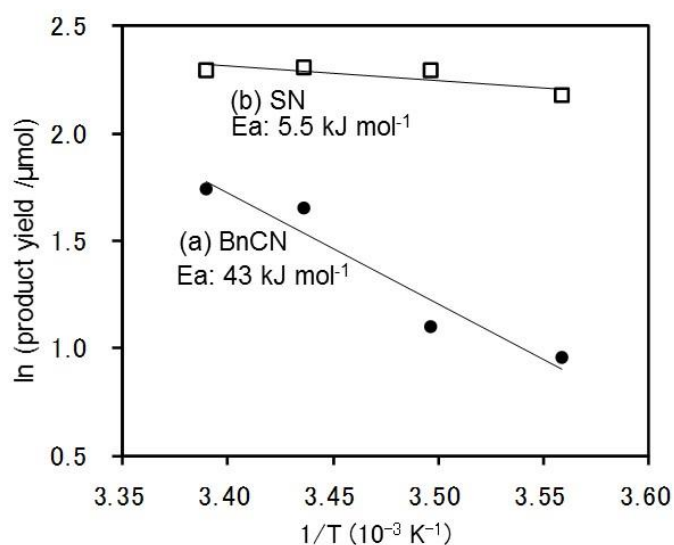


Figure 5.5. Pseudo Arrhenius plot of (a) benzyl cyanide (BnCN) and (b) succinonitrile (SN) yields with the Pd/TiO₂ hybrid catalyst at various temperatures. Reaction condition: the Pd/TiO₂ sample 0.2 g, benzene 0.99 mmol (0.1 mL), and acetonitrile 73 mmol (3.9 mL). Reaction time was 2 h. The wavelength of irradiation light was 360±20 nm and the light intensity was 27 mW cm⁻² measured at 360±15 nm.

Therefore, the reaction mechanism of the cyanomethylation of benzene over the Pd/TiO₂ hybrid catalyst should be concluded as presented in Fig. 5.6. The hole generated by the photoexcitation of TiO₂ and oxidizes acetonitrile to form the cyanomethyl radical and proton, which is the rate determining step in the whole catalytic cycle of this reaction in this condition [10]. Photoformed electron reduces the proton to hydrogen radical. The Pd metal nanoparticle as a metal catalyst has an interaction with benzene to activate by adsorption. Due to this catalytic activation, the cyanomethyl radical can react with the adsorbed and activated benzene to form the complex having sp³ carbon in the transition state, as shown in Fig. 5.6. Through the C–H bond dissociation at the sp³ carbon in the transition state, BnCN is produced with releasing a hydrogen radical, which means that formation of

BnCN is one photon process. Hydrogen molecule is produced from this hydrogen radical and another hydrogen radical produced through the reduction by the photoexcited electron.

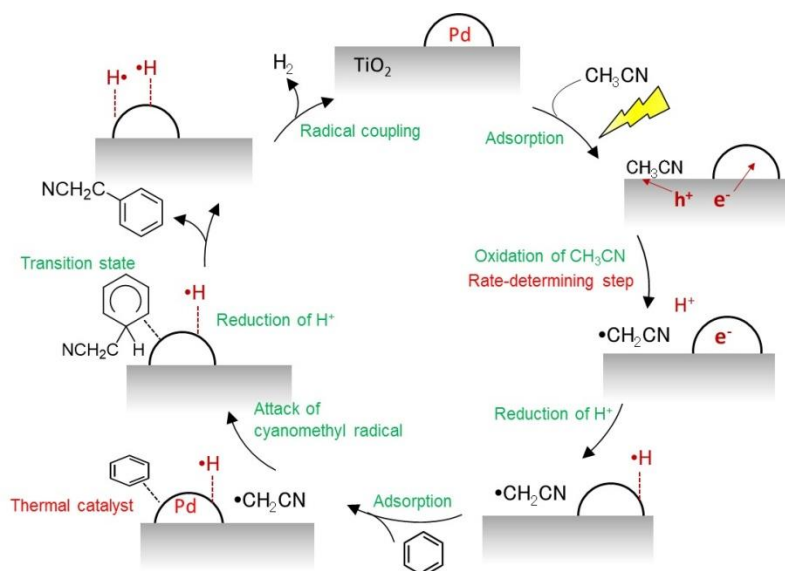


Figure 5.6. Proposed addition-elimination mechanism for the cyanomethylation of benzene over the Pd/TiO₂ hybrid catalyst.

5.3.4 The role of Pd thermal catalyst

Both of the Pt/TiO₂ and Pd/TiO₂ samples promoted the cyanomethylation of cyclohexane and cyclohexene (Table 5.1, entries 1–2, and Table 5.5, entries 1–2) via radical coupling reaction. The addition of the Pd/Al₂O₃ samples to the reaction system did not improve these cyanomethylation reactions (Table 5.1, entry 4–6 and Table 5.3, entry 4), which means that the Pd metal catalyst was not required in these cases. Hence, it was concluded that the cyanomethylation of cyclohexane and cyclohexene are mainly promoted by the photocatalysis with the M/TiO₂ samples, but the metal catalysis would not contribute to the reaction so much. In these reactions, the Pd nanoparticles would contribute as an acceptor of photoexcited electron to prolong the life time of the photoexcited charge carriers and enhance the radical formation, like as the Pt cocatalyst mentioned above.

However, the Pd metal catalyst is necessary for the photocatalytic cyanomethylation of

benzene with acetonitrile. This would be related to the high C–H bond dissociation energy for benzene molecule. This reaction was well promoted by the Pd/TiO₂ hybrid catalyst (Table 5.5, entry 2) as well as the physical mixture of the Pt/TiO₂ photocatalyst and the Pd/Al₂O₃ catalyst (Table 5.5, entries 4–6). This fact evidenced that the supported Pd nanoparticles can function as the catalyst for the substitution reaction of the cyanomethyl radical and benzene. The Pd nanoparticles would activate benzene ring before the substitution reaction with cyanomethyl radical. On the other hand, it is also considered that the Pd nanoparticles deposited on the TiO₂ photocatalyst would also contribute as the electron acceptor for the photoexcited electrons to improve the photocatalysis for the formation of the cyanomethyl radical.

In the past studies, photocatalytic reactions for aromatic functionalization such as hydroxylation of benzene [12] and amination of benzene [13] were well promoted by Pt/TiO₂ photocatalyst without the Pd metal catalyst. In these reactions, ammonia and water molecules are oxidized to the radical species by the photogenerated holes and the addition-elimination reaction proceeds between a molecular benzene and these radical species without the Pd metal catalyst. This is because these radical species would have enough reactivity toward a molecular benzene. On the other hand, the cyanomethyl radical would be more stable and less reactive than these radical species such as the surface hydroxyl radical and the amide radical, since the cyano group in the cyanomethyl radical would withdraw the electron from the radical centre to delocalize the radical property. Therefore, in the photocatalytic cyanomethylation of benzene with acetonitrile, the assist by the Pd catalyst would be necessary to promote the substitution process of benzene by the cyanomethyl radical species, especially for the formation of the complex in the transition state. The Pd catalyst was not required for the cyanomethylation proceeding via radical coupling, such as the cyanomethylation of aliphatic hydrocarbons with acetonitrile, because the reactants can be oxidized to the radical species having enough reactivity for the radical coupling in nature. The assist by the Pd metal catalyst is required only for the addition–elimination process between aromatic ring and somewhat stable radical species such

as cyanomethyl radical.

5.4. Conclusion

The direct cyanomethylation of cyclohexane and cyclohexene with acetonitrile by metal loaded photocatalysts proceeds via radical coupling reaction, where the reaction takes place photocatalytically even without the aid of Pd metal catalysis. In these cases, the Pt and Pd nanoparticles on the TiO₂ photocatalyst would contribute as just an acceptor of photoexcited electrons to enhance the photocatalytic reaction rate. These reactions are two photon processes.

In contrast, the Pd/TiO₂ hybrid catalyst or the physical mixture of the Pt/TiO₂ photocatalyst and the Pd/Al₂O₃ catalyst are required to promote the reaction between benzene and acetonitrile, where the Pd nanoparticle functions as a metal catalyst for the reaction between benzene molecule and cyanomethyl radical species through the addition-elimination process before completing the cyanomethylation. The cyanomethyl radical cannot directly attack the benzene molecule without the aid of the Pd catalyst because of the lower reactivity of the radical species. In the cyanomethylation of benzene, the Pd nanoparticle on the TiO₂ photocatalyst functions as not only an acceptor for the photoexcited electron but also a metal catalyst. Thus, the Pd nanoparticle is bifunctional cocatalyst. This is a one photon process.

In this chapter, some rules in the photocatalytic organic reactions were suggested, *i.e.*, both of the reactivity of reactant to become the corresponding radical species and the reactivity of the radical species should be the important factors for the determination of the reaction rate and the product selectivity, and the metal nanoparticles can help these reaction steps as an electron acceptor or a metal catalyst to promote the photocatalytic coupling reactions. These simple photocatalytic coupling reaction systems would provide wider desirable applications in the field of chemical synthesis in view of green and sustainable chemistry.

References

- [1] Kawano, Y.; Kaneko, N.; Mukaiyama, T. *Chem. Lett.*, **2005**, *34*, 1508–1509.
- [2] (a) Shang, R.; Ji, D.-S.; Chu, L.; Fu, Y.; Liu, L. *Angew. Chem., Int. Ed.*, **2011**, *50*, 4470–4474.
(b) Yeung, P. Y.; Chung, K. H.; Kwong, F.Y. *Org. Lett.*, **2011**, *13*, 2912–2915.
- [3] Kurz, M. E.; Lapin, S. C.; Mariam, K.; Hagen, T. J.; Qian, X. Q. *J. Org. Chem.*, **1984**, *49*, 2728–2733.
- [4] Chakraborty, S.; Patel, Y. J.; Krause, J. A.; Guan, H. *Angew. Chem., Int. Ed.*, **2013**, *52*, 7523–7526.
- [5] Zhang, J.; Wu, W.; Ji, X.; Cao, S. *RSC Adv.*, **2015**, *5*, 20562–20565.
- [6] Liu, Y.; Yang, K.; Ge, H. *Chem. Sci.*, **2016**, *7*, 2804–2808.
- [7] Velcicky, J.; Soicke, A.; Steiner, R.; Schmalz, H. G. *J. Am. Chem. Soc.*, **2011**, *133*, 6948–6951.
- [8] (a) Pan, C.; Zhang, H.; Zhu, C. *Org. Biomol. Chem.*, **2015**, *13*, 361–364. (b) Bunescu, A.; Wang, Q.; Zhu, J. *Angew. Chem. Int. Ed.* **2015**, *54*, 3132–3135. (c) Li, J.; Wang, Z.; Wu, N.; Gao, G.; You, J. *Chem. Commun.*, **2014**, *50*, 15049–15051.
- [9] Bond, G.C.; Webb, G.; Wells, P.B.; Winterbottom, J.M. *J. Catal.*, **1962**, *1*, 74–84.
- [10] Yoshida, H.; Fujimura, Y.; Yuzawa, H.; Kumagai, J.; Yoshida, T. *Chem. Commun.*, **2013**, *49*, 3793–3795.
- [11] (a) Yuzawa, H.; Yoshida, H. *Topics in Catal.*, **2014**, *57*, 984–994. (b) Yuzawa, H.; Yoshida, H. *Chem. Lett.*, **2013**, *42*, 1336–1343.
- [12] (a) H. Yoshida, H. Yuzawa, M. Aoki, K. Otake, H. Itoh, and T. Hattori, *Chem. Commun.*, 2008, **38**, 4634– (b) Yuzawa, H.; Aoki, M.; Otake, K.; Hattori, T.; Itoh, H.; Yoshida, H. *J. Phys. Chem. C*, **2012**, *116*, 25376–25387.
- [13] (a) Yuzawa, H.; Yoshida, H. *Chem. Commun.*, **2010**, *46*, 8854–4636. (b) Yuzawa, H.; Kumagai, J.; Yoshida, H. *J. Phys. Chem. C*, **2013**, *117*, 11047–11058.
- [14] Tyagi, A.; Matsumoto, T.; Kato, T.; Yoshida, H. *Catal. Sci. Technol.*, **2016**, *6*, 4577–4583.
- [15] (a) Bard, A. J. *Science*, **1980**, *207*, 139–144. (b) Yuzawa, H.; Mori, T.; Itoh, H. Yoshida, H. *J. Phys. Chem. C*, **2012**, *116*, 4126–4136.
- [16] (a) Tomita, O; Otsubo, T.; Higashi, M.; Ohtani, B.; Abe, R. *ACS Catal.*, **2016**, *6*, 1134–1144.
(b) Ohtani, B.; Iwai, K.; Nishimoto, S. I.; Sato, S. *J. Phys. Chem. B*, **1997**, *101*, 3349–3359.
- [17] Nishimoto, S.; Ohtani, B.; Kagiya T. *J. Chem. Soc., Faraday Trans.*, **1985**, *1*, 81, 2467–2474.
- [18] Libertini, L. J.; Griffith, O.H. *J. Chem. Phys.*, **1970**, *53*, 1359–1367.

- [19] (a) Luo, Y-R. *Handbook of bond dissociation energies in organic compounds*, **2007**, CRS press. (b) Tian, Z.; Fattahi, A.; Lis, L.; Kass, S.R. *J. Am. Chem. Soc.*, **2006**, 128, 17087–17092.
- [20] (a) Davis, R. J.; Gainer, J. L.; O'Neal, G.; Wu, I. W. *Water Environ. Research*, **1994**, 66, 50–53. (b) Vorontsov, A.V.; Savinov, E.N.; Barannik, G.B.; Froitsky, V.N.; Parmon, V.N. *Catal. Today*, **1997**, 39, 207–218. (c) Shimura, K.; Maeda, K.; Yoshida, H. *J. Phys. Chem. C*, **2011**, 115, 9041–9047.

Chapter 6

Dehydrogenative Lactonization from Diols with Platinum Loaded Titanium Oxide Photocatalyst

Abstract

A new catalytic route for lactonization from diols was developed by using metal loaded TiO₂ photocatalyst. Phthalide, an aromatic lactone, was selectively obtained from 1,2-benzenedimethanol in high yield in the presence of Pt loaded rutile TiO₂ photocatalyst. The selective lactonization did not proceed with Pt loaded anatase TiO₂ photocatalyst because further oxidation of phthalide proceeded. The lactonization from other diols also proceeded by the Pt loaded rutile TiO₂ photocatalyst. In addition, the reaction rate was improved by addition of heterogeneous acid catalyst such as Al₂O₃ and protonated titanate nanotube.

6.1. Introduction

Lactones, cyclic esters, are important chemicals in both academic and industrial fields because they are useful as chemical intermediates or solvents in organic syntheses [1]. In order to synthesize lactones, various reaction routes have been developed. The most common one is intramolecular dehydrative esterification of hydroxycarboxylic acid promoted by Brønsted acid [2]. In general, the reaction process of dehydrative cyclization requires strong acids [1], which limits available reactants for this reaction. Recently, many research groups have reported new reaction routes to obtain lactones, for example, the reaction of epoxide [3] or aliphatic alcohols with CO [4], and reaction of allenol or butadiene with CO₂ [5]. However, these reaction systems usually require high pressure of CO or CO₂ gases and low temperature to increase the solubility of gases [4, 5b, 5c], although the lactonization with CO₂ under the mild gas pressure was also reported [3, 5a].

Another practical reaction route for lactonization is the dehydrogenative oxidation of diols. Many homogeneous catalysts such as Ir- or Ru-complexes have been reported to synthesize various lactones [6,7]. Xie and Stahl reported that the Cu metal complex catalyst with nitroxyl radicals such as TEMPO (2,2,6,6-tetramethylpiperidine 1-oxyl) efficiently catalyzes the aerobic oxidative lactonization of diols at room temperature under ambient conditions [8]. Although homogenous

catalysts are considered to have difficulties for products separation and reuse, Fujita et al. developed a reusable Ir-complex catalyst [6c].

Heterogeneous catalysts for lactonization have been also reported. For example, the Cu-based catalysts [9] and the Au loaded TiO₂ catalyst [10] were reported for the lactonization of 1,4-butanediol to form γ -butyrolactone in the gas phase. CeO₂-based binary oxides was developed for the gaseous phase lactonization of 1,6-hexanediol to ϵ -caprolactone [11]. On the other hand, for liquid phase lactonization, Au loaded hydrotalcite was investigated for the lactonization of 1,4-butanediol with oxygen molecules [12]. Very recently, it was found that Pt loaded SnO₂ catalyst well promotes the oxidative lactonization from various diols at 453 K under solvent free conditions [13]. In addition, Zue *et al.* reported the reaction route with tungstic acids or ZrO₂-supported WO₃ and H₂O₂ to promote the dehydrogenative lactonization from 1,2-benzenedimethanol to form phthalide in high yield (ca. 90%) with high selectivity [14,15].

In this chapter, as a new methodology, dehydrogenative lactonization of diols by a metal loaded TiO₂ photocatalysts is described. Phthalide is a common chemical as the intermediate for pharmaceutical chemicals and fine chemicals [14,16], but the synthesis of phthalide by heterogeneous catalyst was reported to require high temperature such as 453 K, and high pressure of H₂ gas [16]. It was found that Pt loaded rutile TiO₂ photocatalyst promoted the lactonization for the dehydrogenative lactonization from 1,2-benzenedimethal to phthalide as well as that from various diols.

6.2 Experimental

6.2.1 Preparation of metal loaded photocatalyst

Employed TiO₂ powders (JPC-TIO-8, anatase, 338 m²/g; JPC-TIO-6, rutile, 100 m²/g; and JPC-TIO-4, anatase and rutile, 50 m²/g) were supplied from Catalysis Society of Japan were used as photocatalysts. Metal loaded TiO₂ (M/TiO₂) samples were prepared by a photodeposition method in the presence of methanol as a hole scavenger. First, TiO₂ powder (4.0 g) was pre-irradiated by the light

from a 300 W xenon lamp without optical filters (the intensity was 50 mW/cm² measured at 360±15 nm) to clean the catalyst surface for 60 min. After the pre-irradiation, distilled water (200 mL), methanol (40 mL), and a stock solution of a metal precursor (H₂PtCl₆, Wako 99.8 %, dissolved in water, or PdCl₂, Wako 99.0 %, dissolved in a HCl aqueous solution, or RhCl₂, Wako 99.0 %, dissolved in water) were added. The mixture was stirred for 15 min in the dark, and then photoirradiated from the xenon lamp without optical filters for 60 min. The photodeposited sample was separated from the suspension by suction filtration, washed with ion exchanged water, and dried at 323 K overnight in air to obtain the metal loaded TiO₂ photocatalyst sample. The loading amount of metal was 0.1 wt%.

To examine the relationship between the specific surface area and the catalytic activity of the sample, 2.0g of TiO₂ powder (TIO-6 or TIO-8) was calcined in a furnace at various temperature for 1 h. For the measurement of the Barunauer-Emmett-Teller (BET) specific surface area, the sample was evacuated at 423 K for 1 h, followed by N₂ adsorption experiment at 77 K using an automatic gas adsorption instrument (Monosorb, MS-21, Quantachrome).

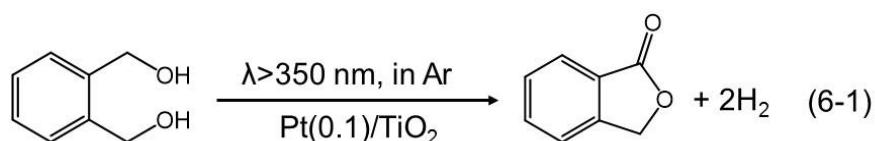
6.2.2 Catalytic reaction

The catalytic reaction tests were carried out in the following manner. The M/TiO₂ sample of 0.1 g was put into a closed reactor made by quartz. Before the reaction was started, the Pt/TiO₂ sample was irradiated for 20 min by the xenon lamp with an optical filter ($\lambda > 350$ nm) with the light intensity of 27 mW cm⁻² measured at 360 nm±15 nm, and the gas phase was purged by argon gas for 15 min. The reaction mixture, 200 μ mol or 400 μ mol of diol dissolved in 4 mL of solvents, was introduced into the reactor. The reaction tests were carried out for 1 h or more under photoirradiation. After the photocatalytic reaction, the gaseous products were taken by a gas-tight syringe, and then the liquid phase including products were separated from the reaction mixture with filtration. Products in gaseous phase were analyzed by GC-TCD (Shimadzu, GC-8A) and liquid phase were analyzed by GC-MS (Shimadzu, GCMS-QP2020). In the present study, molecular hydrogen was always detected when the

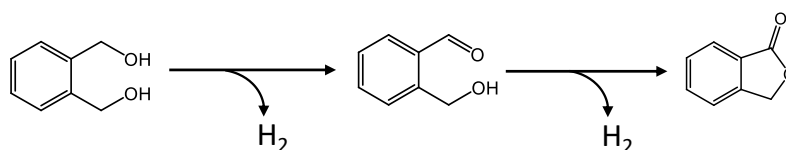
reaction proceeded. However, the value of the yielded hydrogen was not so accurate, especially when the production amount was large.

6.3 Results and discussion

6.3.1 Lactonization of benzenedimethanol



The lactonization from benzenedimethanol to yield phthalide over the Pt loaded TiO₂ photocatalyst was examined in an acetonitrile solution (eq. 6-1). Figure 6.1 shows a time course of the product yield over the Pt/TiO-8 photocatalyst. In the initial period of the reaction 2-(hydroxymethyl)benzaldehyde was preferably formed. The yield of phthalide gradually increased from the start and then became the major product after 2 h with a decrease of the yield of 2-(hydroxymethyl)benzaldehyde. The yield of phthalide reached to 60 % in 3 h. This result indicates that 2-(hydroxymethyl)benzaldehyde is formed as an intermediate, and further oxidation of the intermediate forms phthalide, *i.e.*, the lactonization from benzenedimethanol to form phthalide proceeds via two step oxidation (scheme 6.1). However, the reaction over the Pt/TiO-8 provided low selectivity to phthalide such as 25 % and the carbon balance was poor such as 60 % after 3 h, which means that formation of other byproducts or decomposition of the substrate would also take place. As for gaseous product, hydrogen was actually detected, though the value of the obtained amount had large experimental error.



Scheme 6.1. Two step oxidation in photocatalytic lactonization

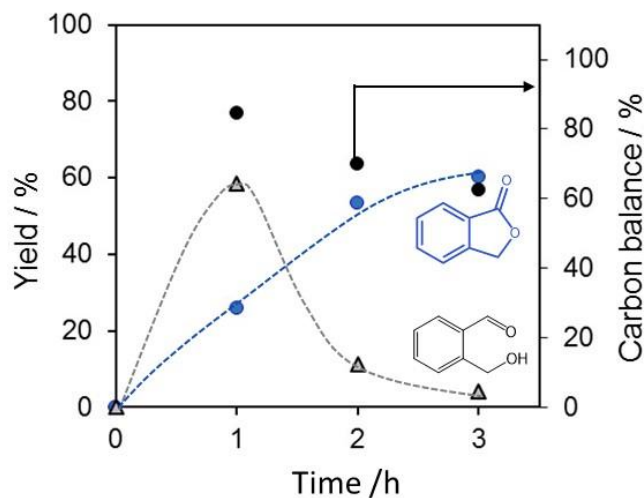
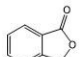
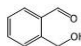


Figure 6.1. Time course of lactonization from 1,2-benzenedimethanol over the Pt/TIO-8 sample. Reaction condition: 1,2-benzenedimethanol of 200 μmol was dissolved in acetonitrile, the amount of the Pt/ST-01 sample was 0.1 g, the Pt loading amount was 0.1 %, the wavelength of the light from the xenon lamp was over 350 nm, and the intensity was 27 mW cm^{-2} measured at 360 ± 15 nm. The calibration curve of phthalide was applied to determine the yielded amount of 2-(hydroxymethyl)benzaldehyde.

On the other hand, the Pt/TIO-6 photocatalyst produced phthalide of 90 % in yield even at initial period for 1 h with high selectivity such as 90% (Table 6.1, entry 1), where 2-(hydroxymethyl)benzaldehyde as the intermediate was not detected. That is, the Pt/TIO-6 sample consisting of rutile TiO_2 showed 3.5 times higher yield of phthalide than the Pt/TIO-8 sample consisting of anatase TiO_2 , although the BET surface area of TIO-6 (100 m^2/g) is smaller than that of TIO-8 (338 m^2/g) (Table 6.1, entries 1 and 2). The reaction over the Pt/TIO-4 sample (Table 6.2, entry3), in which TiO_2 has both anatase and rutile crystal structures and low specific surface area, did not afford phthalide so much. To confirm the effect of the specific surface area, the two kinds of TiO_2 , rutile (TIO-6) and anatase (TIO-8) were calcined to lower the specific surface area, and the relationship between the photocatalytic activity and the specific surface area of the TiO_2 photocatalysts was examined. Figure. 6.3 shows the results. It is clear that the photocatalytic activity increases with an

increase of the surface area for each TiO₂ sample. Further, it is notable that the slope depends on the crystal phase, *i.e.*, rutile is more favorable than anatase for this photocatalytic reaction when they are compared at the same specific surface area.

Table 6.1. Results of the reaction tests for the dehydrogenative lactonization of 1,2-benzenedimethanol over various metal loaded TiO₂ photocatalysts in acetonitrile ^a

Entry	Catalyst	Crystal Phase ^b	BET area (m ² g ⁻¹)	Conv. (%)	Yield (μmol)			Phthalide	
							H ₂	Selec. (%)	Yield (%)
1	Pt/TIO-6	(R)	100	>99	180	n.d. ^c	200	90	90
2	Pt/TIO-8	(A)	338	>98	52	110	110	25	25
3	Pt/TIO-4	(A,R)	50	80	31	12	90	19	15
4	Pd/TIO-6	(R)	100	40	45	10	45	56	23
5	Rh/TIO-6	(R)	100	79	98	40	65	60	49
6	TIO-6	(R)	100	< 1.0	n.d.	n.d.	n.d.	-	-

^a Reaction condition was the same as that described in the caption of Fig. 6.1. ^b(R) and (A) represent rutile and anatase, respectively. ^c not detected.

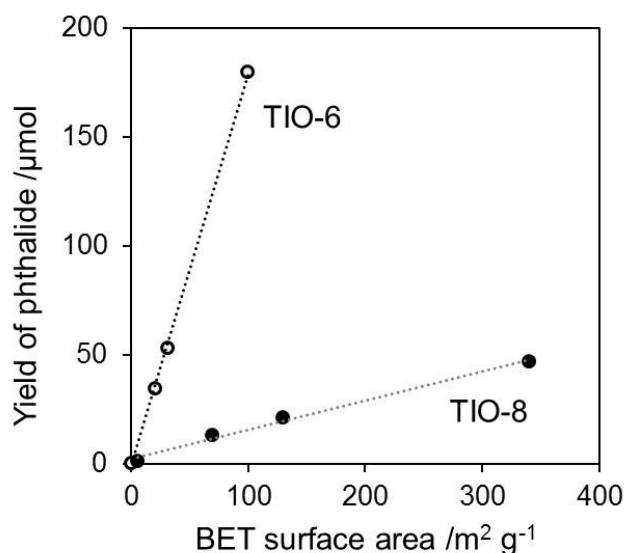


Figure 6.2. The effect of specific surface area of the photocatalysts on their photocatalytic activities of the Pt/TIO-6 sample and the Pt/TIO-8 sample. Reaction condition was the same as that described in the caption of Fig. 6.1.

To clarify the reason of the different activity between anatase and rutile, some experiments were carried out as shown in Table 6.2. First, the adsorption amount of the substrate, benzenedimethanol, on the catalyst surface in the acetonitrile was measured in the dark. Both the Pt/TIO-6 and Pt/TIO-8 samples showed very low and similar values, suggesting that the diol adsorption property of the samples would not be so important (Table 6.1, entries 1 and 2). Second, the adsorbed amount of phthalide on the Pt/TiO₂ samples in the dark was measured. The values were also very small and not so different from each other. Finally, the stability of the product against the successive reaction was examined in the presence of the Pt/TiO₂ photocatalysts under photoirradiation, where 20 μmol of phthalide was added in the solvent in the presence of the photocatalyst sample and then photoirradiated for 1 h. After the light irradiation, it was found that the remaining amount of phthalide decreased in the presence of the Pt/TIO-8 and the Pt/TIO-4 samples, whereas it was not changed so much in the presence of the Pt/TIO-6 sample. This means that the successive reaction hardly takes place on the Pt loaded rutile TiO₂ photocatalyst. Therefore, it is the reason why the Pt/TIO-6 photocatalyst exhibited the high yield of phthalide with high selectivity.

Table 6.2. Results of some experiments: The adsorbed amount of 1,2-benzendimethanol and phthalide, and the remaining amount of phthalide in the presence of the Pt/TiO₂ photocatalysts after the photoirradiation.

Entry	Sample	Crystal phase	Adsorbed amount of diol ^a (μmol)	Adsorbed amount of phthalide ^a (μmol)	Amount of phthalide in liquid after light irradiation ^b (μmol)
1	Pt/TiO-6	(R)	10	7	187
2	Pt/TiO-8	(A)	12	10	97
3	Pt/TiO-4	(A, R)	trace	trace	77

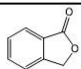
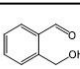
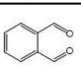
^a Stirred in the dark for 10 min. Conditions: 20 μmol of phthalide or benzenedimethanol was dissolved in acetonitrile of 4 mL, the amount of photocatalyst was 0.1 g. ^b Reaction condition was the same as that described in the caption of Figure 6.1 except for the use of 200 μmol of phthalide instead of 1,2-benzenedimethanol. Blank tests confirmed that phthalide and benzenedimethanol were not adsorbed by the reactor and phthalide did not decrease under the photoirradiation in the absence of the photocatalyst sample.

To know the efficiency of the precious metal co-catalyst, Pd and Rh were examined on the rutile TiO₂ photocatalyst. The Pd/TiO-6 sample and Rh/TiO-6 sample also promoted to the reaction (Table 6.1, entries 4 and 5), but the yields of phthalide were less than that of the Pt/TiO-6 sample. Since the bare rutile TiO₂ exhibited no activity (Table 6.1, entry 6), it is obvious that the precious metal cocatalyst drastically improves the photocatalytic activity.

The solvent effect in the photocatalytic lactonization was also confirmed. Table 6.3 shows the lactonization from 1,2-benzendimethanol with the Pt/TiO-8 sample in various solvents. When the reaction was examined in water, 1,2-benzendimethanol was slowly converted into phthalide in the presence of the Pt/TiO-8 sample (Table 6.3, entry 1). In contrast, the reaction proceeded in acetone and THF. The yields of phthalide in these solvents were almost the same as, or higher than, that in acetonitrile (Table 6.3, entries 3 and 4). However, the homocoupling of acetone and THF proceeded as well in these cases (Table 6.3, entries 3 and 4), while homocoupling of acetonitrile did not occur in acetonitrile (Table 6.3, entry 1). These results can be explained by the bond dissociation energy of these compounds, *i.e.*, the C–H bond activation energy of acetonitrile (406 kJ mol⁻¹) is higher than that

of THF (389 kJ mol⁻¹) and acetone (402 kJ mol⁻¹) [17]. These results indicate that the solvent affect the reaction rate and selectivity in the present photocatalytic reaction and the acetonitrile is a suitable solvent.

Table 6.3. Photocatalytic lactonization of 1,2-benzenedimethanol over the Pt/ST-01 photocatalyst in various solvents ^a

Entry	Solvent	Conv. / %	Yield / μmol				Phthalide	
						Homocoupling product	Yield / %	Selec. / %
1	Acetonitrile	>95	60	110	n.d. ^b	n.d.	30	30
2	Water	68	20	80	12	-	10	15
3	Acetone	90	70	120	n.d.	15	35	39
4	THF	>95	97	50	n.d.	47	49	49

^a Reaction conditions: 1,2-benzenedimethanol 200 μmol dissolved in 4 mL of solvent, the Pt/TiO-8 0.1 g, other conditions were the same as those described in the caption of Figure 6.1. ^b not detected.

6.3.2 Reaction mechanism of the photocatalytic lactonization

As depicted in the scheme 6.1, the photocatalytic lactonization consists of the two dehydrogenation steps. It was confirmed that the reaction cannot proceed in the dark or in the absence of the photocatalyst, indicating that the lactonization proceeds photocatalytically. Since TiO₂ has acid property [18], it was wondered if the acid property of TiO₂ might contribute to the present photocatalysis or not. Thus, reaction tests were carried out by the addition of heterogeneous acid catalyst to the reaction system. The results are shown in Table 6.4. The yield of phthalide increased when the acid catalysts such as Al₂O₃ or protonated titanate nanotube (TiNT, see also chapters 2 and 3) were introduced to the photocatalytic reaction mixture with the Pt/TiO-6 photocatalyst (Table 6.4, entries 3 and 4), suggesting that the acid sites can improve the reaction to form phthalide. However, it must be mentioned that in the presence of TiNT, dehydration of 1,2-benzendimethanol was proceed as

well as lactonization, indicating that acid catalyst having moderately strong acid sites is not available for this purpose. On the other hand, the acid catalyst having weak acid sites such as Al_2O_3 is useful to accelerate the photocatalytic reaction rate without promoting the side reactions. Separate experiment evidenced that the acid catalysts itself did not promote the reaction without photocatalyst, which confirmed that the acid catalysis accelerates at least one step such as the cyclization step during the photocatalytic lactonization reaction as shown in Scheme 6.1. Here, it is proposed that the blended catalyst consisting of the Pt/TiO_2 photocatalyst and the Al_2O_3 acid catalyst is an efficient catalyst for the photocatalytically dehydrogenative lactonization. The optimization of their combination will improve this reaction system further.

On the other hand, the yield of phthalide was not increased by the addition of bare TIO-6 sample to the reaction mixture including the $\text{Pt}/\text{TIO-6}$ sample, but rather decreased (Table 6.4, entry 2), although the TiO_2 has acid sites [18]. As mentioned above, bare TIO-6 sample did not give phthalide under the light irradiation (Table 6.1, entry 6). This result show the bare TiO_2 powder would shade the $\text{Pt}/\text{TIO-6}$ sample from the light to reduce the photoexcitation of the $\text{Pt}/\text{TIO-6}$ sample (Table 6.4, entry 2). Figure 6.3 shows the pseudo Arrhenius plot for the phthalide formation with the $\text{Pt}/\text{TIO-6}$ photocatalyst alone. The apparent activation energy for the formation of phthalide calculated from the plot was 4.6 kJ mol^{-1} , which would be acceptable value as activation energy for typical photocatalytic reaction [19]. These results clarify that the reaction with the $\text{Pt}/\text{TIO-6}$ photocatalyst proceeds photocatalytically and the acid sites on the TiO_2 surface cannot contribute to the reaction rate so much. Although some studies suggested that Pt nanoparticles [13] or Ag-based catalysts [20] functioned as metal catalysts in dehydrogenative lactonization, the result in Fig. 6.3 shows that thermal catalysis such as acid catalysis or metal catalysis did not contribute to the present reaction over the Pt/TiO_2 samples under this reaction condition.

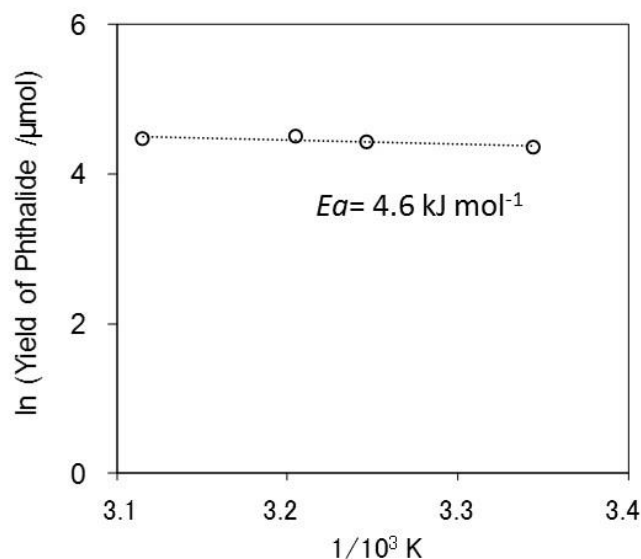


Figure 6.3. Pseudo Arrhenius plot for phthalide formation from 1,2-benzenedimethanol over the Pt/TiO-6 sample. A 70 mL of test tube was employed as a reactor. Other conditions were the same as those described in the caption of Figure 6.1 except for the reaction temperature.

Table 6.4. The lactonization of 1,2-benzenedimethanol by the physical mixture of the Pt/TiO-6 photocatalyst and acid catalyst ^a

Entry	Additional acid catalyst (0.1 g)	Conv. (%)	Product (μmol)		
			Phthalide (selec. %)	2-(hydroxymethyl) benzaldehyde	H ₂
1	-	90	110 (31)	240	250
2	TiO-6	81	100 (33)	210	200
3	Al ₂ O ₃	98	200 (50)	172	320
4	TiNT ^b	98	230 (59)	72	310

^a Reaction conditions: 1,2-benzenedimethanol of 400 μmol was dissolved in acetonitrile of 4 mL, the amount of the Pt/ST-01 sample was 0.1 g, other conditions were the same as those described in the caption of Figure 6.1. ^b Protonated titanate nanotube.

Based on the above results, it is proposed that the dehydrogenative lactonization from 1,2-benzenedimethanol to produce phthalide with the Pt/TiO₂ photocatalyst proceeds as shown in Fig. 6.4. The photoformed hole on the TiO₂ surface oxidizes the diol to form the corresponding radical species, and proton. This radical species can be converted to an aldehyde, which is the intermediate in the

reaction, with generation of a hydrogen radical. The hydrogen radical reacts with the formed proton and photoexcited electron to form molecular hydrogen. Further oxidation of the intermediate compound proceeds by another photoformed hole, and then phthalide is produced with producing another molecular hydrogen in the same way.

The addition of the acid catalyst would accelerate at least one step during the whole photocatalytic reaction steps. As one possibility, the acid sites might interact with the carbonyl group to assist the cyclization.

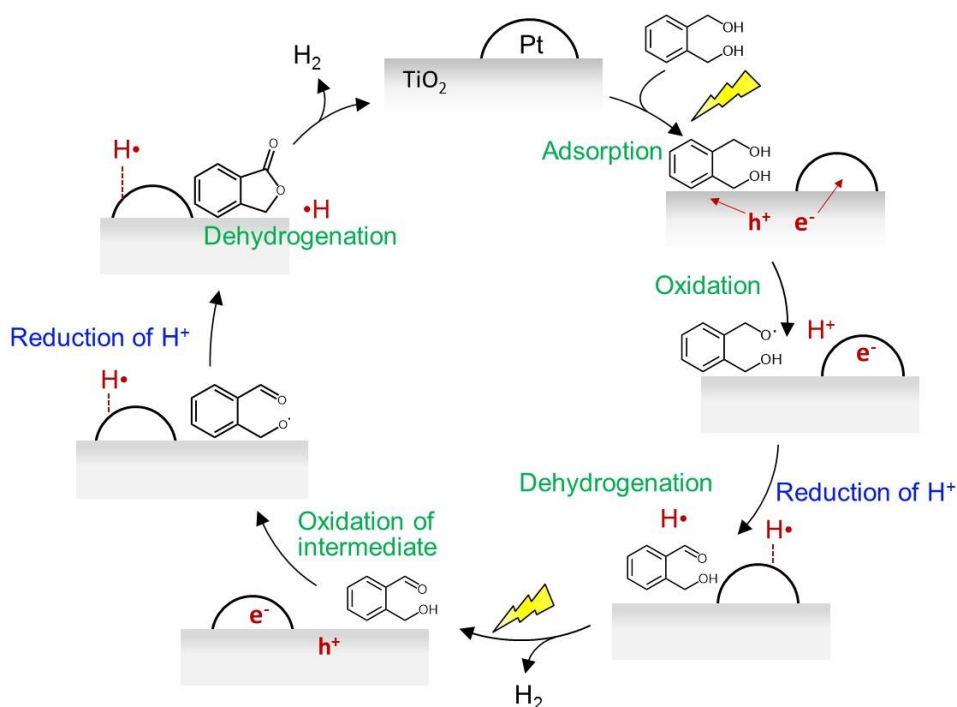


Figure 6.4. Proposed reaction mechanism for two step oxidation in the photocatalytic lactonization

6.3.3 The photocatalytic lactonization of other diols

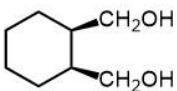
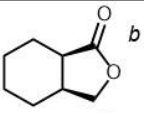
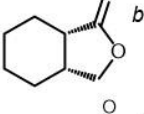
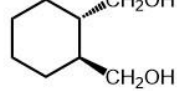
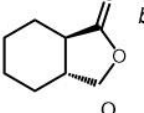
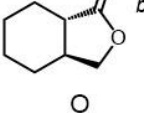
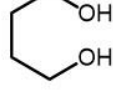
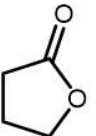
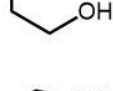
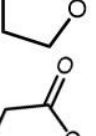
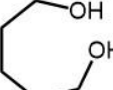
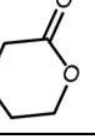
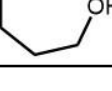
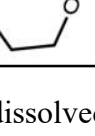
In order to expand the scope of the current reaction system, the lactonizations from various diols were examined with the Pt/TiO₂ photocatalyst. The results are listed in Table 6.5. All diols were transformed into corresponding lactones. The Pt/TIO-6 sample promoted all these reactions more than the Pt/ST-01 sample. The yields of lactones in these cases were lower than that in the lactonization

from 1,2-benzenedimethanol.

The lactonization from *cis*-1,2-cyclohexanedimethanol over the Pt/TIO-6 sample gave dominantly the corresponding lactone compounds **1** and **2** ((3*aS*,7*aR*)-hexahydroisobenzofuran-1(3*H*)-one and (3*aR*,7*aS*)-hexahydroisobenzofuran-1(3*H*)-one, total 83 μmol , 42 % in yield) as the products of stereoretention reaction, and the other lactone compounds **3** and **4** ((3*aR*,7*aR*)-hexahydroisobenzofuran-1(3*H*)-one and (3*aS*,7*aS*)-hexahydroisobenzofuran-1(3*H*)-one, total 8.0 μmol , 4.0 % in yield) as the products of the stereoinversion reaction (Table 6.5, entry 1). The Pt/TIO-8 sample gave the same products with low yields (Table 6.5, entry 2). The Pt/TIO-6 sample gave the higher stereoretention ratio (*r*) than the Pt/TIO-8 sample, which indicates that the C–C bond dissociation of starting compound can happen more easily in the presence of the Pt/TIO-8 sample. The same tendency to retain the stereochemical structure was observed in the lactonization reaction from *trans*-1,2-cyclohexanedimethanol (Table 6.5, entries 3 and 4), but the total yields of lactone compounds decreased compared with the lactonization from *cis*-1,2-cyclohexanedimethanol, which would be related to the structural torsion of the lactone **3** and **4**.

The lactonization from 1,4-butanediol also proceeded as well as the other lactones (Table 6.5, entries 5 and 6), but the reaction from 1,5-pentandiol was hardly proceeded (Table 6.5, entries 7 and 8). In these cases, the high flexibility of the carbon chain structure would decrease the chance to form the cyclic structure.

Table 6.5. The lactonization of various diols catalyzed by the M/TiO₂ photocatalysts ^a

Entry	catalyst	Substrates	Product	Yield (%)			<i>r</i> ^c
				Total	1 + 2	3 + 4	
1	Pt/TiO-6		1 	46	42	4.0	11
2	Pt/TiO-8			2 	20	17	3.3
3	Pt/TiO-6		3 	24	3.1	21	6.8
4	Pt/TiO-8			4 	10	1.9	8.5
5	Pt/TiO-6			20			
6	Pt/TiO-8			5.0			
7	Pt/TiO-6			2.5			
8	Pt/TiO-8			n.d. ^d			

^a Reaction conditions: diols of 200 μmol was dissolved in acetonitrile of 4 mL, the other conditions were the same as those mentioned in the caption of Fig. 6.1. ^b The calibration curve of starting materials were applied to determine the yields of lactones because the products were not commercially available.

^c $r = (\text{sum of yields of products via stereoretention reaction}) / (\text{sum of yields of products via stereo inversion reaction})$. ^d Not detected.

6.4 Conclusion

In conclusion, the new synthesis route for the lactones from diols with Pt/TiO₂ photocatalysts was established. The photocatalytic lactonization proceeds via two-step dehydrogenation process. The Pt loaded rutile TiO₂ photocatalyst exhibits higher yield of lactones with higher selectivity than Pt loaded anatase TiO₂ because the further oxidation proceeded in the presence of anatase TiO₂. It is also proposed that the blended catalyst consisting of the photocatalyst and the acid catalyst such as Al₂O₃ is more efficient for the dehydrogenative lactonization.

References

- [1] Paul, D. M. *Essential of Organic Chemistry 3ed*, **2006**, Pearson, p225
- [2] March, J. *Advanced organic chemistry 3ed*. **1985**, Wily,
- [3] Kramer, J. W.; Lobkovsky, E. B.; Coates, G. W. *Org. Lett.*, **2006**, 8, 3709–3712.
- [4](a) Kreimerman, S.; Ryu, I.; Minakata, S.; Komatsu, M. *Org. Lett.*, **2000**, 2, 289–391 (b) Yoneda, E.; Zhang, S. W.; Zhou, D. Y.; Onitsuka, K.; Takahashi, S. *J. Org. Chem.*, **2003**, 68, 8571–8576.
- [5] (a) Li, S.; Miao, B.; Yuan, W.; Ma, S. *Org. Lett.*, **2013**, 15, 977–979. (b) Pierre, B.; Matt, D.; Nobel, D. *J. Am. Chem. Soc.*, **1988**, 110, 3207–3212. (c) Inoue, Y.; Sasaki, Y.; Hashimoto, H. *Bull. Chem. Soc. Jan.* **1978**, 51, 2375–2378.
- [6] (a) Suzuki, T.; Morita, K.; Tsuchida, M.; Hiroi, K. *Org. Lett.*, **2002**, 4, 2361–2363. (b) Kawahara, R.; Fujita, K. I.; Yamaguchi, R. *J. Am. Chem. Soc.*, **2012**, 134, 3643–3646. (c) K. Fujita.; W. Ito.; R. Yamaguchi. *ChemCatChem*, **2014**, 6, 109–112.
- [7] (a) Zhao, J.; Hartwig, J. F. *Organometallics*, **2005**, 24, 2441–2446.
- [8] (a) Xie, X.; Stahl, S. S. *J. Am. Chem. Soc.* **2015**, 137, 3767–3770. (b) Hoover, J. M.; Stahl, S. S. *J. Am. Chem. Soc.*, **2011**, 133, 16901–16910
- [9] (a) Hu, T.; Yin, H.; Zhang, R.; Wu, H.; Jiang, T.; Wada, Y. *Catal. Commun.*, **2007**, 8, 193–199. (b) Ichikawa, N.; Sato, S.; Takahashi, R.; Sodesawa, T.; Inui., K. *J. Mol. Catal. A Chem.*, **2004**, 212, 197–203.
- [10] Huang, J.; Dai, W. L.; Li, H.; Fan, K. *J. Catal.*, **2007**, 252, 69–76.
- [11] Akashi, T.; Sato, S.; Takahashi, R.; Sodesawa, T.; Inui, K. *Catal. Commun.*, **2003**, 4, 411–416.
- [12] Mitsudome, T.; Noujima, A.; Mizugaki, T.; Jitsukawa, K.; Kaneda, K. *Green Chem.*, **2009**, 11, 793–797.
- [13] Touchy, A. S.; Shimizu, K. I. *RSC Advances*, **2015**, 5, 29072–29075.
- [14] Zhu, Q.; Chu, X.; Zhang, Z.; Dai, W. L.; Fan, K. *Green Chem.*, **2010**, 12, 205–208.
- [15] (a) Zhu, Q.; Chu, X.; Zhang, Z.; Dai, W. L.; Fan, K. *Appl. Catal. A: General*, **2012**, 435, 141–147. (b) Zhang, Z.; Zhu, Q.; Ding, J.; Liu, X.; Dai, W. L. *Appl. Catal. A: General*, **2014**, 482, 171–178.
- [16] Liu, Y. X.; Xing, T.F.; Wei, Z.J.; Li, X.N.; Yan, W. *Catal. Commun.*, **2009**, 10, 2023–2026.
- [17] Lou, Y-R., *CRS press*, **2007**, Handbook of bond dissociation energies in organic compounds.
- [18] (a) Tanabe, K.; Htattori, H.; Sumiyoshi, T.; Tamaru, K.; Kondo, T. *J. Catal.* **1978**, 53, 1–8. (b) Hadjiivanov, K. *Appli. Surf. Sci.*, **1998**, 135, 331–338.
- [19] (a) Davis, R. J.; Gainer, J. L.; O'Neal, G.; Wu, I. W. *Water Environ. Research*, **1994**, 66, 50–53. (b) Vorontsov, A.V.; Savinov, E.N.; Barannik, G.B.; Froitsky, V.N.; Parmon, V.N. *Catal. Today*, **1997**, 39, 207–218. (c) Shimura, K.; Maeda, K.; Yoshida, H. *J. Phys. Chem. C*, **2011**, 115, 9041–9047.
- [20] Gooßen, L.J.; Ohlmann, D. M.; Dieker, M. *Green Chem.*, **2010**, 12, 197–200.

Chapter 7

Summary

In this thesis, Friedel-Crafts alkylation of aromatic compounds by the protonated titanate nanotube catalysts and photocatalytic cyanomethylation and lactonization by the metal loaded TiO₂ photocatalysts were studied. Here, the findings obtained in these studies were summarized.

In Chapter 1, acid-catalyzed organic reactions and photocatalytic organic reactions were shortly reviewed to remind the background of this thesis. In case of acid-catalyzed reactions, heterogeneous catalysts have been desired because they are reusable and easily separate with products after the reaction. Some examples of acid catalyzed reactions promoted by heterogeneous catalysts were mentioned. Among them, it was noted that some of reactions were cooperatively enhanced by two kinds of the acids sites, Brønsted acid sites and Lewis acid sites. As for photocatalytic organic reactions, it was mentioned that some studies have been reported successive photocatalytic organic synthesis by Pt/TiO₂ photocatalyst or Pd/TiO₂ bifunctional catalyst in the absence of oxygen. Finally, the outline of this thesis was introduced.

In Chapter 2, it was demonstrated that Brønsted acid sites of protonated titanate nanotubes was stronger than that of titanate nanosheets. Titanate materials such as layered titanate, nanosheets, and nanotubes were applied for the Friedel-Crafts alkylation of toluene with benzyl chloride. It was found that the catalytic activity was well promoted by protonated titanate nanotubes. The results of MAS NMR and FT-IR analysis suggested that titanate nanotubes has stronger Brønsted acid sites than other materials, suggesting it originates from the tube structure with torsion. This hypothesis was supported by the results of DFT calculation using ammonia as a probe molecule. Since other titanate materials except for the titanate nanotubes did not promote the reaction at room temperature, the strong Brønsted acid sites on the nanotube should assist the reaction.

In Chapter 3, hydrothermally treated titanate materials were prepared at various temperatures and applied for Friedel-Crafts alkylations of toluene with benzyl alcohol or benzyl chloride. Anatase nanoparticles were converted into various titanate structures by the hydrothermal treatment, and the nanotube structure was formed at 423 K. The nanotube significantly enhanced both of the Lewis catalyzed reaction and Brønsted acid catalyzed reaction, suggesting that OH group of the nanotubes function as a Brønsted acid. Considering the results of Chapter 1 and 2, protonated titanate nanotube has OH group functioned as Brønsted acid sites, and the cooperative work of Lewis acid sites and Brønsted acid sites enhances the Friedel-Crafts alkylation of toluene with benzyl chloride at 300 K.

In Chapter 4, Nb doped titanate nanotube (Nb-TiNT) was synthesized in order to improve the catalytic property of the titanate nanotube. XRD patterns and the results of N₂ adoption measurements suggested that the nanotube structure forms regardless of Nb amounts. However, the TEM images and the results from ICP-AES analysis revealed that Nb oxide not only substituted with Ti of titanate nanotube but also formed amorphous Nb oxides particles on the surface. The Lewis acid catalyzed reaction between toluene and benzyl chloride significantly enhanced over the Nb-TiNT samples compared to the non-doped TiNT sample. Furthermore, the Brønsted acid catalyzed reaction of toluene with benzylalcohol was also enhanced over the Nb-TiNT samples, which suggests the existence of doped Nb atoms in the titanate nanotubes framework. Since the catalytic activity of Nb-containing solid acid catalysts such as Nb₂O₅·nH₂O and Nb–Ti mixed oxides, and the physical mixture of Nb₂O₅ and TiNT was lower than that of the Nb-TiNT samples, Nb cations were partially doped into nanotubes to generate Brønsted acid sites such as Ti(OH)Nb. ³¹P MAS NMR and FT-IR measurements with base probe molecules evaluated that acid amount of both of the Nb-TiNT samples and the TiNT sample was almost the same, but the strong Brønsted acid sites increased on the Nb-TiNT samples. Since the pore size distributions of the Nb(5%)-TiNT sample was narrower than that of the TiNT sample, it can be concluded that strong Brønsted acid sites and uniformed pore distributions were formed by adding Nb,

resulting the high catalytic activity of the Nb-TiNT samples for Friedel-Crafts alkylation of aromatic compounds.

In Chapter 5, the direct cyanomethylation of hydrocarbons with acetonitrile over metal loaded TiO₂ photocatalyst (M/TiO₂) was demonstrated. The Pt/TiO₂ photocatalyst promoted the cyanomethylation of cyclohexane and cyclohexene more than the Pd/TiO₂ photocatalyst, and the catalytic property of the Pd metal particles, which was observed in the cyanomethylation of benzene, did not contribute to increase the yields of cyanomethylated cyclohexane and cyclohexene. In these reactions, the oxidation of reactants by holes competitively occur to form the corresponding radical species, followed by the radical coupling to yield both of homo- and cross-coupling reactions. The radical species have enough reactivity to promote the coupling reactions, and thus the contribution of metal catalyst was not observed. These reactions were two photons processes. In contrast, the cyanomethylation of benzene, which was proceeded via addition-elimination reaction with one photon, required the metal catalysis by the Pd nanoparticles, which was evidenced by the Arrhenius plot and the reaction test with alumina-supported Pd catalyst. Considering from the results of the cyanomethylation of aliphatic and aromatic hydrocarbons, it was revealed that the Pd catalyst activated the aromatic ring to react with cyanomethyl radical. In conclusion, the Pd catalyst is important for the photocatalytic addition-elimination reaction involving the reaction between aromatic ring and less active radicals such as cyanomethyl radical.

In Chapter 6, the lactonization from diols are examined with Pt/TiO₂ photocatalyst. The reaction from 1,2-benzenedimethanol to phthalide was well promoted by Pt loaded rutile TiO₂ photocatalyst. The obtained of phthalide was up to 90 % in yield with 90 % in selectivity because rutile TiO₂ photocatalyst could not enhance successive oxidation of phthalide. In order to expand the scope of this reaction, some diols were also examined over the Pt/TiO₂ photocatalysts, and found that all

examined reactions proceeded in the presence of Pt loaded rutile TiO₂ photocatalyst more than Pt loaded anatase TiO₂ photocatalyst. In addition, it is proposed that the combination of acid catalyst and TiO₂ photocatalyst will improve the reaction rate of the lactonization.

As a conclusion of this thesis, the followings were clarified. Firstly, the protonated titanate nanotube developed in this study has two acid sites; Brønsted and Lewis acid sites. The Brønsted acid sites is formed from the process of scrolling the nanosheets which causes structure torsion. This Brønsted acid sites assists to enhance the reaction rate of the Friedel-Crafts alkylation of toluene with benzyl chloride, which is known to be promoted by a Lewis acid sites, at room temperature. The catalytic property of the titanate nanotube can be further improved by adding Nb atoms, where strong Brønsted acid sites and uniformed tube structure are formed.

Secondly, new photocatalytic organic reactions were developed by M/TiO₂ photocatalysts. The metal-loaded TiO₂ photocatalysts can promote the cyanomethylation of not only aromatic but also aliphatic hydrocarbons as well as the lactonization of various diols. The radical coupling reactions such as the cyanomethylation of aliphatic hydrocarbons and lactonization of diols take place without assistant of the Pd catalyst. On the other hand, in the case of the cyanomethylation of aromatic ring, the catalysis by the Pd metal nanoparticles is required for the reaction between the aromatic ring and the cyanomethyl radical via addition-elimination mechanism. This is due to the less reactivity of the aromatic ring and the radical species. It was also elucidated that the photocatalysis assisted by the metal catalysis exhibited more selective than the radical coupling reactions.

Publication list

Original papers corresponding to this thesis

Chapter 2

- 1 . Protonated Titanate Nanotubes with Lewis and Brønstead Acidity: Relationship between Nanotube structure and Catalytic Acidity

M. Kitano, E. Wada, K. Nakajima, S. Hayashi, S. Miyazaki, H. Kobayashi, M. Hara, *Chem. Mater.*, **2013**, vol.25, p385-393

Chapter 3

2. Effect of Preparation Conditions on the Structural and Acid Catalytic Properties of Protonated Titanate Nanotubes

E. Wada, M. Kitano, K. Nakajima, M. Hara, *J. Mater. Chem. A*, **2013**, vol.1, p12768-12774

Chapter 4

3. Synthesis of Nb-doped Titanate Nanotubes as Solid Acid Catalysts

E. Wada, M. Kitano, K. Nakajima, K. Yamamoto, M. Hara, *Catal. Sci. Technol.*, **2016**, vol6, p4832-4839

Chapter 5

4. Direct Cyanomethylation of Aliphatic and Aromatic Hydrocarbons with Acetonitrile over Metal Loaded Titanium Oxide Photocatalysts

Catal. Sci. Technol., to be submitted

Chapter 6

5. Dehydrogenative Lactonization from Diols with Platinum Loaded Titanium Oxide Photocatalyst

To be submitted

Acknowledgements

The present thesis has been carried out at Interdisciplinary Graduate School of Science and Engineering, Tokyo Institute of Technology under the supervision of Associate Professor Masaaki Kitano, and at Graduate School of Human Environmental Studies, Kyoto University under the supervision of Professor Hisao Yoshida.

The author would like to express his sincerest gratitude to Professor Hisao Yoshida for the fruitful discussion, valuable suggestion, and careful reviewing of the manuscript. The author is greatly indebted to Associate Professor Masaaki Kitano for instructive suggestions, advices, and reviewing of the manuscripts.

The author makes his gratitude to Associate Professor Kiyotaka Nakajima at Hokkaido University for his guidance and pointed comments. The author wants to demonstrate his offering to Assistant Professor Toshiyuki Yokoi at Tokyo Institute of Technology for the use of FE-SEM instrument. The author is deeply grateful to Mr. Mikio Ushiyama at Kanagawa Academy of Science and Technology for performing the TEM/EDS measurements of the protonated titanate nanotubes. The author would like to express my gratitude to Dr. Shigenobu Hayashi at National Institute of Advanced Industrial Science and Technology for the use of MAS NMR instrument and valuable discussions about the determination of acid strength with MAS NMR spectra. The author received generous support from Professor Hisayoshi Kobayashi and Mr. Soichi Miyazaki at Kyoto Institute of Technology for DFT calculations to compare the acidity of protonated titanate nanotube with titanate nanosheet. The author wants to express his gratitude to Dr. Kiichi Fukuhara and Ms. Mayo Sugano for fruitful discussion and helpful supports. The author wish to thank Mr. Kazuto Yamamoto at Tokyo Institute of Technology for performing the experiments of test reactions.

The author would like to thanks to Professor Tatsuhisa Kato at Kyoto University for the use of ESR instrument and generous support. The author appreciate the feedback offered by Dr. Hayato Yuzawa at Institute for Molecular Science. He gives me constructive comments for manuscript of direct cyanomethylation. The author would like to thank Assistant Professor Akira Yamamoto at Kyoto University for valuable discussion. The author shows gratitude to Professor Tomoko Yoshida at Osaka City University for measures of XAFS spectra although XAFS studies on Pd loaded TiO₂ and Al₂O₃ are not presented in this thesis.

Thanks should be made to Secretary Ms. Yuri Bonnitcha for her kind aids and official affaires. The author also would like to thank the new chemistry group member in Yoshida Lab., Mr. Tomoaki Takeuchi, Ms. Akansha Tyagi, Mr. Tomoyuki Ohara, Mr. Tomoya Matsumoto, and Mr. Shinpei Naniwa.

Finally, a financial support, Grant-in-Aid for JSPS Fellows from Japan Society for the promotion of Science must be acknowledged.

November 2016

Emiko Wada